Calhoun: The NPS Institutional Archive

DSpace Repository

Theses and Dissertations | 1. Thesis and Dissertation Collection, all items

2005-09

Multi-beam digital antenna for radar, communications, and UAV tracking based on off-the-shelf wireless technologies

Gezer, Berat Levent

Monterey California. Naval Postgraduate School

http://hdl.handle.net/10945/2583

Downloaded from NPS Archive: Calhoun

http://www.nps.edu/library

Calhoun is the Naval Postgraduate School's public access digital repository for research materials and institutional publications created by the NPS community. Calhoun is named for Professor of Mathematics Guy K. Calhoun, NPS's first appointed -- and published -- scholarly author.

Dudley Knox Library / Naval Postgraduate School
411 Dyer Road / 1 University Circle
Monterey, California USA 93943

NAVAL POSTGRADUATE SCHOOL

MONTEREY, CALIFORNIA

THESIS

MULTI-BEAM DIGITAL ANTENNA FOR RADAR, COMMUNICATIONS, AND UAV TRACKING BASED ON OFF-THE-SHELF WIRELESS TECHNOLOGIES

by

Berat Levent GEZER

September 2006

Thesis Advisor:	David C. Jenn
Second Reader:	Robert D. Broadston

Approved for public release, distribution is unlimited

THIS PAGE INTENTIONALLY LEFT BLANK

REPORT DOCUMENTATION PAGE		Form Approved OMB No. 0704-0188

Public reporting burden for this collection of information is estimated to average 1 hour per response, including the time for reviewing instruction, searching existing data sources, gathering and maintaining the data needed, and completing and reviewing the collection of information. Send comments regarding this burden estimate or any other aspect of this collection of information, including suggestions for reducing this burden, to Washington headquarters Services, Directorate for Information Operations and Reports, 1215 Jefferson Davis Highway, Suite 1204, Arlington, VA 22202-4302, and to the Office of Management and Budget, Paperwork Reduction Project (0704-0188) Washington DC 20503.

1. AGENCY USE ONLY *(Leave blank)*	2. REPORT DATE September 2006	3. REPORT TYPE AND DATES COVERED Master's Thesis

4. TITLE AND SUBTITLE : Multi-Beam Digital Antenna For Radar, Communications, and UAV Tracking Based On Off-The-Shelf Wireless Technologies	5. FUNDING NUMBERS
6. AUTHOR(S) Berat Levent GEZER	
7. PERFORMING ORGANIZATION NAME(S) AND ADDRESS(ES) Naval Postgraduate School Monterey, CA 93943-5000	8. PERFORMING ORGANIZATION REPORT NUMBER
9. SPONSORING /MONITORING AGENCY NAME(S) AND ADDRESS(ES) N/A	10. SPONSORING/MONITORING AGENCY REPORT NUMBER

11. SUPPLEMENTARY NOTES The views expressed in this thesis are those of the author and do not reflect the official policy or position of the Department of Defense or the U.S. Government.

12a. DISTRIBUTION / AVAILABILITY STATEMENT Approved for public release, distribution is unlimited	12b. DISTRIBUTION CODE

13. ABSTRACT (maximum 200 words)

The state-of-art technologies keep generating new ways of improving on the performance of the old systems. Array antennas, one of the continuously improving technologies, brought many benefits to our life. The superiorities of array antennas remove the disadvantages of the old technology radars such as great sidelobes, vulnerability to the jammers, and degradation effect of the clutter. Array antennas find many applications on different areas.

Today, unmanned aerial vehicles (UAVs) have begun to be seen in our life more often than before. UAVs prevent pilot loss of life. They carry out a variety of military and civilian missions such as surveillance and reconnaissance, target recognition, battle damage assessment, EW, search and rescue, and traffic monitoring. An important use of the UAVs is troop support, carrying out reconnaissance and surveillance missions, which requires maintaining a data-link with troops in order to send any data collected, such as video images, or audio.

During operations it is necessary to continuously maintain a data and control link with the operator. This requires the ground station antenna to track the UAV so the antenna beam is pointed properly. The purpose of this research is to design and build an array to angle-track a UAV and, eventually, to accomplish the data transfer from the UAV to the ground station.

14. SUBJECT TERMS Array, tracking antenna, tracking, CST Microwave Studio, characterization, LabVIEW	15. NUMBER OF PAGES 127
	16. PRICE CODE

17. SECURITY CLASSIFICATION OF REPORT	18. SECURITY CLASSIFICATION OF THIS PAGE	19. SECURITY CLASSIFICATION OF ABSTRACT	20. LIMITATION OF ABSTRACT
Unclassified	Unclassified	Unclassified	UL

NSN 7540-01-280-5500 Standard Form 298 (Rev. 2-89)
Prescribed by ANSI Std. 239-18

THIS PAGE INTENTIONALLY LEFT BLANK

Approved for public release, distribution is unlimited

MULTI-BEAM DIGITAL ANTENNA FOR RADAR, COMMUNICATIONS, AND UAV TRACKING BASED ON OFF-THE-SHELF WIRELESS TECHNOLOGIES

Berat L. GEZER
Lieutenant Junior Grade, Turkish Navy
B.S., Turkish Naval Academy, 2000

Submitted in partial fulfillment of the
requirements for the degree of

MASTER OF SCIENCE IN SYSTEMS ENGINEERING

from the

NAVAL POSTGRADUATE SCHOOL
September 2006

Author: Berat Levent GEZER

Approved by: Professor David C. Jenn
Thesis Advisor

Robert D. Broadston
Second Reader

Dan C. Boger
Chairman, Department of Information Sciences

THIS PAGE INTENTIONALLY LEFT BLANK

ABSTRACT

The state-of-art technologies keep generating new ways of improving on the performance of the old systems. Array antennas, one of the continuously improving technologies, brought many benefits to our life. The superiorities of array antennas remove the disadvantages of the old technology radars such as great sidelobes, vulnerability to the jammers, and degradation effect of the clutter. Array antennas find many applications on different areas.

Today, unmanned aerial vehicles (UAVs) have begun to be seen in our life more often than before. UAVs prevent pilot loss of life. They carry out a variety of military and civilian missions such as surveillance and reconnaissance, target recognition, battle damage assessment, EW, search and rescue, and traffic monitoring. An important use of the UAVs is troop support, carrying out reconnaissance and surveillance missions, which requires maintaining a data-link with troops in order to send any data collected, such as video images, or audio.

During operations it is necessary to continuously maintain a data and control link with the operator. This requires the ground station antenna to track the UAV so the antenna beam is pointed properly. The purpose of this research is to design and build an array to angle-track a UAV and, eventually, to accomplish the data transfer from the UAV to the ground station.

THIS PAGE INTENTIONALLY LEFT BLANK

TABLE OF CONTENTS

I. INTRODUCTION....1
A. BACKGROUND....1
B. PREVIOUS WORK....4
C. SCOPE OF RESEARCH....6
D. ORGANIZATION OF THESIS....7

II. MAIN PRINCIPLES OF TRACKING ANTENNAS....9
A. TRACKING SYSTEMS....9
B. TRACKING TECHNIQUES....11
1. Sequential Lobing....11
2. Conical Scanning....12
3. Monopulse Scanning....12
a. Amplitude Comparison Monopulse Systems....13
b. Phase-Comparison Monopulse Systems....15
C. TRACKING ERRORS....16
1. Thermal Noise....16
2. Angular Glint....18
3. Scintillation....19
4. Manufacturing Quality and Alignment....20
5. Total Error....20
D. OTHER EXTERNAL CAUSES OF ERROR....20
1. Multipath....20
2. Crosstalk Caused by Cross-Polarized Energy....22
3. Troposphere Propagation....23

III. TRACKING SYSTEM DESIGN CONSIDERATIONS....25
A. DETERMINING THE DESIGN PARAMETERS....25
B. POLARIZATION MISMATCH....38
C. CST MICROWAVE STUDIO SIMULATION RESULTS....41

IV. TRACKING ARRAY HARDWARE....47
A. DESCRIPTION OF THE COMPONENTS....47
1. Dipoles....48
2. Low Noise Amplifier (LNA)....49
3. Demodulator....49
4. Local Oscillator....51
5. Power Supplies and Power Adjustment Circuit....52
6. Signal Processing Devices....52
B. CHARACTERIZING THE COMPONENTS OF THE SYSTEM....55
C. ARRAY ASSEMBLY....60
D. LABVIEW CONTROLLER SOFTWARE....62
E. LABVIEW PROGRAM....63
F. INTEGRATION OF THE COMPONENTS....65
G. FINAL ANALYSIS OF THE ARRAY....70

V. CONCLUSION AND RECOMMENDATIONS 75
A. SUMMARY AND CONCLUSION 75
B. RECOMMENDATIONS FOR FUTURE WORK 76
1. Circularly Polarized Antennas 76
2. Simplifying LabVIEW Program 76
3. Acquisition System 76
4. Verifying the Pattern Distributions 77
5. Data Transfer 77
6. Operational Testing 77

APPENDIX 79
A. MATLAB CODES TO DEFINE THE DESIGN PARAMETERS 79
B.1. MATLAB CODE FOR TRACKING ERROR AND MONOPULSE SLOPE CONSTANT CALCULATION 83
B.2. MATLAB CODE WITH DIGITAL BEAMFORMING FOR TRACKING ERROR AND MONOPULSE SLOPE CONSTANT CALCULATION 86
C. MATLAB CODE FOR ARRAY ANTENNA SUM AND DIFFERENCE PATTERN DISTRIBUTION 89
D. MATLAB CODE FOR RANGE CALCULATION FOR DIFFERENT BIT RATES 91
E. MICROWAVE STUDIO SIMULATED PATTERNS OF THE GROUND PLANE 93
F. MATLAB CODE FOR CHARACTERIZING THE DEMODULATORS AND THE FIGURES OF THE MATLAB CODE 95
G. MATLAB CODE FOR FINDING THE INTER-ELEMENT PHASE DIFFERENCES 104

LIST OF REFERENCES 107

INITIAL DISTRIBUTION LIST 111

LIST OF FIGURES

Figure 1 The original design of the array antenna by Guglielmo Marconi. This antenna was destroyed by very strong winds on September 17, 1901. [1].....2
Figure 2 The cooperation among the elements of a UAV system. [8].....6
Figure 3 One of the four faces AN/SPY-1D phased array radar. [10].....10
Figure 4 The outputs of a lobe-switching antenna pattern. (After [9].) 11
Figure 5 Conical-scan tracking. [9].....12
Figure 6 Two squinted antenna beams in polar and rectangular coordinates. (After [9].).....13
Figure 7 The sum and difference patterns of an array antenna. 14
Figure 8 Normalized Δ/Σ vs. pattern angle. [12].....15
Figure 9 Noise contribution to the monopulse pattern. Half power beamwidth is entered as 16 degrees. 17
Figure 10 (a) Plane wave from A incident on the antenna. (b) Plane waves from three different sources incident on the antenna. (After [9].).....19
Figure 11 (a) Geometry of radar multipath tracking. (b) (c) Elevation difference pattern or multipath error computation. (After [11], [13].).....22
Figure 12 Element Spacing (*d*) for no grating lobes vs. Scan Angle (θ_s). 26
Figure 13 Element spacing (*d*) vs. gain for isotropic elements (no scan) based on Eq. (13). 28
Figure 14 Drawing of the array and ground plane. 29
Figure 15 Gain vs. number of elements. 30
Figure 16 Scan angle (θ_s) vs. half power beamwidth.....31
Figure 17 UAV tracking by the array located at *x*=0. 32
Figure 18 Angular difference (tracking error) vs. time for a UAV 1000 m downrange at a speed of 30 m/sec. 33
Figure 19 Array antenna sum and difference pattern distribution.....34
Figure 20 Angular difference (Tracking Error) vs. time for a UAV 1000 m at a speed of 60 m/sec. 37
Figure 21 Angular difference (Tracking Error) vs. time for a UAV downrange 1000 m at a UAV speed of 90 m/sec. 38
Figure 22 Illustration of reception of a linearly polarized incident wave by a linearly polarized receiving antenna. (After [15].).....40
Figure 23 The top view of the ground plane and an array of dipoles modeled in CST Microwave Studio. [19] 42
Figure 24 The bottom view of the ground plane and an array of dipoles modeled in CST Microwave Studio. [19].....43
Figure 25 The sum pattern of the array of dipoles with ground plane modeled in CST Microwave Studio (broadside). [19].....44
Figure 26 The scanned sum pattern of the array of dipoles with ground plane modeled in CST Microwave Studio, scanned 40° from broadside. [19] 44

Figure 27 The difference pattern of the array of dipoles with ground plane modeled in CST Microwave Studio (broadside). [19].....45
Figure 28 The scanned difference pattern of the array of dipoles with ground plane modeled in CST Microwave Studio, scanned 40° from broadside. [19] 45
Figure 29 Block diagram of the array. 48
Figure 30 One of the printed circuit dipoles used in the array. 48
Figure 31 LNA-2700 by RF Bay, Inc.....49
Figure 32 Quadrature demodulator recovers both the in-phase and quadrature phase components of the input signal. [21].....50
Figure 33 AD 8347 Quadrature demodulator by Analog Devices. 51
Figure 34 LO Configuration. 52
Figure 35 NI cRIO-9215 Analog Input Module. [24] 53
Figure 36 The reconfigurable chassis NI cRIO-9104 with the real-time embedded controller, cRIO-9004 and analog input module, NI cRIO-9215. 54
Figure 37 The demodulator setup. [25] 55
Figure 38 Phasor In-phase and Quadarature-Phase plane. 58
Figure 39 The setup for deviation from linear phase measurement for 4-way splitters...59
Figure 40 Specification of the anechoic chamber at the Naval Postgraduate School. Monterey, CA (Spanagel Hall Room 604) [27].....62
Figure 41 LabVIEW Software Data Flow Diagram. 64
Figure 42 Transmitted phase vs. received phase for each demodulator with an LNA.....67
Figure 43 The approximate linear curve fit received phase vs. transmitted phase. 68
Figure 44 The measured received phase vs. transmitted phase after the phase offsets are subtracted. 68
Figure 45 Measured array antenna sum and difference pattern distributions for broadside excitation when the beam is scanned. 69
Figure 46 Calculated array antenna sum and difference pattern distributions for broadside excitation when the beam is scanned. 70
Figure 47 The block diagram of host VI. 71
Figure 48 The front panel of host VI showing array sum and difference amplitudes (left), beam scan angle (upper right) and pointing correction (lower right). ...72
Figure 49 a) The front view of the current system configuration. b) The back view of the current system configuration. 75

LIST OF TABLES

Table 1 Parameters for use in computing the directivity of uniform current amplitude. Equally spaced linear arrays. [15].....28

Table 2 Bit Rates and minimum sensitivity level equivalents vs. range for an ERP of 1 W. (After [16].).....36

Table 3 The parameters measured for each demodulator. 58

Table 4 The phase differences for each port on both 4-way splitters. 60

Table 5 The parameters remeasured for each demodulator when integrated in the system. 66

Table 6 The phase differences in degrees with respect to the reference demodulator, D1. 67

THIS PAGE INTENTIONALLY LEFT BLANK

ACKNOWLEDGEMENTS

I would like to express my gratitude to Professor David C. Jenn for his help with my thesis and to have trusted me by assigning for this thesis. He was always patient, time-giving and information sharing. His sense of humor and sound knowledge about electromagnetics and its applications gave me the confidence I needed.

I would like to thank Robert D. Broadston, the manager of the microwave laboratory of Naval Postgraduate School for accepting to be my second reader. He is an engineer who managed to mix practices and theories of electronics in the same pot. He helped me with my research set-up and taught how to be a practical engineer.

I would like to thank my friend, Selcuk Hosoglu who helped me with his endless programming ability.

My parents, Ulfet Gezer and Ersan Gezer, and my brother, Bulent Gezer for having supported all my decisions all along my life and let me be myself without judging me. I could not be successful without them.

I would like to thank my girl-friend, Yvette, for her never-ending patience with my not having made enough time for her and support throughout my research.

I would like to thank Turkish Naval Commandership to give me the opportunity to get my master's degree in Naval Postgraduate School and Turkish Nation to pay for my tuitions with their taxes.

THIS PAGE INTENTIONALLY LEFT BLANK

I. INTRODUCTION

A. BACKGROUND

The state-of-art technologies keep generating new ways of improving on the performance of the old systems. Array antennas, one of the continuously improving technologies, brought many benefits to our life. The superiorities of array antennas include the digital and computerized processing capabilities that can be built into them. Digital phase shifting to form a beam is one of the best advantages of array antennas. Array antennas have electronic and rapid beam scanning ability, and they have broadband potential. The low sidelobes and the narrow beams of the antennas give a very low signature that provides a lower probability of intercept. The low sidelobes can also minimize the mutual interference effects of the antennas among each other. Multiple, simultaneous beams can be achieved by the means of *digital-beam forming* (DBF). Error correction and self calibration can be done easily in the signal processing. DBF also allows us to direct the nulls in the pattern in the direction of noise jammers, and also suppress clutter which is a cause of degradation in range. DBF also gives the opportunity to compensate for the failure of the elements in the array. Different data rates, depending on the operating environment, can be achieved with DBF. The array antennas can be used in many application such as communications, data-links, radar (search and track), and electronic warfare (EW). This gives perhaps the most important advantage of these antennas, the *multi-functionality*.

Today, there is a big improvement going on in the field of unmanned aerial vehicles (UAVs). UAVs prevent pilot loss of life. They carry out a variety of military and civilian missions such as surveillance and reconnaissance, target recognition, battle damage assessment, EW, search and rescue, and traffic monitoring. An important use of the UAVs is troop support, carrying out reconnaissance and surveillance missions, which requires maintaining a data-link with troops in order to send any data collected, such as video images, or audio.

During operations it is necessary to continuously maintain a data and control link with the operator. This requires the ground station antenna to track the UAV so the an-

tenna beam is pointed properly. The purpose of this research is design and build an array to angle-track a UAV and, eventually, to accomplish the data transfer from the UAV to the ground station. The antenna type on the UAV is not a subject of this research and it will be assumed to be an ordinary dipole. What is of concern is the array system that will be designed to achieve the purposes that were just mentioned.

Why is an array antenna selected for this application? The narrow beam of the antenna must be kept on the UAV as it moves and maneuvers. The beams of an array can track without physically moving the antenna. Array antenna systems can be reconfigured and different beamwidths can be used depending on the UAV path and the data rate desired for the type of operation. Array antenna systems can track and follow more than one UAV at a time (*multiple tracking*).

The first array antenna in history, shown in Figure 1, was designed and built by Guglielmo Marconi in 1901. This array antenna transmitted the first transatlantic wireless signal from Poldhu, Cornwall, U.K., to another identical array antenna in Cape Cod, Massachusetts, maintaining a two-way communication system. [1]

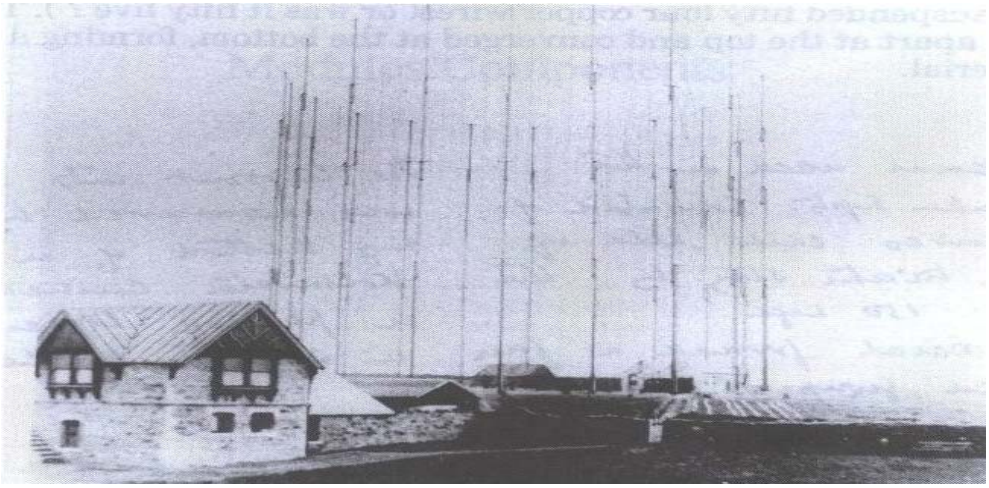

Figure 1 The original design of the array antenna by Guglielmo Marconi. This antenna was destroyed by very strong winds on September 17, 1901. [1]

Since 1901, scientists have made great progress in array antenna technology. Arrays have been increasingly common, with types that vary from linear to planar to conformal. Digital array applications have given arrays the capability to steer the main beam

electronically rather than mechanically. If the radiating elements of the array are excited by the relatively phased currents, the array is called a *phased array*. The main beam of these types of arrays can scan the desired field continuously. Phased arrays are particularly used in radars, but are gaining wider use in communications applications.

Nowadays, countries are getting more interested in phased array radars for their navies. One of the most advanced naval phased array radars is the Lockheed Martin AN/SPY-1D three-dimensional fixed phased array tactical radar, which is a four-faced array operating within the AEGIS combat system on Arleigh Burke class destroyers. The electronically steered phased array radars have many advantages because of their special features, which are summarized below. The advantages also apply to arrays used in communication systems.

1. These phased arrays can scan rapidly and agilely with a narrow beam, reducing the possibility of the system getting jammed. Likewise, the side lobes are lower compared with those of the conventional arrays, an advantage against side lobe jamming.

2. The power radiated can be adjusted for each element when each element has its own transmitter. Even though it increases the cost, it is an efficient way of controlling the radiated power in sectors, especially where emission control and cosite interference are a concern.

3. The phased arrays can serve multiple UAVs by either scanning one single beam rapidly or producing multiple, independent beams. This would also increase the dwell time which is the time on each UAV.

4. Phased array technology permits solid-state transmitters and monolithic technology to design the arrays. Monolithic microwave integrated circuits (MMIC) are projected to reduce the cost of the transceiver elements of an array.

5. The antenna elements of the arrays can be designed to conform to the ship structure, for example, like a microstrip patch antenna. This design would

reduce the RCS of the platform. Likewise, the aperture illumination can also be managed wisely to achieve the RCS reduction goal.

6. Because there are often hundreds of elements in an array, damage or defects on some elements do not shut the system down entirely. But, there is a graceful degradation.

7. Electronic beam steered phased arrays do not have any mechanical rotation components, and electronic modules can be replaced more easily and quickly without the need to return to a shipyard for maintenance.

8. A single phased array can serve several systems. This feature of phased arrays removes the need for individual antennas for each system and reduces the RCS arising from the extensions on the ship mast and structure.

The frequency bandwidth is a major design challenge for the array system. Even though current array radars are expected to be multifunctional, it is a fact that different functions need different bands. Multifunction radars can be used for surveillance, tracking, communications, direction finding and weapon guidance purposes. The radars should be designed in lower bands in order to increase range. The AN/SPY-1D operates in S band. Current electronic support equipment operates within the range from 2 to 20 GHz. But, especially in littoral waters, it is very hard for electronic warfare operators to detect radars operating in the UHF band because of the dense electronic environment.

The complexity of the design of phased array radars increases their cost. Designers have been trying to overcome this difficulty by finding some commercial-off-the-shelf (COTS) components that could be used in the system. The eventual aim of radar engineers is to decrease the cost of phased array antennas without sacrificing performance.

B. PREVIOUS WORK

This research is part of an ongoing project started with the thesis by Bartee. [2] Esswein [3] continued the work and demonstrated the feasibility of building a digital phased array with available COTS hardware. Esswein constructed a 24-element, three-dimensional, dual-ground plane, active phased array. The Genetic Algorithm (GA) was

used to determine the element excitations, and the measured radiation beam was in agreement with the theoretical calculations. The modulator feeding each printed antenna element used for this array was the Analog Devices AD8346EVAL quadrature modulator board, which is now being incorporated into a transmit receive (T/R) module for radar applications.

Eng [4] examined the operating characteristics of the COTS modulator and demodulator for digital phased array applications. He added an Analog Devices AD8347EVAL quadrature demodulator board to the test setup already made by Esswein. The demodulator board was successfully configured to operate as a phase shifter. The demodulator receives the signal sent by the modulator, and phases were measured via the *In-phase (I)* and *Quadrature (Q)* voltages. A periodic phase error was identified and attributed to the phase error inherent in the modulator boards.

Ong [5] focused on the receiver part of the project and investigated the periodic phase error attributed to the modulator boards. After modifying the bias voltage conditions that were used, the periodic phase errors disappeared. The phase difference between the received and transmitted phases was acceptably small. Ong also investigated a technique of using different types of time-varying phase weights for a linear frequency modulated signal on both transmission and reception in order to improve the phase distortion and increase the operating bandwidth of the phased array. Results showed that using time-varying phase weights improves the signal-to-noise ratio performance.

Yong [6] continued by examining the phase relationship between the AD8346EVAL modulator and AD8347EVAL demodulator boards. He studied the distribution of the local oscillator (LO) to two AD8346EVAL modulator boards in a wired and wireless setup. This has been the first step towards a fully wireless phased array. The digitization and synchronization of multiple receive modules was another point of interest, and digitization of the direct downconverted I and Q voltages was achieved by implementing NI5112 digitizers.

Dr. Kevin Jones from the Naval Postgraduate School (NPS) is also working on a tracking UAVs. He is using mechanical tracking with GPS data from the UAV to tell the antenna where to point. This is considered a closed loop system. The antenna is pointed mechanically. [7]

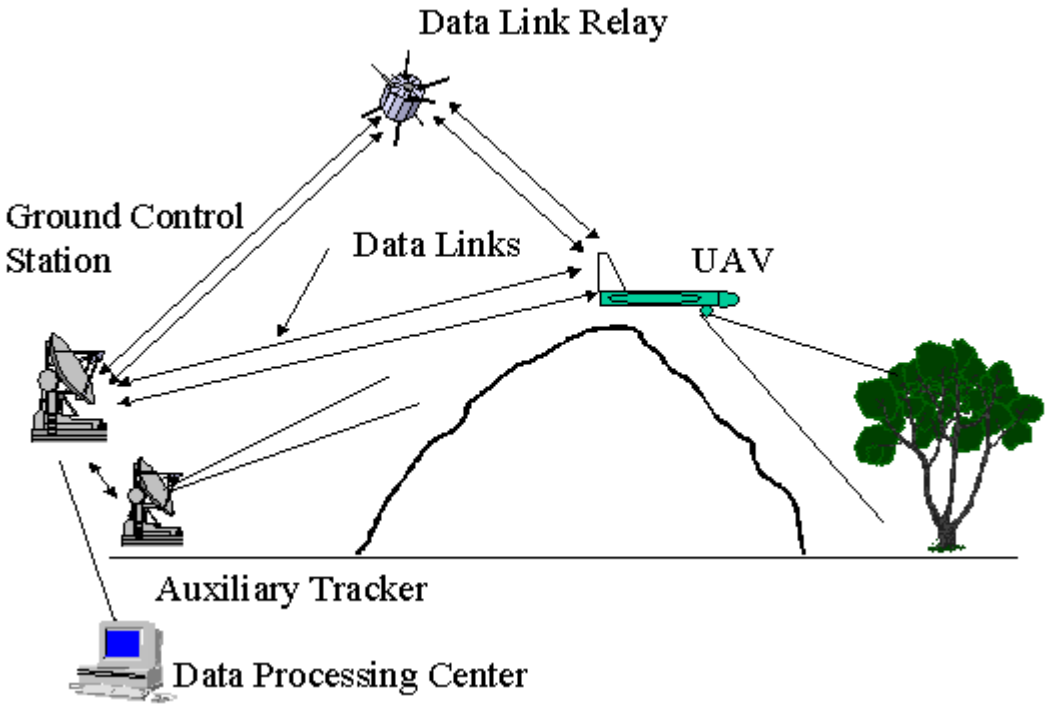

Figure 2 The cooperation among the elements of a UAV system. [8]

C. SCOPE OF RESEARCH

The state of art technology uses all the means to increase the information superiority and provide the decision makers with a well described tactical picture of the war scene. To achieve this, UAVs are being integrated into the network centric warfare elements. The UAVs can carry out many reconnaissance and surveillance missions and provide the necessary information to the troops as seen in Figure 2. As an element of the network, the ground control station of UAV systems exploits the improving technology. Array antennas are a very sophisticated means to accomplish an accurate UAV tracking and maintain a good data-link.

The research goal was to design and build a digital phased array for tracking UAVs and use the data and control signals from the UAV to point the antenna. The de-

sign is to incorporate the COTS hardware to reduce cost. Simulation is another way to reduce the cost of the design and comprehend the consequences of design changes before manufacturing and to see if it needs any adjustment. Thus, the design of tracking array antenna system is verified through the simulations. In our design, we also had the chance to demonstrate the critical technologies such as new COTS base station electronic hardware and special controller software compatible with the new hardware.

D. ORGANIZATION OF THESIS

Chapter II discusses the main principles of tracking antennas. The first section of this chapter mentions the tracking antenna types. In Section B, tracking techniques are presented and discussed. In Section C, the tracking errors degrading the performance of the tracking systems are explained. In Section D, the other external causes of errors are mentioned.

Chapter III addresses the overall tracking antenna design. Section A discusses the parameters that need to be considered in designing a tracking antenna system. After determining the design parameters, the tracking process is simulated in terms of the range and speed of the UAV that is expected. In Section B, the effect of polarization is studied for different cases. Section C presents a Microwave Studio simulation of the pattern on a ground plane for the array antenna.

Chapter IV discusses the fabrication and measurement setup and the tests made to verify the design of the array system.

Chapter V summarizes what was done in this research and gives recommendations for future work.

Appendix A includes the MATLAB code used to determine the design parameters of the system. Appendix B is the MATLAB code calculating the tracking error and monopulse slope constant. Appendix C is the MATLAB code for array antenna sum and difference pattern distribution. Appendix D is the MATLAB Code for calculating range depending on the data rate. Appendix E consists of the graphs showing *I* vs. *Q* values and transmitted phase vs. difference between received and transmitted phases for each board and MATLAB code written for this purpose. Appendix F gives the MATLAB code for

characterizing each demodulator and figures of this MATLAB code. Appendix G is the MATLAB code for finding the inter-element phase differences.

II. MAIN PRINCIPLES OF TRACKING ANTENNAS

The first section of this chapter discusses tracking antenna types. In Section B, tracking techniques are presented and discussed. In Section C, the tracking errors degrading the performance of the tracking systems are explained. In Section D, the other external causes of errors are mentioned.

A. TRACKING SYSTEMS

Radars can search the airspace and then track the desired targets in order to extract the azimuth, elevation, course and speed information from the movement of the targets. It enables the operator to predict where the target will be next. There are many types radar applications of tracking. Tracking antennas can also be used by weapon systems to aim the related weapons or guide the missiles. The search radars detect the target via their wide beamwidth and once the target is designated, the tracking radar, which could be another mode of the same radar system, tracks the target with its narrow beamwidth (i.e. pencil beam) of the tracking antenna. The subject of this thesis is not radar applications but the tracking of signals from UAVs, and thus of the UAV itself. It can be considered as the receiver side of a radar. Our tracking system is processing the signal the UAV transmitter sends.

Thus, it is necessary to mention tracking principles. Although there are many types of tracking techniques, they can be classified in four general categories:

- *Single-target tracker (STT)*: This tracks a single target continuously. It is a typical tracker for military applications (i.e. tracking of an aircraft or guided missiles). STT follows its target at a rapid data rate by the means of its antenna beam. It is a very accurate tracking system, because the obtained error signal is employed in a servo system in order to keep the error signal small. [9]
- *Automatic detection and track (ADT)*: ADT is integrated in most air-surveillance radars. It is an open-loop servo system and has a lower data rate than STT. Its advantage over STT is that ADT can track multiple tar-

gets (i.e. hundreds and even thousands of targets). [9] For radar applications, the difference between open-loop and closed-loop servo systems is that the position of the antenna is not dependent on the track data. In open-loop servo system the antenna rotates continuously, whereas closed-loop servo systems adjust the position of the antenna based on the track information.

- *Phased array radar tracking*: Phased array radars can track many targets on a time-shared basis with a higher data rate than the types of tracking radar mentioned above. It has the fast data rate of STT and multiple target tracking capability of ADT. Today, phased array radars are used not only for search, detection, and tracking purposes but also for communication and space tracking. AEGIS (SPY-1D) shown in Figure 3, Patriot, TPQ-36, APQ-164, SA-10, SA-12 and Erieye are among the modern phased array radar systems. [9]

Figure 3 One of the four faces AN/SPY-1D phased array radar. [10]

- *Track while scan (TWS)*: This radar can maintain track on many targets while scanning a limited airspace to find others. Since it deals with many targets, its accuracy can be said to be less precise than that of STT. TWS radars are used in an open-loop servo system and their data rate is moder-

ate. Today, this application has been absorbed by ADT, because, ADTs can carry out the functions of TWS, as well as other functions. [9]

B. TRACKING TECHNIQUES

There are three major methods that can be used to track a target: sequential lobing, conical scan, and monopulse tracking. Monopulse tracking will be discussed more than the other techniques because the phased array antenna design for this research uses the monopulse technique. But, it is important to understand the other tracking techniques as well to comprehend the main principles of tracking.

1. Sequential Lobing

This technique involves sequential switching between two beams with overlapping but offset patterns. Figure 4 shows the antenna output when a target is present, and the beam switched between two positions. Each position of the target on the beam corresponds to a voltage value. The rectangles A and B in Figure 4 are the beam position 1 and 2 returns respectively. The goal is to bring the target on the antenna boresight. The difference of the voltage amplitudes between the two positions gives the angular measurement error. The beam is moved to the direction in which the amplitude of the voltage is larger. If the amplitude of the voltages corresponding to the two positions of the target are the same, then the target is said to be on the switching axis.

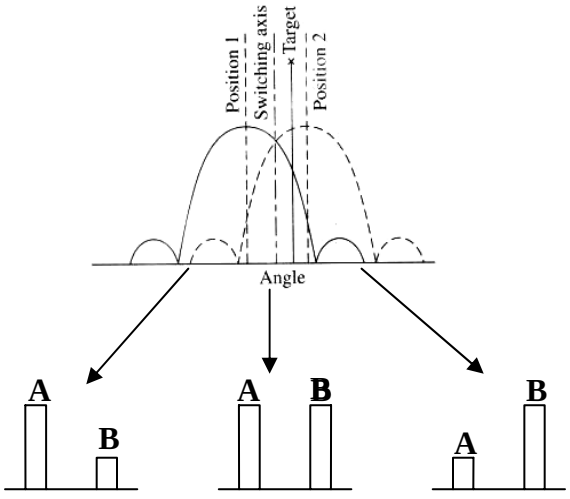

Figure 4 The outputs of a lobe-switching antenna pattern. (After [9].)

2. Conical Scanning

Conical scanning takes its name from the shape that a pencil beam makes by rotating the beam around an axis as seen in Figure 5. The angle between the rotating axis and the beam axis, where the gain of the antenna is greatest, is called a *squint angle*. The amplitude of the echo signal is modulated at a frequency called *conical scan frequency*. Conical scan frequency is actually the beam rotation frequency. This modulation occurs due to the rotation of the squinted beam and the target's offset from the rotation axis. The phase of conical scan modulation gives the location of the target. The error signal obtained from the modulated signal combines the elevation-angle error and azimuth angle error. These error signals are applied to elevation and azimuth servo motors to position the antenna. If the antenna is on target, the amplitude of conical-scan modulation is zero. [9]

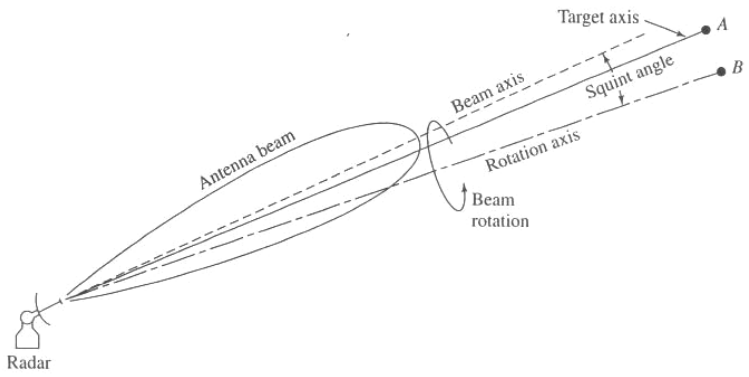

Figure 5 Conical-scan tracking. [9]

3. Monopulse Scanning

Monopulse scanning is the most efficient and robust tracking technique. The tracking techniques discussed above need more than one signal sample, theoretically four target returns, two of which are for the vertical direction and two for the horizontal direction, to determine the tracking error. The signals returning from the target will have different phase and amplitude due to the signal fluctuations. The fluctuations in the signal results in tracking errors. As evident from its name, monopulse scanning radars use only

one pulse to determine the tracking error. Using one pulse (single sample) eliminates the problem of signal fluctuation. [11] Several samples can be used to improve the accuracy of the angle estimate. [9]

Monopulse systems can be divided into two types; *amplitude comparison* monopulse systems and *phase comparison* monopulse systems.

a. Amplitude Comparison Monopulse Systems

Amplitude comparison monopulse is reminiscent of sequential lobing but in amplitude monopulse comparison systems, the beams are created simultaneously. There are two overlapping "squinted" [9] beams pointing in slightly different directions as seen in Figure 6. These two beams might be fed from separate feeds. The echo of the target is received simultaneously by both beams.

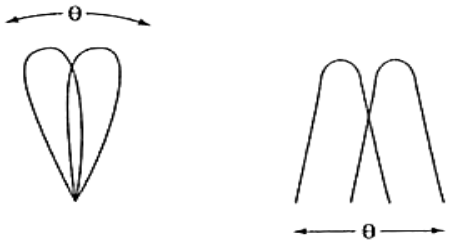

Figure 6 Two squinted antenna beams in polar and rectangular coordinates. (After [9].)

The two antenna outputs that help the system to track a target are the difference and sum of these two squinted beams. The monopulse systems use the sum pattern on transmit, whereas the sum and difference patterns are used together on receive. Figure 7 shows typical sum and difference patterns for an array. As discussed in sequential lobing, the position of the signal on the difference beam corresponds to a nonzero voltage when it arrives off of the null. The difference of the amplitudes obtained from these two beams (i.e. the difference beam) gives the angular error. If the phase of the sum pattern is compared to that of the difference pattern, the direction of the angular error is found.

From Figure 7, it can be observed that the nulls of the difference beam correspond to the peaks of the sum pattern and vice versa. The ratio of difference pattern

to sum pattern is used to generate the angle-error signal so that the null in the center of the difference pattern can be placed on the target. The tracking process uses the voltage ratio: [12]

$$\frac{\Delta}{\Sigma} = \frac{\text{difference voltage}}{\text{sum voltage}} \tag{1}$$

The complex voltage in Eq. (1) above can be separated to its real and imaginary components: [12]

$$\text{Re}\{\Delta/\Sigma\} = \frac{|\Delta|}{|\Sigma|}\cos\delta \tag{2}$$

$$\text{Im}\{\Delta/\Sigma\} = \frac{|\Delta|}{|\Sigma|}\sin\delta \tag{3}$$

where δ is the relative phase between sum and difference channels. Usually only $\text{Re}\{\Delta/\Sigma\}$ is processed because it defines the side of the null with the sign of the ratio, and the target information is found only in real part of the ratio.

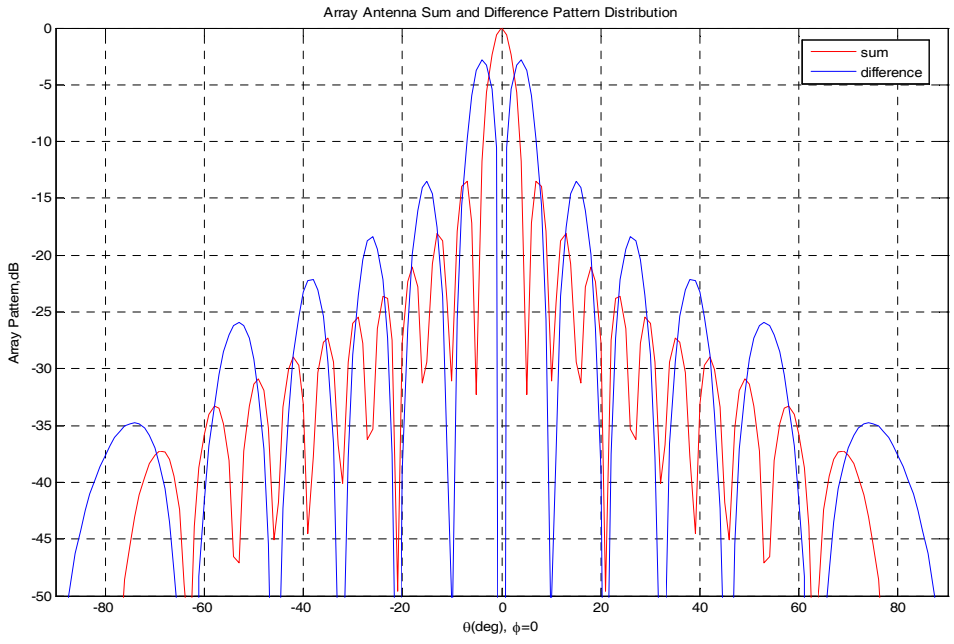

Figure 7 The sum and difference patterns of an array antenna.

The plot of the pattern angle versus normalized difference to sum voltage ratio near the null corresponding to boresight or scan angle of the antenna is shown in Figure 8.

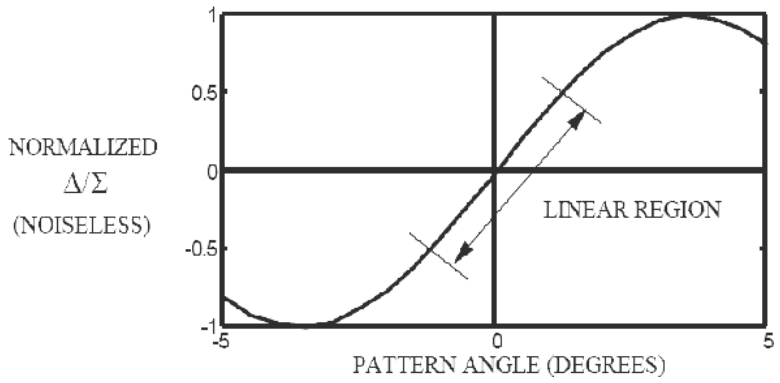

Figure 8 Normalized Δ/Σ vs. pattern angle. [12]

The target is tracked when it is positioned within the difference null of the beam, which is seen in the center of the pattern shown in Figure 7. The slope in the linear region in Figure 8 is used to create an error signal, which makes the difference null move to position of the target within the null. This ratio is proportional to the multiplication of the slope constant with the pattern angle in degrees as: [12]

$$\frac{\Delta}{\Sigma} \approx k_s \theta, \quad |\theta| \le \theta_B / 4 \tag{4}$$

where θ_B is the half power beamwidth, and k_s is the monopulse slope constant. The tracking system of this UAV application will be an amplitude comparison monopulse system and will exploit the principles mentioned above.

b. Phase-Comparison Monopulse Systems

The second monopulse tracking technique is called phase-comparison. It was invented in World War II about the same time as the amplitude-comparison monopulse systems. [9] This kind of monopulse system is similar to the amplitude-comparison monopulse system, but the two antenna beams point in the same direction. Hence, the projection of the target on each beam and the amplitudes of the returns from the target received by each of these antennas are the same. This is the main difference of

the phase-comparison monopulse systems from amplitude-comparison ones. The other difference is that two beams in a phase-comparison monopulse system are not squinted, as it is the case in the amplitude-comparison monopulse systems. [9] The distance of each antenna beam to the target generates a phase difference which also gives an angular error, and this angular error corresponds to an error signal.

C. TRACKING ERRORS

The measure of error is the root mean square (rms) of the difference between the measured angle (estimated) values and the true values. The tracking errors can be divided into two main groups: range tracking errors and angle tracking errors. The antenna system which is subject of this thesis is an angular tracking antenna. Hence, range tracking errors will not be discussed in this report. Even though some types of errors discussed below cannot be encountered in monopulse radar systems, it is good to know the reasons of these kinds of errors in order to understand the nature of tracking accuracy limiting factors. Thermal noise, angular glint (angle noise), scintillation, manufacturing qualities and alignment are factors contributing to angular tracking errors. There are some more errors caused by external factors, which will be discussed in Section D.

1. Thermal Noise

Thermal noise is a very important factor degrading the performance of the system and limiting the accuracy of the angle measurements. Noise is a function of probability as well. As will be discussed, if the Friis equation is divided by the noise power, the signal-to-noise ratio (SNR) is obtained. It is seen that the signal-to-noise ratio is inversely proportional to the square of range. This relationship in the well-known Friis equation gives the limiting effect of noise on radar in terms of range. Thermal noise also contributes to angular error as shown in Figure 9. When thermal noise fills the null, the target can only be located to an angle $\Delta\theta_t$.

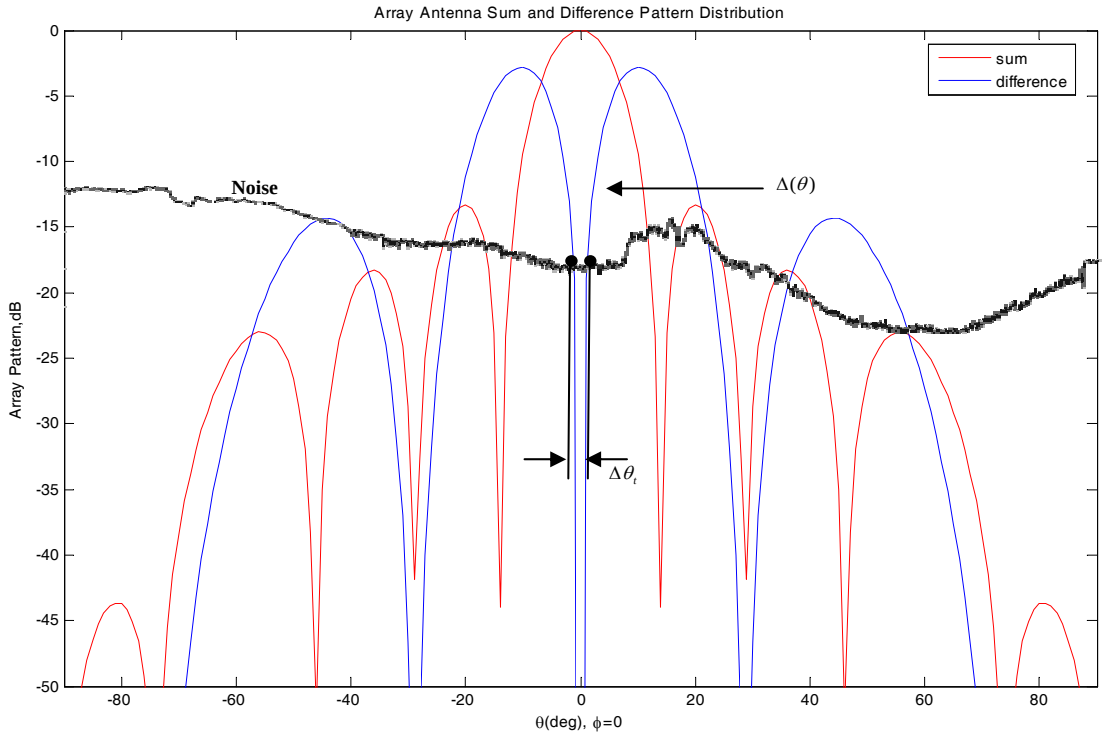

Figure 9 Noise contribution to the monopulse pattern. Half power beamwidth is entered as 16 degrees.

The angular rms error in a tracking radar due to thermal noise can be calculated with the general formula: [11]

$$\sigma_t = \frac{k\theta_B}{k_s\sqrt{B\tau(S/N)(f_p/\beta_n)}} \tag{6}$$

where k=1 for a monopulse and 1.4 for a conical-scan, θ_B is the half-power beamwidth, S/N the signal-to-noise ratio, f_p pulse repetition frequency, and β_n servo bandwidth. The product of B (bandwidth) and τ (pulse width) is approximately equal to unity, and $f_p/2\beta_n$ gives the number of pulses integrated. The constant k_s seen in the denominator is the monopulse slope constant, which is approximately equal to 1.7 for monopulse radars and 1.3 for conical-scan radar. However, its exact value must be determined for the specific antenna used in tracking.

2. Angular Glint

A source of angle tracking error is angular glint, also called *angular noise*, *angle scintillation*, *angle fluctuations,* or *target noise*. The tracker determines the direction of the vector sum of all signals arriving. Glint is the difference in the apparent location compared to the actual. Sometimes it can even result in tracking points off the target. For the communication case, the equivalent of glint can occur from multipath, especially from points on the UAV as shown in Figure 10. The center of gravity of the UAV is usually chosen as a reference. The tracker angle-sensing devices sense the phase front of the UAV transmitted wave and indicate the source to be in a direction normal to the wavefront. For a single source, the wave arrives at the antenna in the form of a uniform planar wave. Thus, the incident wavefront is tilted with respect to the antenna base line as seen in Figure 10(a). The spread of the scatterers on the UAV leads to multipath and the angle measurement gets worse. The vector sum of these incident wavefronts give a wavefront whose amplitude and phase is not uniform across the antenna aperture.

Glint can be a major problem in angle measurements especially for short ranges. Angle noise is an issue on the performance of all the continuous tracking radars with closed-loop angle tracking whatever tracking type it has. [9, 11]

The rms error of the angular location of the point on the target with respect to the center of the scatterer can be calculated by [13]

$$\sigma_g = \frac{1}{R}\sqrt{\frac{1}{2}\sum_i L_i^2 k_i^2} \tag{7}$$

where the error is in radians, L_i is the distance to the i^{th} scattering point and $k_i \ll 1$ is the ratio of the i^{th} signal component amplitude to that of the main element.

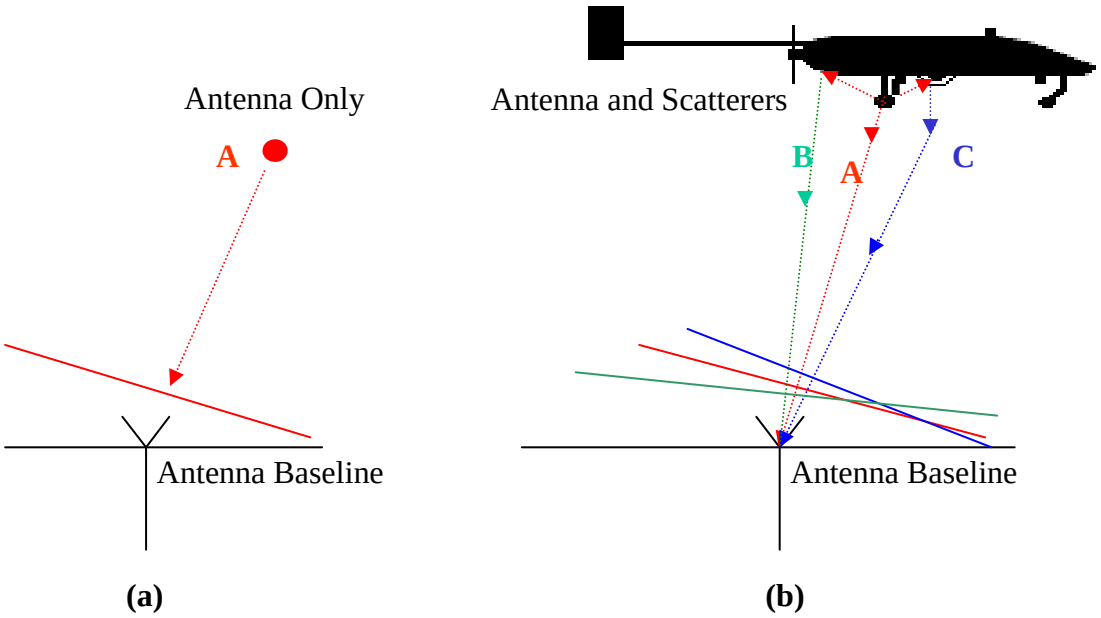

Figure 10 (a) Plane wave from A incident on the antenna. (b) Plane waves from three different sources incident on the antenna. (After [9].)

3. Scintillation

The angle error *scintillation* is usually encountered in conical-scan and sequential lobing tracking radars. As the UAV moves, its aspect with respect to the tracker also changes due to yaw, pitch, or roll. The transmission path is also changing: the atmospheric path and conditions. These changes cause a fluctuation in the amplitude of the received signal. As already discussed in Chapter II, Sections B.1 and B.2, the change in amplitude leads to the conical-scan and sequential lobing angle errors. These tracking systems direct the antenna to point normal to the incident wavefront, which is not the angle from the UAV itself. Hence, the change in amplitude due to the movements of the complex UAV degrades the tracking accuracy of these systems. This fluctuation, also known as *fading*, does not affect monopulse systems as severly as others. [9]

The rms value of this error is calculated approximately by: [14]

$$\sigma_s \cong 0.01\theta_B \tag{8}$$

where θ_B is the half-power beamwidth of the antenna. The factor shown in Eq. (8) is between 0.1-0.2 for track-while-scan (TWS) radars.

4. Manufacturing Quality and Alignment

The errors arising from antenna mismatches can be approximated by: [14]

$$\sigma_m \cong 0.005\theta_B \tag{9}$$

where σ_m is the rms manufacturing and alignment error. An angular error occurs due to the shift of the boresight with frequency. An alignment made at a certain frequency may shift by $0.01\theta_B$ to $0.001\theta_B$ at a different frequency. [14]

For some tracking systems other than the electronic beam steering modern phased arrays, the servo also produces some noise.

5. Total Error

Assuming independent error sources that are normally distributed, the total error of the system is the sum of the variances: [14]

$$\sigma_{at} = \sqrt{\sigma_t^2 + \sigma_g^2 + \sigma_s^2 + \sigma_m^2 + \ldots} \tag{10}$$

At long range, thermal noise will dominate while at short range, glint will dominate.

D. OTHER EXTERNAL CAUSES OF ERROR

Some factors causing errors in the radar performance might be due to some external reasons such as multipath, crosstalk caused by cross-polarized energy, and tropospheric refraction.

1. Multipath

Multipath is a phenomenon occurring as a result of the signal reflecting from the other objects or from terrain such as land, ocean, or sea. This reflection causes the signal returned by the target to arrive from different paths and enter the antenna from different points on its main beam or sidelobes. This situation can be considered as a type of glint. However, in this case the scattering arises from sources in the environment as opposed to sources on the UAV. This difference can be seen in Figure 11(a). If the extension that could be drawn from the reflection point in the direction of the arrow intersects a line

drawn at the same altitude of the target in the opposite direction, it gives the image of the target. It confuses the tracker, which tracks the combination of the true target and the image.

Both elevation and azimuth tracking performance can be degraded by the errors due to multipath. The ocean surface can contribute errors to elevation tracking whereas buildings or rough surfaces, which cause diffuse scattering, contribute errors to both azimuth and elevation tracking. [11] The lower the altitude of the target, the bigger the multipath errors. Hence, low angle tracking causes big multipath tracking errors.

An rms value of the multipath error is calculated from: [11]

$$\sigma_E = \frac{\rho \theta_B}{\sqrt{8 G_{se}(peak)}} \tag{11}$$

where ρ is magnitude of surface reflection coefficient, θ_B is antenna beamwidth, and $G_{se}(peak)$ is the power ratio of the tracking antenna sum-pattern peak to the error-pattern peak sidelobe level at the angle of arrival of the image signal. Figure 11 shows that $G_{se} = G_1 / G_4$. In order to neglect the reflection effect, this power ratio should be much greater than one.

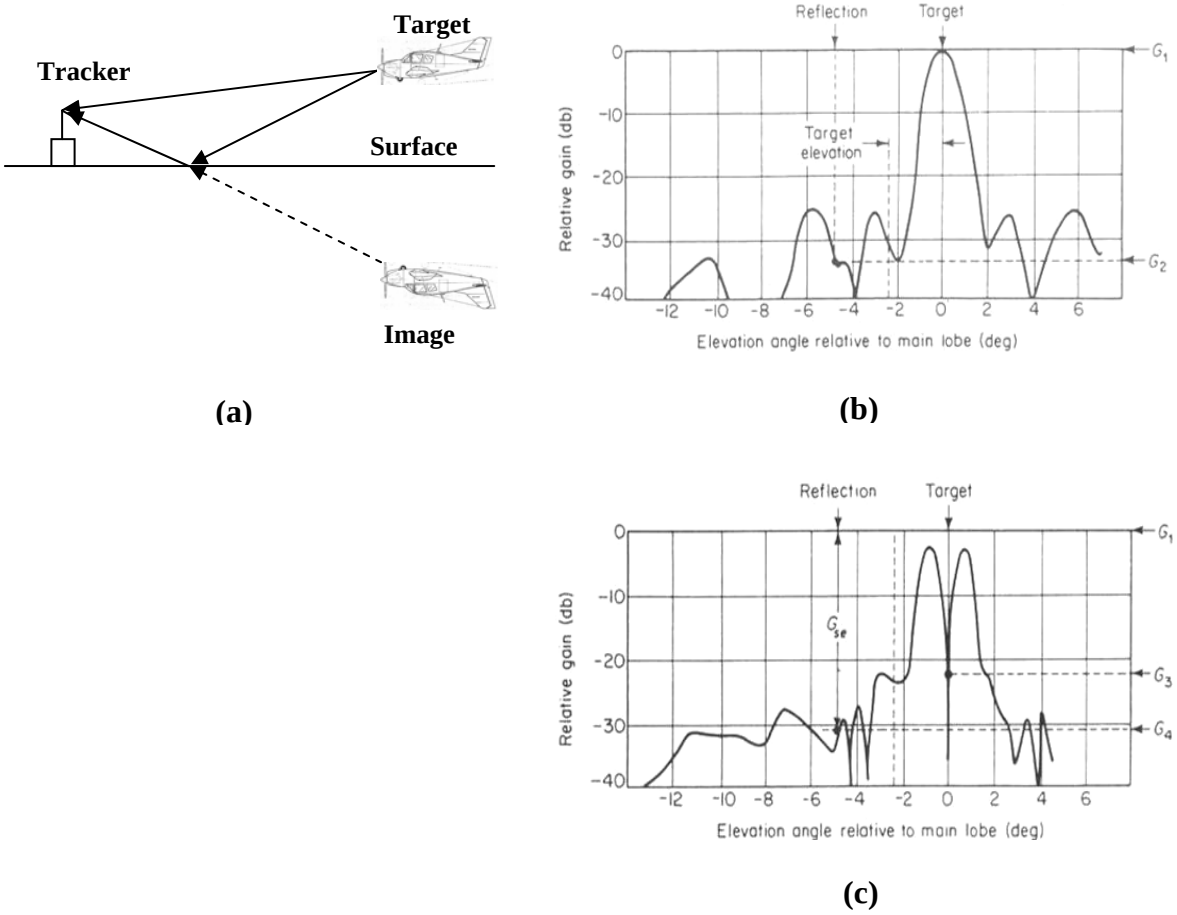

Figure 11 (a) Geometry of radar multipath tracking. (b) (c) Elevation difference pattern or multipath error computation. (After [11], [13].)

2. Crosstalk Caused by Cross-Polarized Energy

The cross-polarized energy of the source causes *crosstalk.* The azimuth error causes output from the elevation-error detector, and vice versa. Crosstalk is called *cross coupling*. This effect is generally negligible and can be overcome with good antenna design. In some situations, it could be significant, so that the crosstalk can cause a large tracking error and even the loss of track.

3. Troposphere Propagation

The troposphere is within the altitude between 0 through 10 km of the surface and is not homogeneous. The variations in density of the air in the troposphere cause random beam bending. Clear air, dry air, heavy overcast, thin clouds or thick cumulus clouds can be counted among these formations. The worst scenario is heavy cumulus clouds which form columns of shaded air in troposphere. These shaded air columns are cooler than the air surrounding them and have different dielectric constants. The radiated energy passes through these shaded air columns and result in beam bending. This effect is valid as long as the beam of the antenna is within troposphere. [10] Tropospheric refraction can lead to a difference in the sensed direction from the bent ray and the actual direction. However, this error is not significant at standard atmosphere conditions and short range.

In this chapter, tracking systems were briefly described to show how they exploit various tracking principles. In Section B, the tracking techniques were discussed and in Section C and D, the tracking errors degrading the performance of the trackers and the external causes of errors were mentioned. The next chapter describes the design of a UAV tracking array.

THIS PAGE INTENTIONALLY LEFT BLANK.

III. TRACKING SYSTEM DESIGN CONSIDERATIONS

This chapter addresses the overall tracking antenna design. Section A discusses the parameters that need to be considered in designing the tracking antenna system. After determining the design parameters, the tracking of the system is simulated in terms of the range and speed of the UAV that is expected. In Section B, the effects of antenna polarization is studied for different cases. Section C discusses the results of a simulation made in CST Microwave Studio to see the effects of the ground plane on the array pattern.

A. DETERMINING THE DESIGN PARAMETERS

The array antenna system will be using the monopulse scanning technique to track the signal sent by the UAV. Before configuring the hardware of the system, the operating parameters need to be determined via some simulations. The parameters that need to be determined are element spacing, scan angle, half power beamwidth (HPBW), gain, number of elements, polarization and ground plane size. Designing a system is actually making a decision on what and how much to sacrifice, taking into account all aspects such as economical, material, and time constraints. The design process can be called an art of manipulating trade-offs. The first step in the antenna design is to write computer programs to examine the antenna performance as a function of various operational parameters.

The phased-array tracking antenna operates in the band from 2.4 to 2.5 GHz. The lowest frequency, which is 2.4 GHz, is selected for the calculation of most parameters. The wavelength is 0.125 m. One of the biggest concerns is the occurrence of *grating lobes*. Grating lobes that appear in the visible region might limit the performance of the antenna system. Grating lobes can be avoided if element spacing satisfies: [15]

$$d < \frac{\lambda}{1+\left|\sin\theta_{s_{\max}}\right|} \tag{12}$$

where $\theta_{s_{\max}}$ is the maximum beam scan angle with respect to the axis of the array. The maximum scan angle will be a function of the operating conditions. That is, the UAV ve-

locity and distance from the tracking array, its angle off boresight, and range. Programs were written to give graphs for different operating conditions. One of the graphs, which can be seen in Figure 12, shows the element spacing vs. scan angle. This graph is based on the highest frequency within the operating bandwidth. This graph gives an idea about the element spacing for no grating lobes for each scan angle. To estimate the required maximum scan angle the UAV range and velocity must be specified.

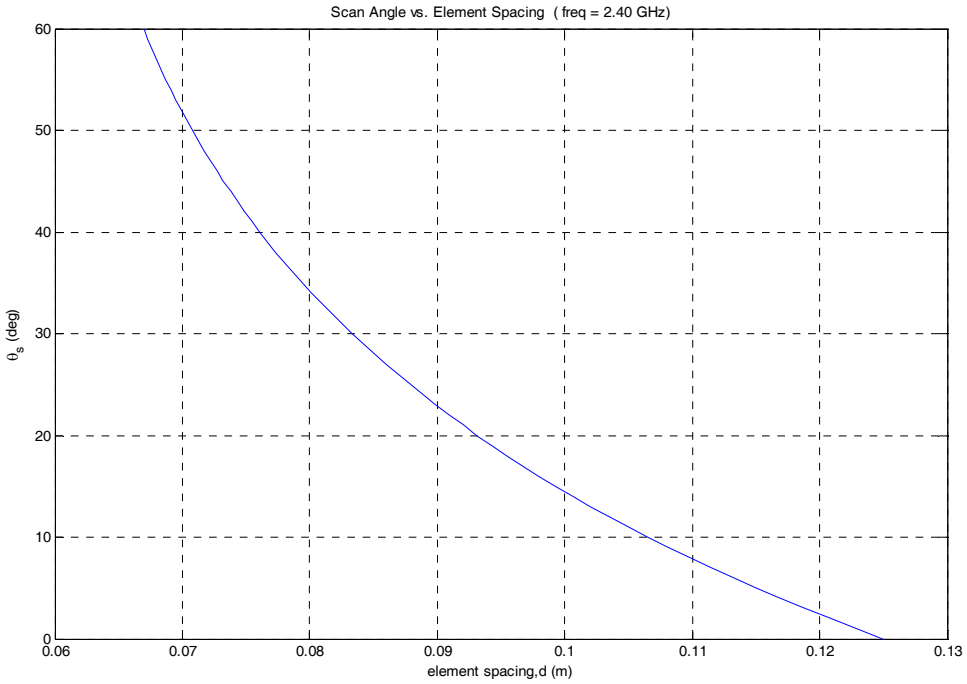

Figure 12 Element Spacing (d) for no grating lobes vs. Scan Angle (θ_s).

The element spacing and number of elements both affect the gain. More elements means higher gain and narrower beam width, but it also makes the design more expensive. Using National Instruments hardware, the number of slots for the demodulators is limited to multiples of four. To minimize cost, the fewest possible elements should be used. The signal that will be tracked needs to fall on the main null in the difference array pattern. To have a symmetric difference beam, the number of elements must be even.

The gain of the linear array can be calculated with the following formula: [15]

$$D = \frac{1}{\frac{a_o}{N} + \frac{2}{N^2}\sum_{m=1}^{N-1}\frac{N-m}{m\beta d}(a_1 \sin m\beta d + a_2 \cos m\beta d)\cos m\alpha} \tag{13}$$

where N is the total number of elements in the array and α is inter-element phase shift (which is zero for broadside). The factors in the formula above—a_o, a_1, and a_2—are given in Table 1 for several element patterns. The array will be using parallel dipoles, which are placed above a ground plane. The addition of the ground plane increases the gain about 3 dB above that predicted by Eq. (13).

Figure 13 shows a comparison between the element spacing and directivity, which is equal to gain for a lossless antenna. It can aid in a decision to define the element spacing. The vertical axis in Figure 12 gives the maximum allowed element spacing for each scan angle to avoid grating lobes. We can take any of the values below these maxima as the element spacing of the system, however, spreading the elements out (larger d) gives a narrower beamwidth. The directivity curves as a function of N for parallel short dipoles, shows a sudden decrease near one and two wavelengths (see Figure 13). This is the result of the grating lobes appearing in the visible region at the spacing of 1λ and 2λ, respectively.

The directivity of a broadside array of isotropic elements when there are no grating lobes is approximated by: [15]

$$D \approx 2\frac{L}{\lambda} = 2\frac{Nd}{\lambda} \tag{14}$$

where $L = Nd$ is the array length. The directivity of long arrays ($L \gg \lambda$) is primarily controlled by the array factor if the element pattern is of low directivity and its major lobe is aligned with that of the array factor. In cases such as these, Eq. (14) can be used. The actual array will have a small ground plane under the dipoles, giving a gain about 3 dB higher than predicted by Eq. (13) and (14).

Element Type	$\left\|g_a(\theta,\phi)\right\|^2$	a_o	a_1	a_2
Isotropic	1	1	1	0
Collinear short dipoles	$\sin^2\theta$	$\frac{2}{3}$	$\frac{2}{(m\beta d)^2}$	$\frac{-2}{m\beta d}$
Parallel short dipoles	$1-\sin^2\theta\cos^2\phi$ $=\sin^2\gamma$	$\frac{2}{3}$	$1-\frac{1}{(m\beta d)^2}$	$\frac{1}{m\beta d}$

Table 1 Parameters for use in computing the directivity of uniform current amplitude. Equally spaced linear arrays. [15]

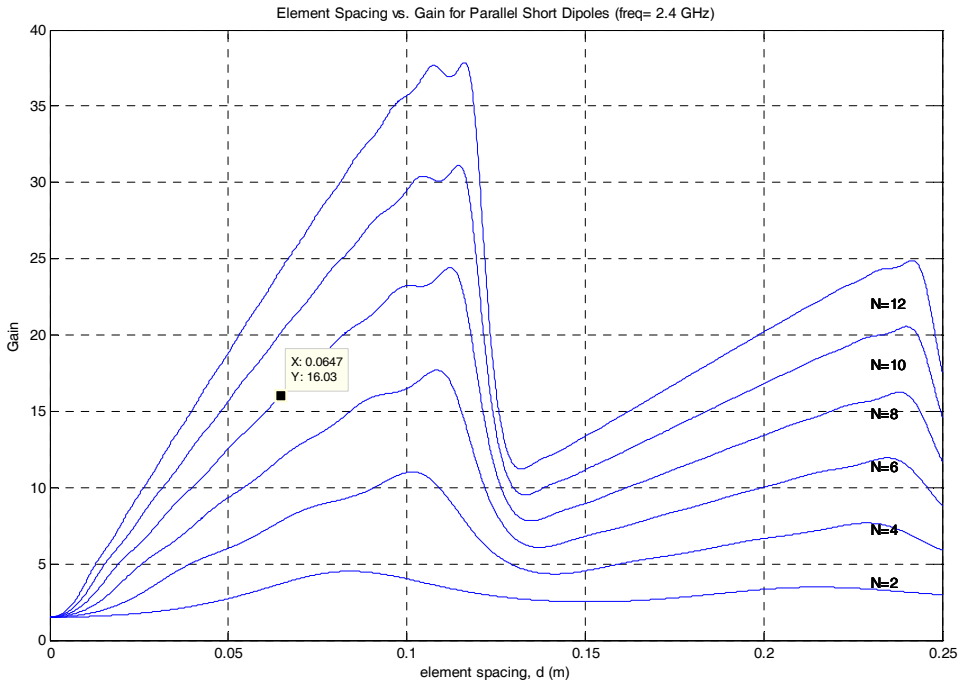

Figure 13 Element spacing (d) vs. gain for isotropic elements (no scan) based on Eq. (13).

Figures 12 and 13 can be used to make a decision on what the element spacing should be. Based on initial estimates of the UAV range and velocity, the maximum scan angle was estimated to be 40 degrees. This scan angle corresponds to a maximum spacing of approximately 0.073 m. Any value of element spacing below this prevents grating

lobes in the visible region. The determination of the element spacing does not only depend on the desired scan angle but also the gain and certainly on the economical considerations as discussed above. Taking into account all these considerations, the number of elements was decided to be between 8 and 12. The length of each antenna element (printed circuit dipole) is 0.09 m and element spacing is 0.065 m. It is decided to leave at least half a wavelength space (0.0625 m) between the edges of the elements and the sides of the ground plane. Dimensions of the ground plane allowed more space. The dimensions of the array ground plane on which the elements are placed are 0.215 m by 0.58 m as seen in Figure 14. The determined element spacing corresponds to a gain of approximately 16 for parallel short dipoles. Figure 15 shows that 8 elements give a gain of around 12 dB. With a ground plane, the gain will increase 2 to 3 dB. This issue will be addressed later.

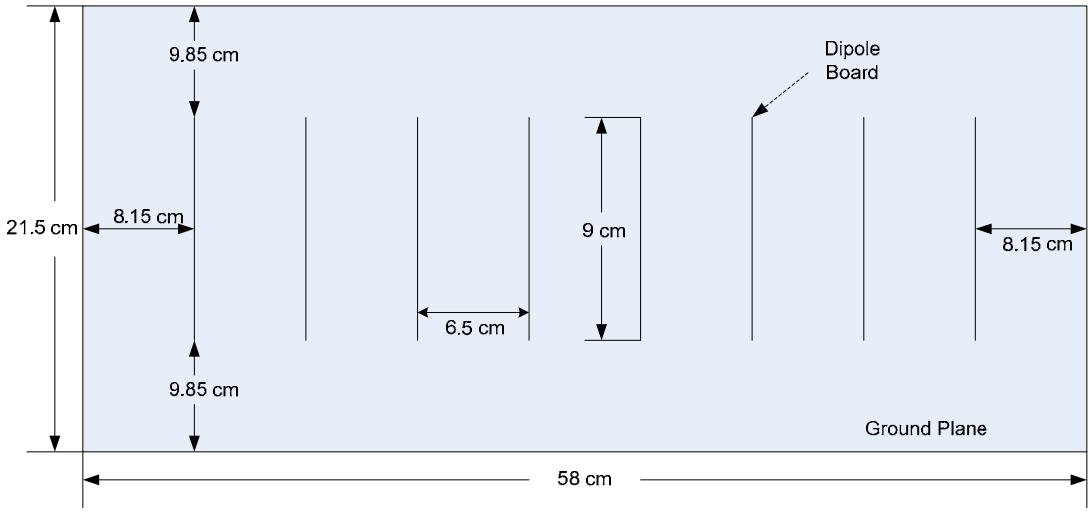

Figure 14 Drawing of the array and ground plane.

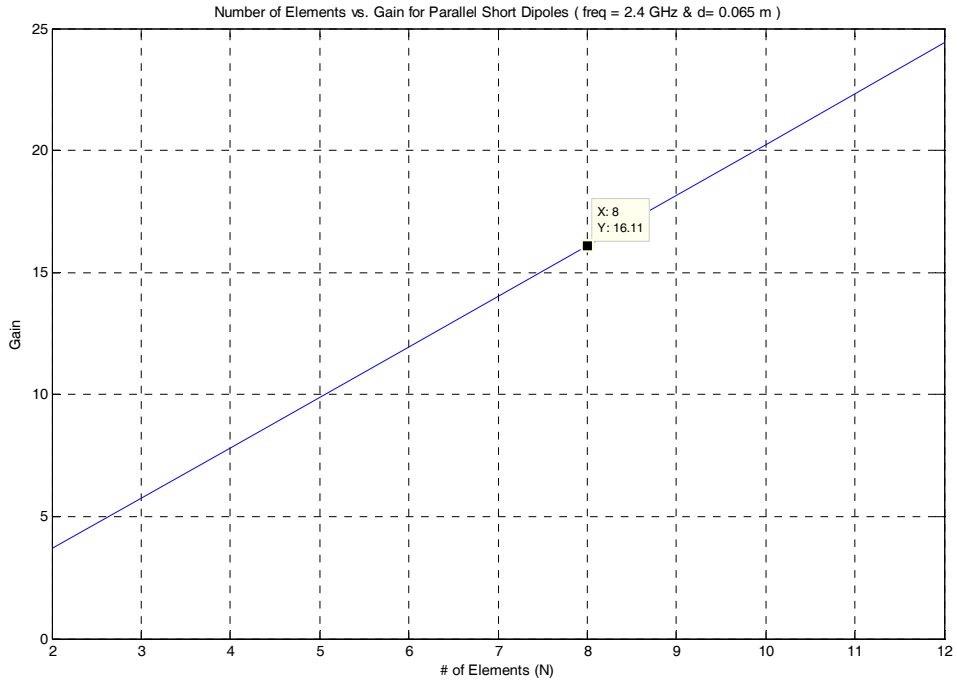

Figure 15 Gain vs. number of elements.

HPBW is another important parameter to consider. Figure 16 shows a graph giving the half power beam width vs. scan angle for various *N*. Beam broadening will affect the achievable accuracy of the tracking antenna at wide beam angles. In order to determine the half power beamwidth for various values of the number of elements, the element spacing and the scan angle was inserted in the MATLAB program. For a long ($Nd >> \lambda$) uniformly excited and equally spaced linear array, the HPBW is approximately: [15]

$$HPBW \approx 0.886 \frac{\lambda}{Nd} \sec \theta_s \qquad \text{near broadside} \tag{15}$$

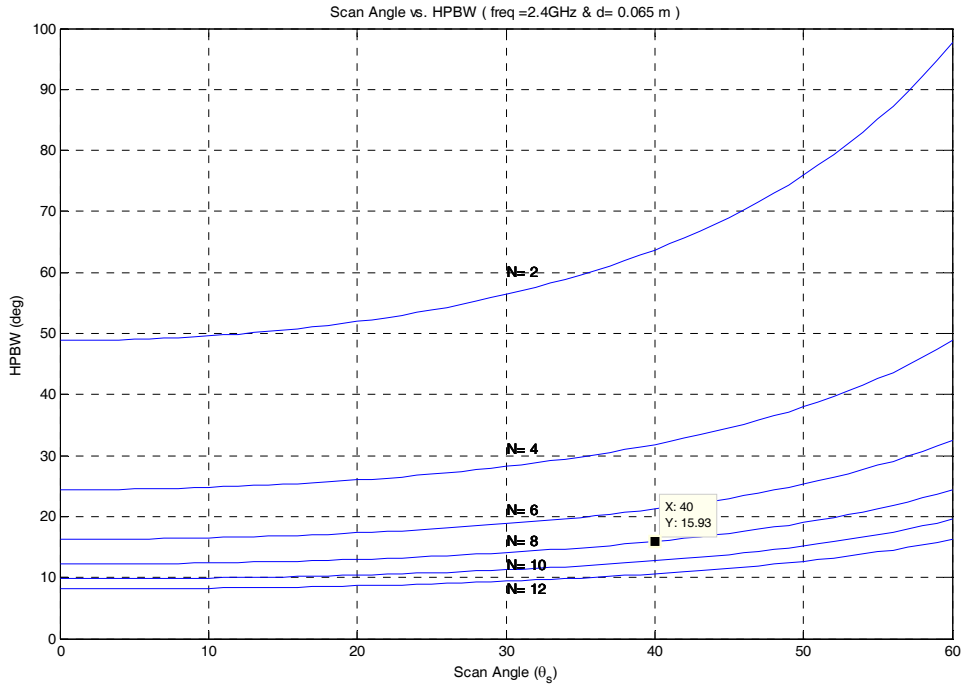

Figure 16 Scan angle (θ_s) vs. half power beamwidth.

The graph in Figure 16 consists of curves for even values of *N* from 2 through 12. A scan angle of 40 degrees with eight elements gives a half power beam width of about 16 degrees. This half power beamwidth is a good starting point for our system. Hence, the initial values for the scan angle, element spacing, and number of elements have been determined for our design.

The frequency is set at 2.4 GHz by the fact that this is the frequency used by the communication systems on the UAV. The scan angle was determined to be 40 degrees, and the half power beamwidth approximately 16 degrees, giving more than 12 dB of a gain for eight vertical dipole elements in the linear array. With a ground plane, the gain will increase to about 15 dB.

Based on all of these parameters, another MATLAB program was written to find the accuracy of our tracking system. The MATLAB code gives the difference between the tracking angle and actual angular position of the UAV over time. Current UAVs can reach to speeds up to Mach 4. Nonetheless, the speed of UAVs depend on the type of mission. Although the specific type of UAV for the system has not been defined yet, its

desired purpose is troop support, carrying out reconnaissance and surveillance missions, and maintaining a data-link with troops in order to send any data collected such as video, image, or audio. In light of this mission context, the UAV speed is likely to be between 10 and 90 m/sec. Initially, a UAV speed of 30 m/sec is assumed. From Figure 17, the range of the UAV is decided to be 1000 meters. When UAV is at θ=0, the range from the antenna to UAV is *R*= 1000 m. The antenna is stationary and UAV is assumed to be moving on a route perpendicular to the array. This short range puts more demand on the tracking system because the UAV moves through the beam rapidly.

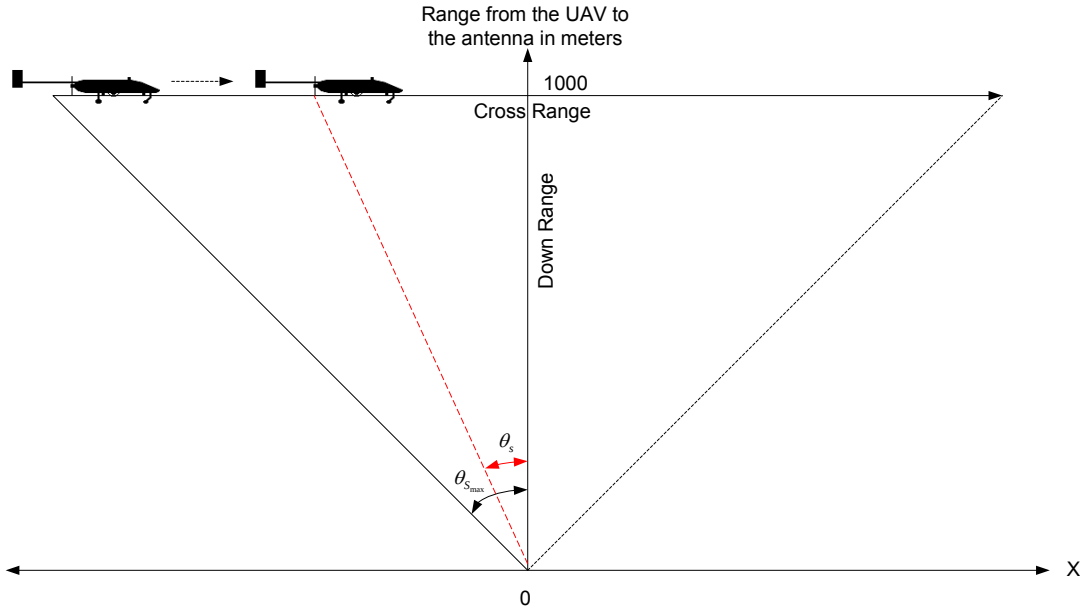

Figure 17 UAV tracking by the array located at *x*=0.

The MATLAB code uses the slope error constant formula, which is given in Eq. (4). The computed monopulse slope constant of the antenna is $k_s = -0.12003$ per degree. The resulting graph for the initial parameters (element spacing, number of elements, HPBW, frequency, scan angle) is seen in Figure 18. It takes approximately 44 seconds for a UAV with a speed of 30 m/sec to travel over a path the length of approximately 1700 m that is a function of the scan angle that was determined before; i.e. 40 degrees. The tracking error— the difference between the scan angle of the antenna and the actual angular position of the UAV—is a maximum 2.305 degrees when the target is near $\theta = 0^\circ$.

In order for a monopulse tracking system to track the target, it is supposed to be within the difference beam null, which is the region where the sum beam crosses over the difference beam on its each side. It has already been mentioned in Chapter II that the sum beam is used on both receive and transmit while the difference beam is used only on receive. As it can be seen in Figure 19, at the moment the error signal reaches its greatest value, e.g. when tracking (scan) angle is zero, the difference beam crossover is found to be 7 degrees. The linear region is less than this, so in the MATLAB code the difference beam linear region is limited to one-fourth of the sum beam HPBW on each side, i.e. -4 to 4 degrees. Consequently, the target is considered to be tracked by the antenna as long as the angular error is kept within these limits.

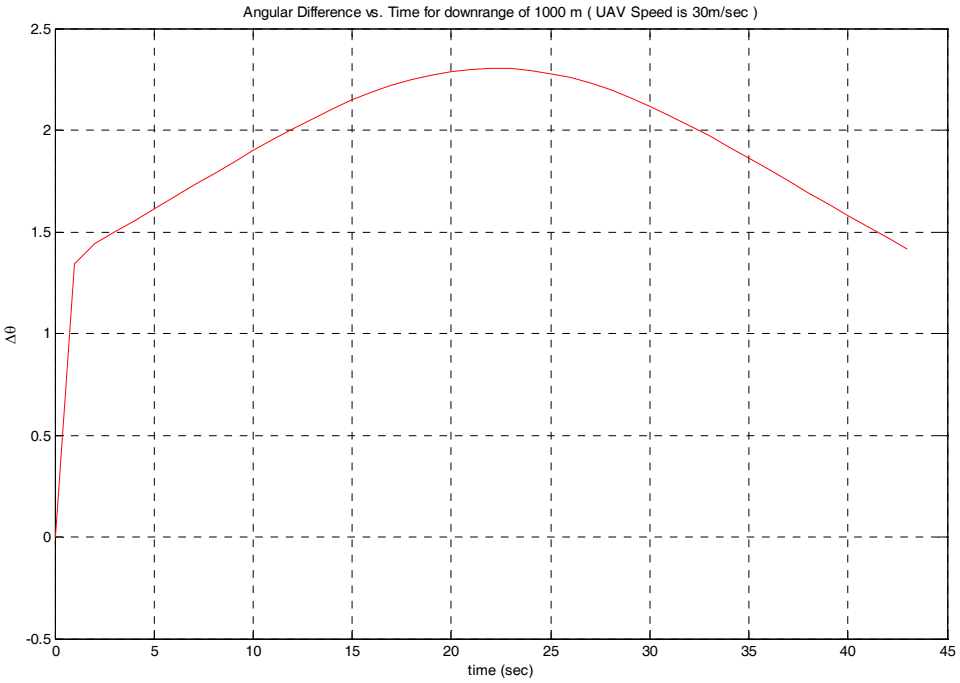

Figure 18 Angular difference (tracking error) vs. time for a UAV 1000 m downrange at a speed of 30 m/sec.

When the MATLAB code is examined, it can be seen that the time increment for the system to follow the target is one second. When the time increment is reduced to one-tenth of a second, the angular error gets much smaller, i.e. for UAV speed equal to 30

m/sec, the maximum angular error becomes 0.23 degrees. This makes sense because as the update rate is increased, the tracking system will refresh its scan angle more frequently.

With the help of Figure 16, the HPBW has been found to be approximately 16 degrees. On the other hand, Figure 19 shows that it is actually around 13 degrees. This difference arises from the approximations made in obtaining Eq. (15), an equation to calculate HPBW. The difference encountered is expected for small arrays. [15]

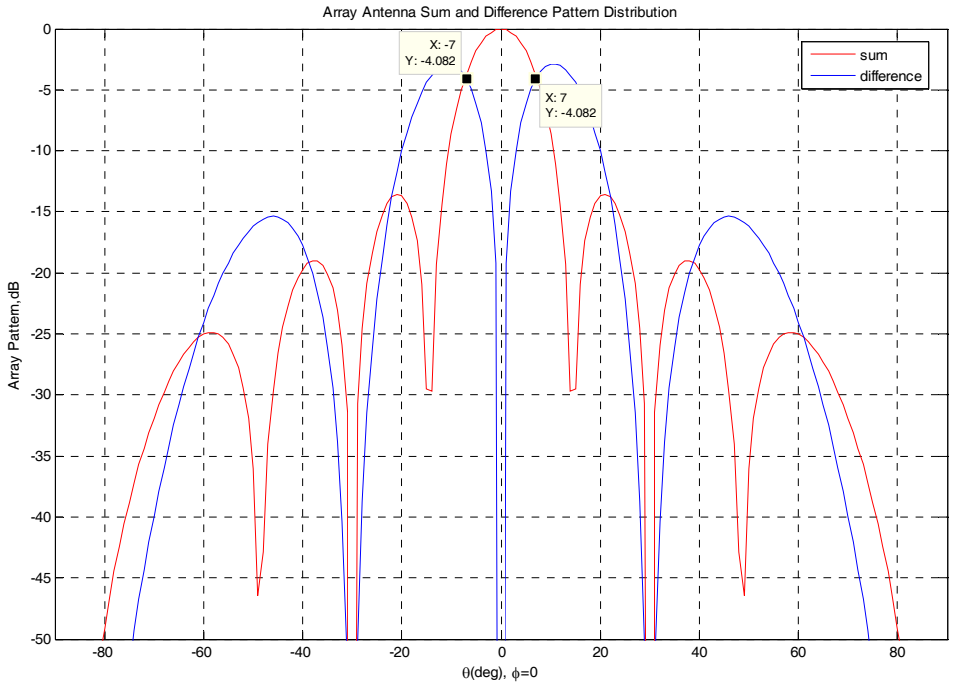

Figure 19 Array antenna sum and difference pattern distribution.

Gain is another concern for tracking a target. If the angular position of the target is squinted with respect to the peak of the main beam, a loss in gain called *crossover loss* occurs. Crossover loss is calculated as follows for a Gaussian beam: [12]

$$G(\Delta\theta) = G_o e^{-K(\Delta\theta)^2/(\theta_B)^2} \tag{16}$$

$$L_{co} = 10\log\left(\frac{G(\Delta\theta)}{G_o}\right) \tag{17}$$

where G_o is the gain of the beam peak, $\Delta\theta$ is the angular difference between the beam and the position of the target with respect to the antenna boresight, θ_B is HPBW, $K = 4\ln(2) = 2.773$, and L_{co} is the crossover loss in dB.

The SNR is obtained from the Friis equation:

$$SNR = \frac{P_r}{N} = \frac{P_t G_t G_r \lambda^2 pq}{(4\pi R)^2 L_s} \frac{1}{k_B T_s B} \tag{18}$$

where P_r is the received power, N is the noise generated in the system, P_t is the transmitter power on the UAV, G_t and G_r are the antenna gains of the transmitting and receiving antennas, respectively, λ is the wavelength, R is the range, L_s is the system loss, p is the polarization efficiency (or polarization mismatch factor) and q is the input mismatch factor, k_B is Boltzman's constant, T_s the temperature of the system and B is the bandwidth of the receiver.

Equation (18) reveals the fact that SNR is proportional to gain, meaning that the smaller the gain, the smaller the SNR. As seen in the equation, the reduction in gain also causes loss in receiver power. If the system does not have sufficient receiver power, it cannot have the necessary bit rate to maintain the data link and it suffers loss of information. If range is computed based on a given SNR:

$$R_{\max}^2 = \frac{P_t G_t G_r \lambda^2 pq}{(4\pi)^2 (SNR) L_s} \frac{1}{k_B T_o B} \tag{19}$$

It is seen that range of the tracking system is dependent on gain as well. Losses in gain reduce the range of the system and cause loss of track.

The noise level changes with receiver hardware. A more appropriate quantity that is independent of the receiver noise is the received power, P_r. In order to examine the range performance of our tracking system, a MATLAB program, *Friis Equation.m*, based on Eq. (18) and (19) was written. It is assumed that our system does not have any polari-

zation or feed mismatch losses. Moreover, the sensitivities according to bit rates of Cisco Aironet 350 cards are used in the program. The bit rates and sensitivities are summarized in Table 2. [15] The P_t is entered as 1 Watt and G_t is 1. The G_r is 12 dB and the increase in receiver gain due to ground plane element factor effects is neglected.

The results of the MATLAB program are shown in Table 2. The higher the bit rate, the less range we will have. These bit rates can be determined in accordance with the operation type. The results seen in Table 2 are overly optimistic, because the calculation does not take the losses into account. The FCC limits the Effective Radiated Power (ERP) ($= P_t G_t$) to 4 Watts. If the ERP of the transmitter antenna on the UAV is increased to 4 Watts, the range increases to double the range values seen in Table 2.

Bit Rate	**Minimum Sensitivity Level**	**Range**
1 Mbps	-94 dBm	62.76 km
2 Mbps	-91 dBm	44.43 km
5.5 Mbps	-89 dBm	35.29 km
11 Mbps	-85 dBm	22.27 km

Table 2 Bit Rates and minimum sensitivity level equivalents vs. range for an ERP of 1 W. (After [16].)

Using the antenna parameters of Figure 18 and taking $\Delta\theta$ as 2.305 degrees (because it is the maximum angular error), the maximum crossover loss of the system is calculated at approximately -0.25 dB. Figure 15 has shown that an 8-element system needs a gain of more than 12 dB. A loss of 0.25 dB in gain does not cause a big decrease in SNR of the system.

If the UAV travels the path in 22 seconds at speed of 60 m/sec (as opposed to 30 m/sec), the maximum tracking error is 4.323 degrees, as seen in Figure 20. Even though this angular error is not within the approximated limits of the MATLAB code, it is still within the limits of the system design, as seen in Figure 18. Consequently, the system does not lose the track with a UAV at the speed of 60 m/sec.

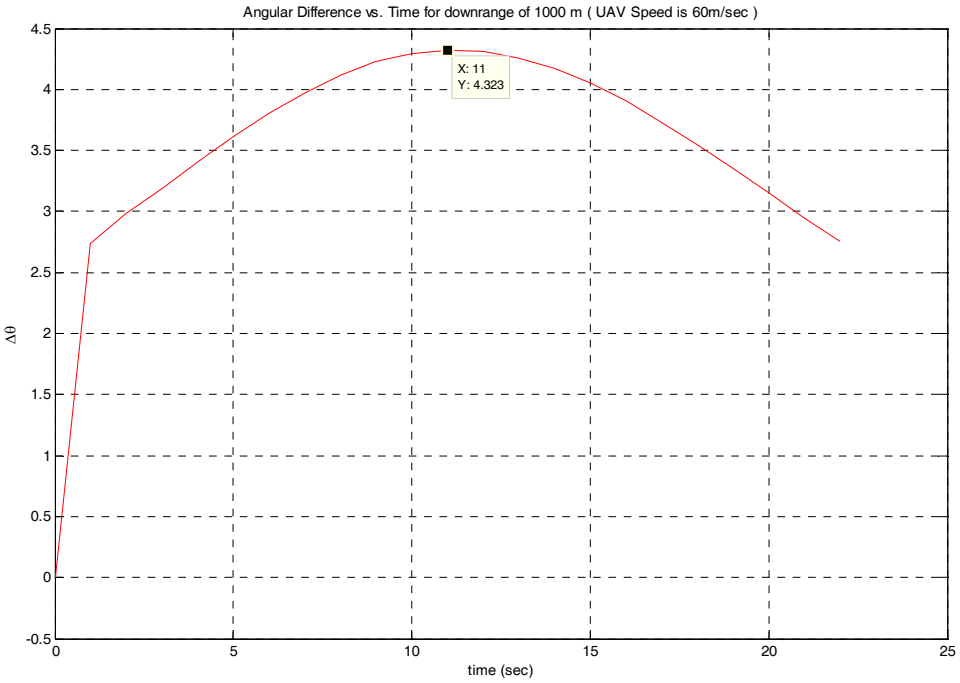

Figure 20 Angular difference (Tracking Error) vs. time for a UAV 1000 m at a speed of 60 m/sec.

Crossover loss is calculated from Eq. (16) and (17) as 0.879 dB. Again, this loss is much less than the required gain of the tracking antenna, so much less so that it can be ignored. This result also shows that the system does not lose the track.

As far as the maximum speed is concerned, the maximum angular error for a UAV with the speed of 90 m/sec is 5.943 degrees, as seen in Figure 21. Crossover loss is calculated as 1.66 dB. These parameters are still within the acceptable limits. As a result, the system does not lose the track of a UAV flying with maximum speed at 1 km and can maintain the data link between the UAV and the tracking system.

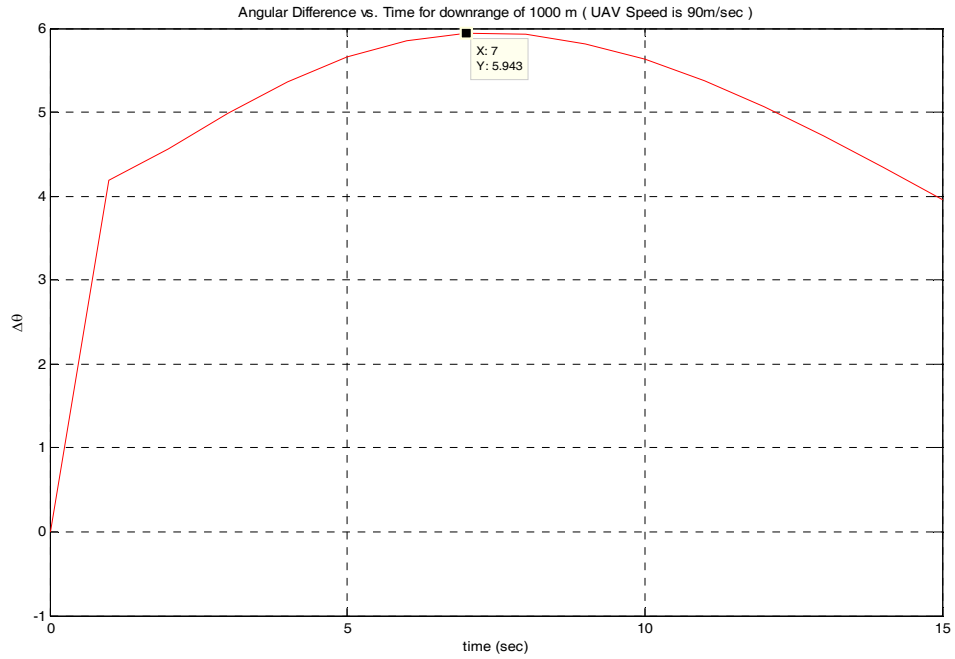

Figure 21 Angular difference (Tracking Error) vs. time for a UAV downrange 1000 m at a UAV speed of 90 m/sec.

B. POLARIZATION MISMATCH

One important consideration of the antennas that needs to be taken into account is the *polarization*. Polarization affects the link performance. The antenna polarization determines the direction of the electric field. *Elliptical polarization* is the most general polarization, with *linear* and *circular polarizations* being special cases of elliptical polarization. In the case of linear polarization (LP), when the electric field component of the radiated wave oscillates in a direction perpendicular to the earth's surface, the radiation is said to be *vertically polarized*. If the electric field component of the radiated wave oscillates in a plane parallel to the earth's surface, then the radiation is said to be *horizontally polarized*.

The tracking system is receive only so the polarization of the antenna in the tracking system should match the polarization of the antenna on the UAV. For transmitting and receiving to be matched, they both need to have the same type of polarization, or a mismatch loss arises, which is accounted for by p in the Friis equation, Eq. (18). The impedance mismatch factor q is between 0 and 1. The impedance of both antennas are as-

sumed to be well matched for the feed lines, i.e. $q = 1$. The polarization efficiency varies from 0 to 1 as well; a complete match ($p = 1$) occurs when the incoming wave and the receiving antenna are identical polarization and aligned. When the incoming wave and the antenna are *cross polarized* ($p = 0$), a complete mismatch occurs; i.e. orthogonal linear states (horizontal and vertical polarizations).

The polarization efficiency is the product of the incident wave electric field $\vec{E}^i$ and vector effective length of the receiving antenna $\vec{h}$. The dot product of these two quantities gives the antenna output voltage in volts. When the antenna is matched to the incident field, the maximum voltage is obtained. The polarization efficiency can be obtained as: [15]

$$p = \frac{\left|\vec{E}^i \cdot \vec{h}^*\right|^2}{\left|\vec{E}^i\right|^2 \left|\vec{h}\right|^2} = \left|\hat{e}^i \cdot \hat{h}^*\right|^2 \tag{20}$$

where $\hat{e}^i$ and $\hat{h}$ are the complex unit vectors for the incident wave and antenna effective length. Since the circular and linear polarizations are the special cases of elliptical polarization, these vectors can be written as: [15]

$$\hat{e}^i = \cos\gamma_i \hat{x} + \sin\gamma_i e^{j\delta_i} \hat{y} \tag{21-a}$$

$$\hat{h} = \cos\gamma \hat{x} + \sin\gamma e^{j\delta} \hat{y} \tag{21-b}$$

where γ_i, δ_i and γ, δ are the polarization parameters that will define whether the elliptical polarization becomes linear or circular. The details for calculation of these parameters are explained well in [15].

There are three combinations of the polarization types of the receiving and transmitting antenna. The first case is where a linearly polarized antenna receives a linearly polarized wave. The dipole in Figure 22 is tilted at an angle τ and dipole represents a linearly polarized antenna. The wave arrives normal to the *x-y* plane of the dipole an-

tenna. The angles γ and γ_i are equal to τ and τ_i, respectively. When these are substituted in Eq. (21), Eq. (20) becomes: [15]

$$\begin{aligned} p &= \left|\hat{e}^i \cdot \hat{h}^*\right|^2 = \left|(\cos\tau_i \hat{x} + \sin\tau_i \hat{y}) \cdot (\cos\tau \hat{x} + \sin\tau \hat{y})\right|^2 \\ &= \left|\cos\tau_i \cos\tau + \sin\tau_i \sin\tau\right|^2 = \cos^2(\tau_i - \tau) \\ &= \cos^2\delta \end{aligned} \tag{22}$$

It is seen from Eq. (22) that the polarization efficiency is a factor of the relative tilt angle and varies from 0 to 1. As the UAV moves, this angle will change so the polarization efficiency will change as well. This could cause an unacceptable loss in received signal at the array.

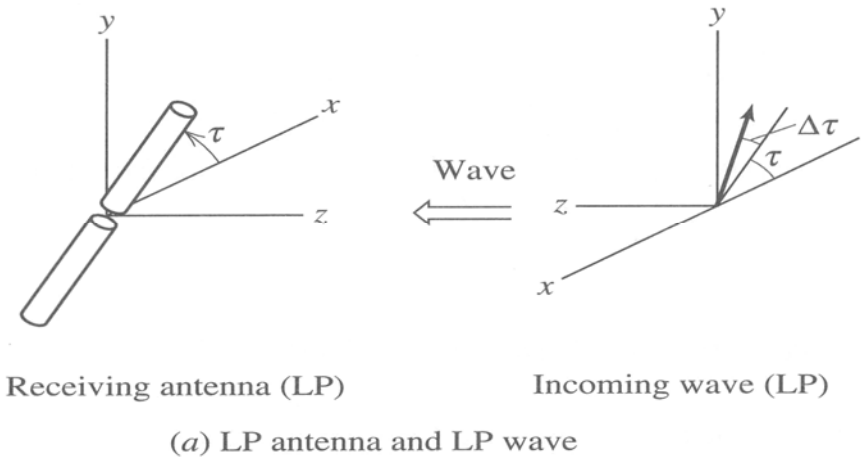

Figure 22 Illustration of reception of a linearly polarized incident wave by a linearly polarized receiving antenna. (After [15].)

Because the elements in the tracking array are linearly polarized. The polarization of the antenna on the UAV could be made circular. When a circularly polarized (CP) wave is received by a linearly polarized antenna, the polarization loss is: [15]

$$p = \left|\hat{e}^i \cdot \hat{h}^*\right|^2 = \left|\frac{1}{\sqrt{2}}(\hat{x} - j\hat{y}) \cdot (\cos\tau \hat{x} + \sin\tau \hat{y})^*\right|^2 = \frac{1}{2}\left|\cos\tau + j\sin\tau\right|^2 = \frac{1}{2} \tag{23}$$

Therefore, the polarization efficiency is 0.5 and constant. Half the power from the circularly polarized wave is lost when received by the linearly polarized antenna in our system. This loss is equal to 3 dB and is significant, reducing the operational range of the UAV. It is the price paid to avoid complete loss of signal due to polarization mismatch.

The third case is where both the incident wave and receiving antenna are circularly polarized. Even though the antenna is currently linearly polarized, the dipoles can replaced by CP elements. If both of the antennas are assumed to be right-hand circularly polarized, Eq. (20) would take the form of: [15]

$$p = \left|\hat{e}^i \cdot \hat{h}^*\right|^2 = \left|\frac{1}{\sqrt{2}}(\hat{x} - j\hat{y}) \cdot \frac{1}{\sqrt{2}}(\hat{x} - j\hat{y})^*\right|^2 = 1 \tag{24}$$

As a result, the antennas are seen to be perfectly matched. If one of the antennas were left-hand circularly polarized, then they would be cross polarized and polarization efficiency equal to 0. In light of these findings, it can be said that both of the antennas should preferably be circularly polarized for the best performance of the system.

C. CST MICROWAVE STUDIO SIMULATION RESULTS

CST Microwave Studio is a software package for electromagnetic analysis and design in the high frequency range. The Finite Integration Technique (FIT), a time-domain numerical method based on the integral form of Maxwell`s equations is used in CST Microwave Studio. The parameters of the device that is modeled can be defined in detail in three dimensions. The program is especially suited to the fast efficient analysis and design of components like antennas, filters, transmission lines, couplers, connectors, printed circuit boards, resonators, etc. [17, 18]

Before building a ground plane, it is desired to see how the ground plane is going to affect the performance of the system. Because, the array consists of printed circuit dipoles behind the ground plane, the radiation pattern of the array needs to be computed via a simulation. CST Microwave Studio is the program that will give us accurate patterns of the array with a ground plane. Mutual coupling and ground plane edge diffraction are included in the FIT solution.

The model shown in Figure 23 is a modification of an existing model as a part of some previous research. The coordinate system has the ground plane in the *x*-*z* plane and the normal is the *y* axis. The dimensions were already determined as shown in Figure 14. The ground plane is selected to be copper, a good conductor.

After the sides of the ground plane are cut, the locations of the dipole boards are inserted in slots at the element spacing as shown in Figure 24. The extent of the ground plane length at the sides, top and bottom are required to be at least ½ wavelength. The lengths for the ground plane are approximately 0.65 and 0.80 wavelengths respectively.

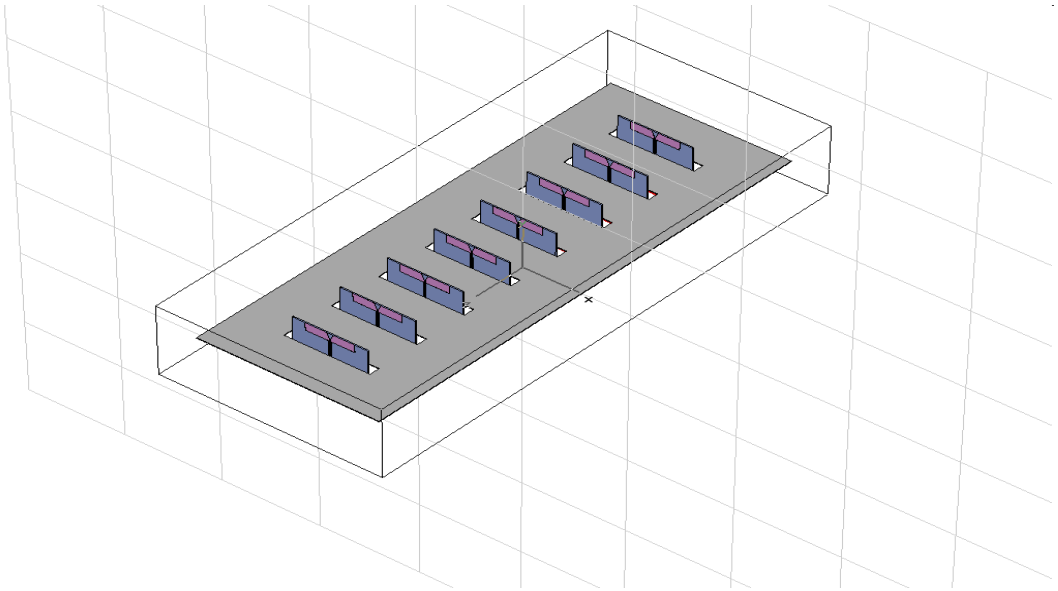

Figure 23 The top view of the ground plane and an array of dipoles modeled in CST Microwave Studio. [19]

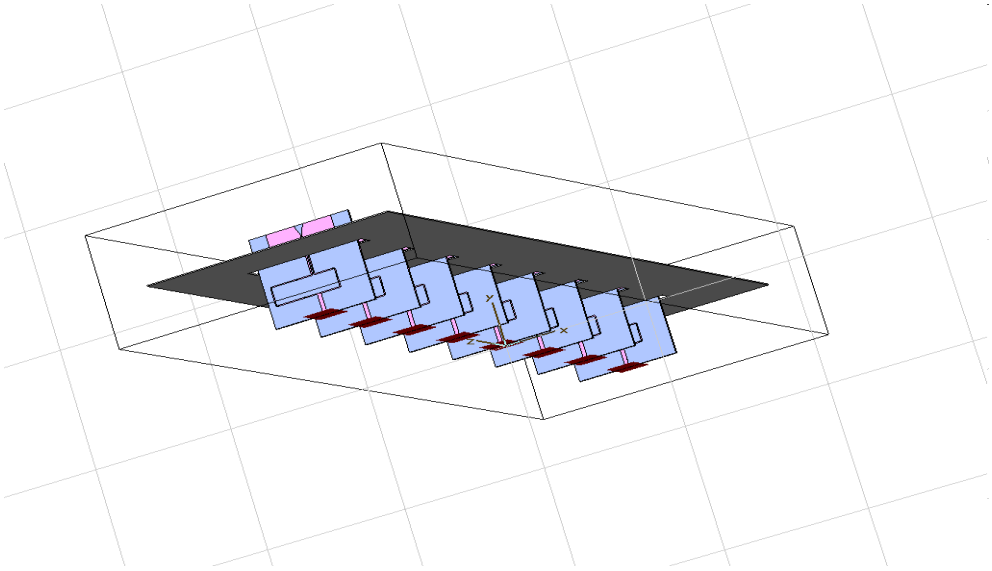

Figure 24 The bottom view of the ground plane and an array of dipoles modeled in CST Microwave Studio. [19]

The simulation is run to obtain the sum and difference patterns of the array of dipoles with and without scanning in the H-plane of the array. The E-plane of the array and polar plots of sum and difference patterns can be seen in Appendix E. The sum pattern of the array of dipoles without scan and with scan are seen in Figures 25 and 26. The gain of the main lobe is computed as 16.6 dB and HPBW as 12.1 degrees. It can also be seen in the sum pattern polar plot in Appendix E. The gain is found to be 3.6 dB more and HPBW is 3.9 degrees less than expected. These differences can be attributed to the ground plane effect. The ground plane increases the gain about 3 dB as mentioned before and decreases the HPBW. The sidelobes are about -13 dB and there is almost no back lobe.

The difference patterns with and without scan angle are seen in Figure 27 and 28. The gain of the main lobe is computed as 13.9 dB and HPBW as 11 degrees as it can be seen in the difference pattern polar plot in Appendix E. The sidelobes are about -9.5 dB and there is almost no back lobe. The main lobe of the sum pattern can also be called the directivity of the array.

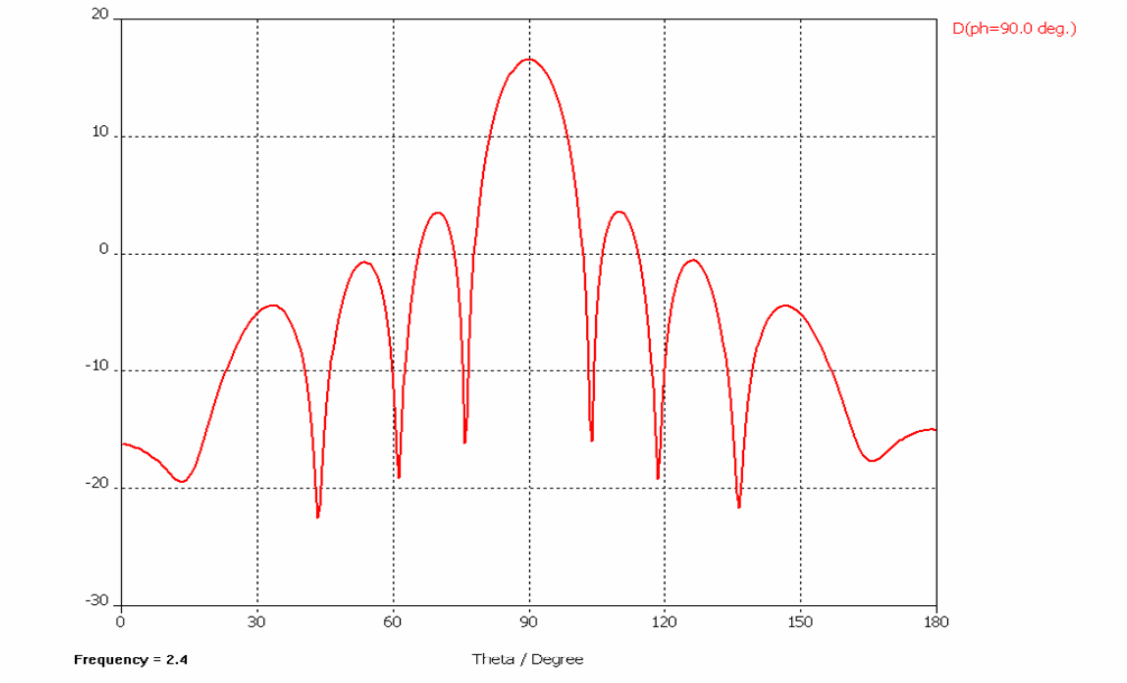

Figure 25 The sum pattern of the array of dipoles with ground plane modeled in CST Microwave Studio (broadside). [19]

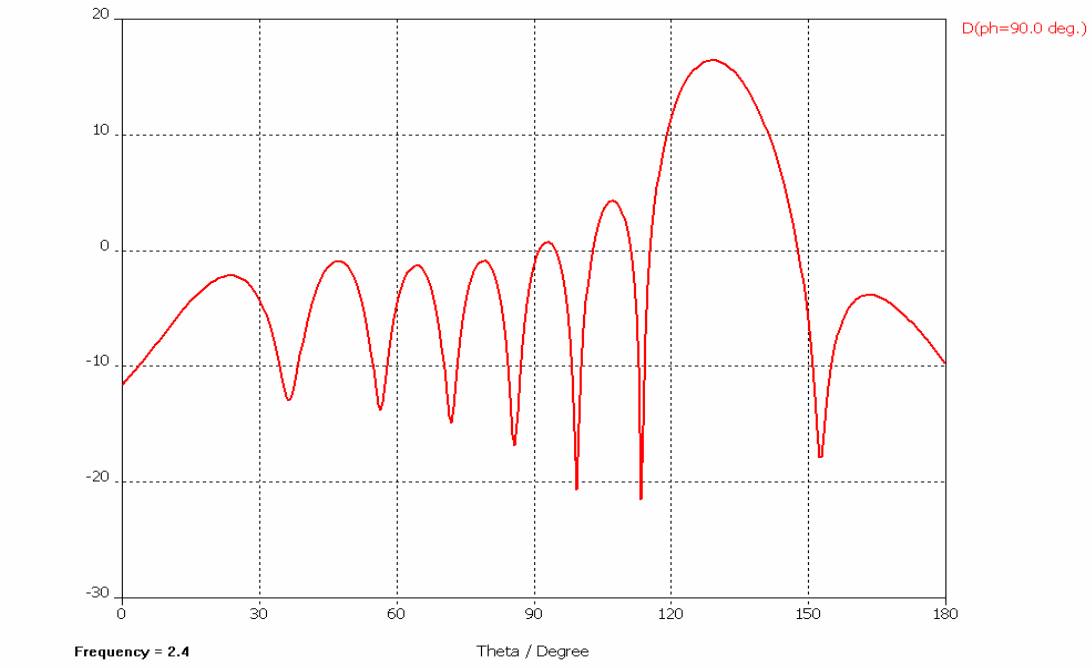

Figure 26 The scanned sum pattern of the array of dipoles with ground plane modeled in CST Microwave Studio, scanned 40° from broadside. [19]

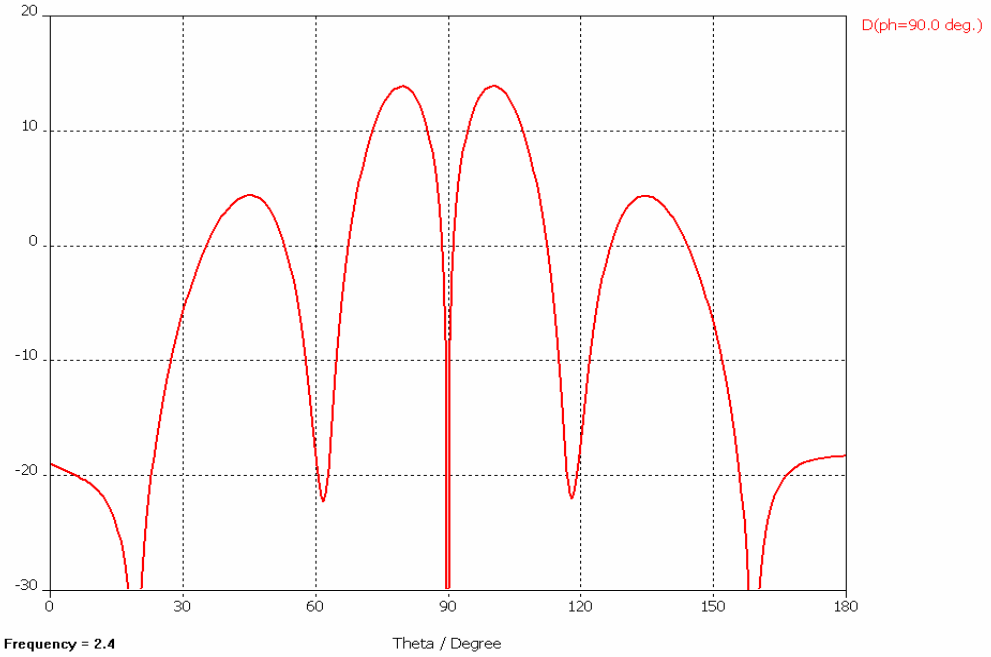

Figure 27 The difference pattern of the array of dipoles with ground plane modeled in CST Microwave Studio (broadside). [19]

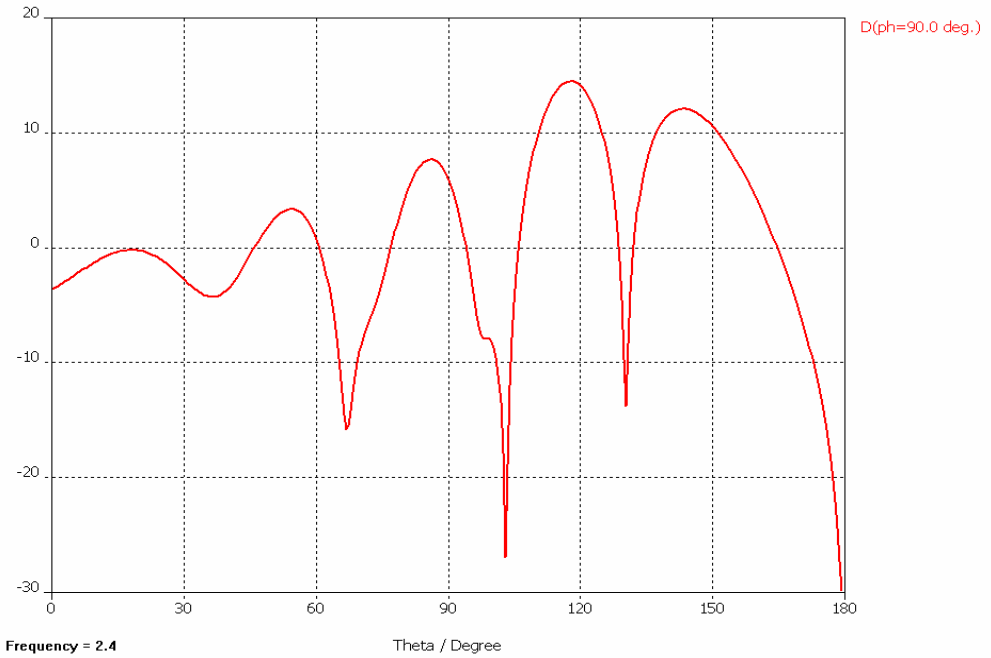

Figure 28 The scanned difference pattern of the array of dipoles with ground plane modeled in CST Microwave Studio, scanned 40° from broadside. [19]

This chapter covered the tracking antenna design. It was mentioned in Section A how the necessary parameters for the design were determined and what requirements were. The tracking error results of some MATLAB programs were shown. In Section B, other important considerations such as SNR, and polarization mismatch, were discussed. Lastly, the ground plane effect on the array pattern was examined via a simulation using CST Microwave Studio in Section C.

IV. TRACKING ARRAY HARDWARE

This chapter discusses the tracking array assembly and test. Section A gives descriptions of the test set-up and array components. Section B addresses the procedure and results of characterizing the system components. Section C covers the array assembly. Section D gives a brief introduction of the controller software (LabVIEW). LabVIEW data flow is mentioned in Section E. How the components of the system were built up as a system is in Section F. Section G analyses the final simulation results.

A. DESCRIPTION OF THE COMPONENTS

A block diagram of the eight element array is seen in Figure 29. The design is similar to the receiver part of a radar. One of the biggest advantages of our array is that it exploits COTS hardware to reduce the cost. The array consists of eight dipoles that were actually designed for a previous research project [3]. A Low Noise Amplifier (LNA) is connected to each of the dipoles and the signal is sent to the AD-8347 EVAL demodulators for the demodulation process of the signal. The demodulators are fed by a local oscillator (LO) signal via 4-way and 2-way splitters (they are not shown in Figure 29) to obtain the baseband voltage. The demodulated analog baseband signal is digitized by an analog input module (cRIO-9215) made by National Instruments (NI). The modules are set in an 8 slot chassis with an embedded controller. There are four digitized differential voltage components (I^-, I^+, Q^-, Q^+). Two power supplies provide the power to the components of the system.

The cRIO-9215 modules run with software called LabVIEW. LabVIEW will be discussed in detail in the Section D of this chapter. LabVIEW can be run either on a PC/ Laptop or an embedded controller designed by National Instruments that has the same architecture as a computer. The LabVIEW program incorporates MATLAB software to accomplish the tracking signal calculation and provide the phase data to scan the beam. The tracking error signal is also computed by the controller.

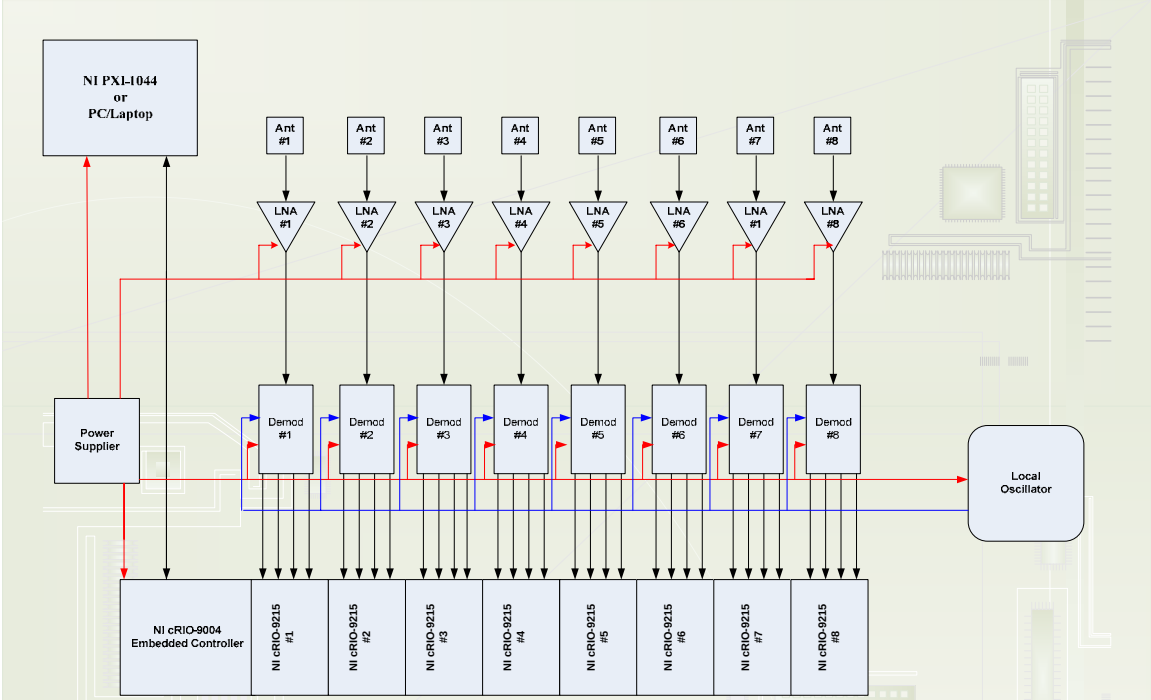

Figure 29 Block diagram of the array.

1. Dipoles

The dipoles (shown in Figure 30) were designed in CST Microwave Studio by Professor David C. Jenn and fabricated by Cirexx Corporation. They operate at 2.4 GHz. The return loss of the dipoles was measured and found to be at least 15 dB. Reference [3] discusses the dipole element return losses more in detail.

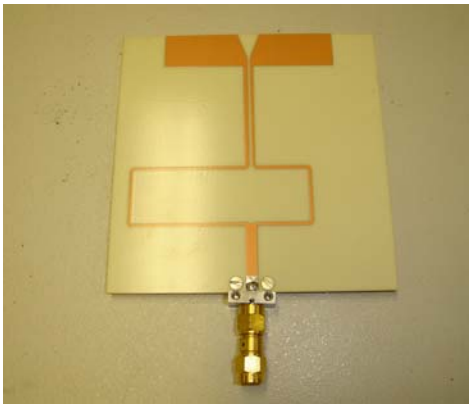

Figure 30 One of the printed circuit dipoles used in the array.

2. Low Noise Amplifier (LNA)

The LNA amplifies the weak signals captured by the dipoles. The LNA has a low noise figure (1.7 dB) and high gain (23 dB), which improves the performance the array. Because the overall noise figure is dominated by the first few stages, the total noise of the cascaded stages is reduced by the LNA. Hence, the fact that the LNA has a very low noise figure is a key factor to signal detection.

The LNA must be located very close to the dipole in order to prevent the losses in the feedline. For our setup, the LNAs are connected to the dipoles with a barrel to minimize the cable loss.

Cost is always a factor in building an array system. The LNA-2700 by RF Bay Inc. (shown in Figure 31) was selected as the LNA because of its reasonable price as well as its low noise figure. The LNA-2700 is a wideband LNA that operates with a frequency range from 2.2 GHz to 3.2 GHz. A 12 V DC power supply is required to run the LNA. The spec-sheet of LNA-2700 can be found in [20].

Figure 31 LNA-2700 by RF Bay, Inc.

3. Demodulator

The demodulator recovers the information from the carrier wave of an analog signal. The demodulator that is selected for this design is a quadrature demodulator. A quadrature demodulator phase shifts a portion of the LO signal by 90 degrees and multiplies it with the received signal in a mixer of the receiver. The general diagram of a quadrature demodulator is shown in Figure 32.

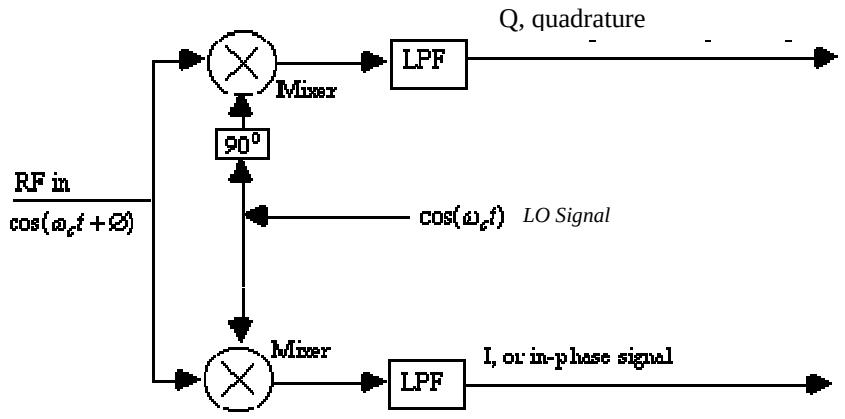

Figure 32 Quadrature demodulator recovers both the in-phase and quadrature phase components of the input signal. [21]

The demodulator selected for the array is the AD8347 EVAL Quadrature Demodulator manufactured by Analog Devices. Figure 33 shows one of these demodulators used in the system. This COTS demodulator operates within the frequency range 0.8 through 2.7 GHz. This demodulator can be supplied with voltages between 2.7 and 5.5 V. The voltage VGIN determines the amplification of the received signal. VGIN can range from 0.2 to 1.2 V.

On the demodulator board, the RF input signal goes through two stages of variable gain amplifiers of the AD 8347 prior to two mixers. The LO quadrature phase splitter employs polyphase filters to achieve high quadrature accuracy and amplitude balance over the entire operating frequency range. Separate *I* and *Q* channel variable gain amplifiers follow the baseband outputs of the mixers. Then, the *I* and *Q* baseband components of the received signal are amplified again by baseband amplifiers.

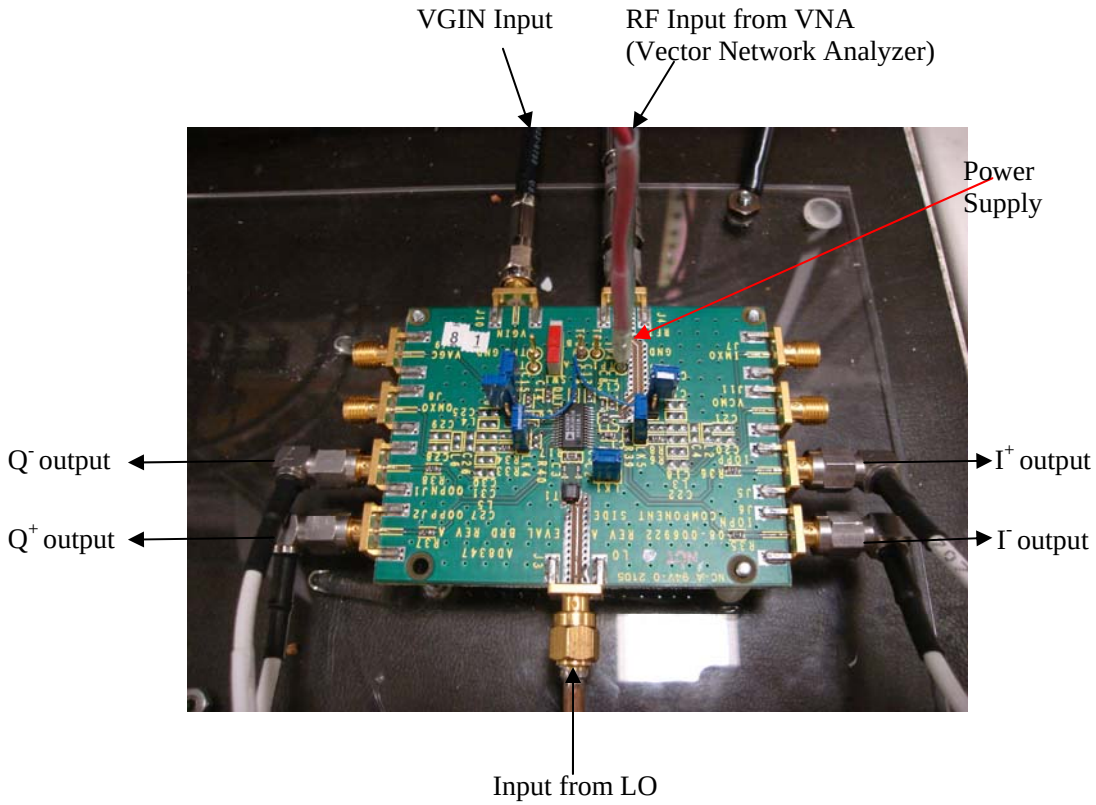

Figure 33 AD 8347 Quadrature demodulator by Analog Devices.

The AD8347 demodulator has a Voltage Gain Amplifier (VGA) which gives control of the gain automatically. For our application the VGA is not used. The VGA gain will be set from an external source, hence VDT1 and VDT2 (the on-board detector inputs) are not used, and tied to VREF with the blue wires as seen in Figure 32. Reference [22] includes a very detailed specsheet of AD8347 EVAL Quadrature Demodulator with more information.

4. Local Oscillator

The local oscillator (LO) is designed and manufactured by Z-Communications and is shown in Figure 34. The LO signal at 2.4 GHz is generated by a V800ME10 oscillator on the board and fed into the demodulators. There are two types of voltages that need to be supplied to the V800ME10. They are power up and tuning voltages. The tuning voltage is routed through a 1 kΩ adjustable pot for fine-tuning of the LO frequency.

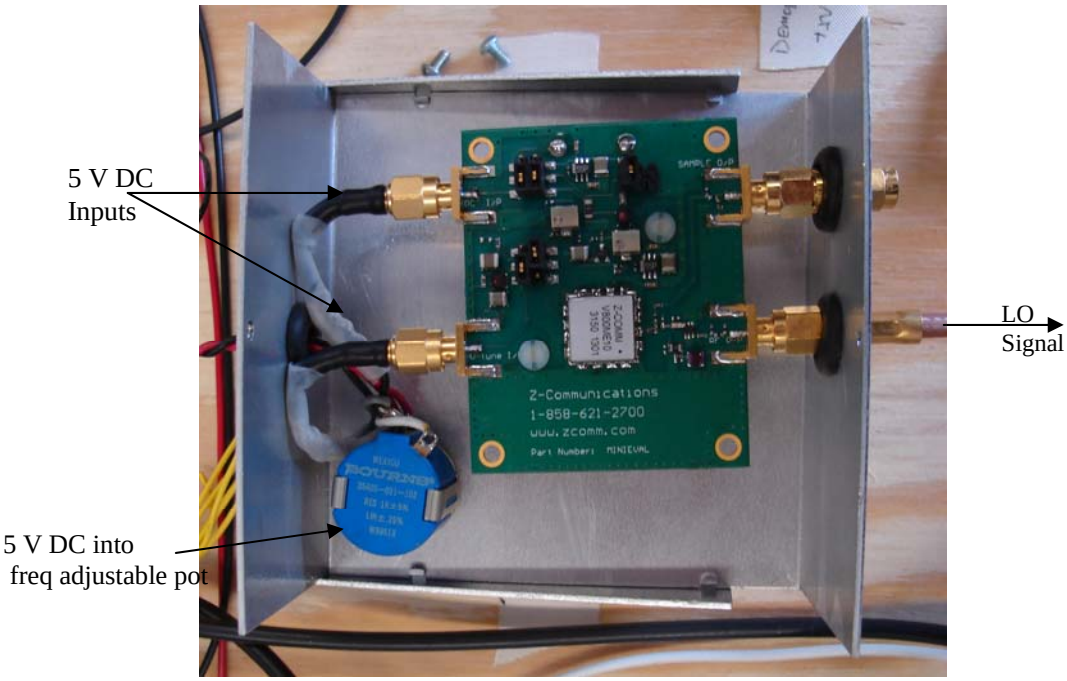

Figure 34 LO Configuration.

5. Power Supplies and Power Adjustment Circuit.

There are two linear power supplies used for the array which are HP 6255 A by Hewlett Packard. The power supplies will be replaced by Condor HCC512-A+ linear power supplies to be tested in anechoic chamber. The power supplies provide +5 and +12 V. The +12 V is applied to VGIN of the demodulator after being adjusted with a VGIN voltage regulator designed by Bob Broadston from NPS. The adjustor reduces VGIN to 0.38 V, which is the voltage selected for the demodulators. The LO and LNAs are provided with +12 V by the power supply which has maximum currents of 6.00 A, 2.50 A for the voltages of 5 V and 12 V, respectively.

6. Signal Processing Devices

National Instruments (NI) manufactures many Input and Output (I/O) modules to interface with or acquire real-world data, analyze that data, and to extract information and present the information to an end user. The I/O modules contain built-in signal conditioning and connectors for direct connection to sensors or actuators.

The I/O modules are set in a special reconfigurable expansion chassis with a controller device which is basically a highly reliable embedded real-time processor designed to achieve intelligent operation. The reconfigurable chassis is the heart of the NI Compact Reconfigurable I/O (cRIO) system and contains the NI RIO Field Programmable Gate Array (FPGA). The RIO core is powered by a user-programmable FPGA configured by a special software designed by NI, LabVIEW, that serves as a high-speed interface to the I/O modules. LabVIEW FPGA Module is used to program the FPGA on the cRIO reconfigurable chassis. FPGAs are silicon chips with unconnected logic gates. The flexible design of FPGA enables us to target any device compatible with NI cRIO and to customize our hardware functions for our system. It is possible to execute multiple tasks simultaneously using the LabVIEW FPGA module. Collectively all of the components mentioned above are known as a Data Acquisition (DAQ) system. [23]

NI provides different I/O modules for different purposes. The four analog output signals from the demodulator are input to an analog input (A/I) module to be sampled and converted into digital signals for signal processing and analysis. The A/I module selected for this purpose is the NI cRIO-9215. The NI cRIO-9215, shown in Figure 35, provides 4 simultaneously sampled analog inputs with a rate of 100 kS and a resolution of 16 bits. The NI-9215 contains traceable calibration, a channel-to-earth ground, double isolation barrier for safety and noise immunity, and a high common voltage range. [23]

Figure 35 NI cRIO-9215 Analog Input Module. [24]

The NI cRIO-9215 analog input modules are connected directly to the FPGA hardware. This FPGA hardware is the reconfigurable chassis NI cRIO-9104 with the real-

time embedded controller cRIO-9004 as shown in Figure 36. The cRIO-9104 chassis has 8 slots and a RIO FPGA core with a RAM of 196 kB. The FPGA core has an individual connection to each NI cRIO-9215 analog input module and can read information from each module. The module operation is precisely synchronized with 25 ns resolution. The FPGA circuitry in the cRIO-9104 chassis passes the data to the real-time embedded controller cRIO-9004 through a local PCI bus. The cRIO-9004 includes 64 MB of DRAM memory and 512 MB of nonvolatile flash storage for data-logging applications. Embedded software code processes the data from the I/O modules and transfers the data to the host program run on a desktop PC or laptop. This FPGA program is synchronized with the host program by the means of FPGA-generated interrupt request (IRQ) or an internal millisecond real-time clock source. [23]

In addition to programmatic communication via TCP/IP, the cRIO controllers also include built-in servers for VISA, HTTP, and FTP. The VISA server provides remote download and communication access to the RIO FPGA that is configured for our system over Ethernet.

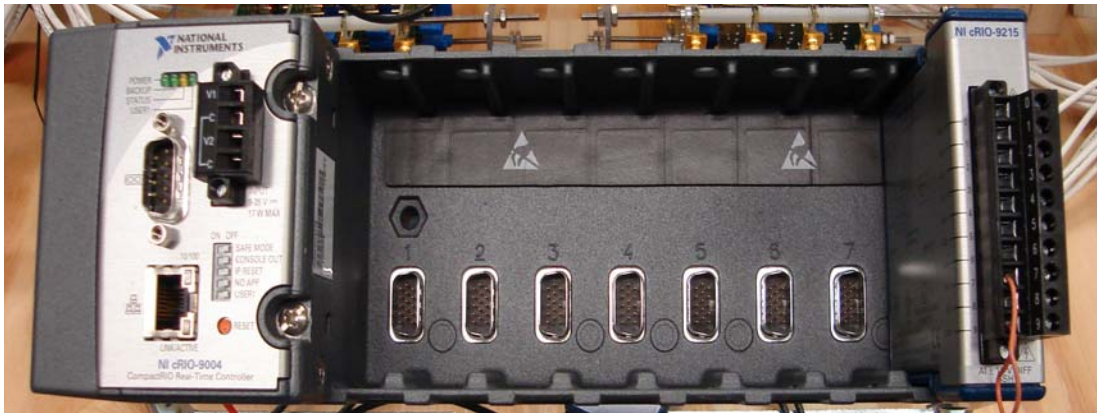

Figure 36 The reconfigurable chassis NI cRIO-9104 with the real-time embedded controller, cRIO-9004 and analog input module, NI cRIO-9215.

B. CHARACTERIZING THE COMPONENTS OF THE SYSTEM

Although all the manufactured system components generally perform the same, there are slight differences that must be determined and the variations compensated for in the signal processing. Using the VNA, the demodulators, 4-way splitters and 2-way splitter are characterized before installing them in the system. Integration of the LNA in the system and the inter-element phase differences will be discussed later.

Before building up the array, a test setup was designed to test and characterize the demodulators. The setup in Figure 37 was established for this purpose. The VNA is a very sensitive device that can measure the magnitude and phase characteritics of networks and components such as filters, amplifiers, attenuators, demodulators, modulators and antennas. Two kinds of measurements can be made with VNA: reflection measurements and transmission measurements. An incident signal is generated by an RF source controlled by the HP 8510, then applied to the test network and compared with the signal reflected from the test network input or transmitted through it. The deviation from linear phase is one of the transmission measurements that can be made with VNA.

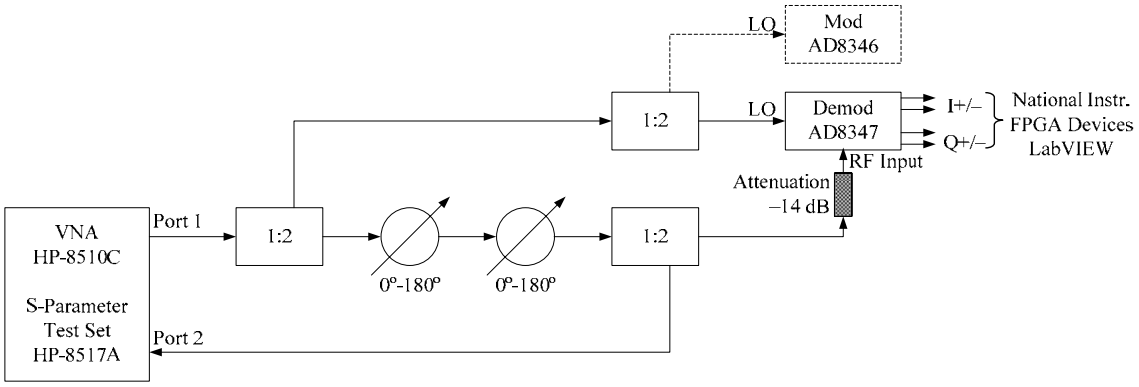

Figure 37 The demodulator setup. [25]

An S-parameter test set is integrated into VNA. The scattering parameter of a port is measured with all other ports terminated with a 50 Ω load. S_{11} is the input reflection coefficient, S_{22} is the output reflection coefficient, S_{21} is the forward transmission (insertion) gain and S_{12} is the reverse transmission (insertion) gain. Since the input is port 1, the VNA measures the forward transmission, S_{21}. [26]

The VNA generates the reference signal at 2.4 GHz and it serves as RF signal to the test setup and the LO signal to the modulator (AD8346) and demodulator (AD8347) after a 2-way splitter. The modulator is not used for this particular measurement. The RF signal goes through two phase shifters so the signal phase can be shifted 360 degrees manually. The RF signal passes through a 2-way splitter again and one arm feeds the demodulator whereas the other arm is fed back into the S-parameter set. A setting of 6 dBm of input power from the VNA (default value) is applied for the RF and LO signals. According to Analog Devices, the RF input power must be between -2 and -30 dBm and the LO input power must be between -10 and 0 dBm. In order to keep the demodulator from having more power than that the maximum limit, a 14 dB attenuator is inserted at the RF input of the demodulator. The LO signal power was -14.4 dBm and the RF signal power -14 dBm right after Port 1. RF signal power was measured at -26.15 dBm and the LO signal power was measured at -14.4 dBm right before the signals enter the demodulator. The 20 dB loss for the LO and 12.15 dB loss for the RF signals can be attributed to the splitters, phase shifters, attenuators and cables. Note that every component added to the system (such as attenuators, cables, and connectors) contributes to a change in phase and rotation of the *I*-*Q* circle that is obtained from the demodulator voltage.

The received signal with the carrier wave at ω_c or $2\pi f_c$ is converted to a baseband signal by the demodulator:

$$s(t) = A(t)\cos(\omega_c t + \Phi(t)) = I(t)\cos(\omega_c t) - Q(t)\sin(\omega_c t) \tag{25}$$

where ω_c is the carrier frequency of $s(t)$ in radians. The baseband signal is composed of two components:

$$\begin{aligned} I(t) &= A(t)\cos(\Phi(t)) \\ Q(t) &= A(t)\sin(\Phi(t)) \end{aligned} \tag{26}$$

where $A(t)$ is the amplitude of the signal, $s(t)$, and $\Phi(t)$ is the phase of $s(t)$. These in-phase (I) and quadrature-phase (Q) components are used to obtain the amplitude and phase of the received signal:

$$A(t) = \sqrt{I(t)^2 + Q(t)^2} \tag{27}$$

$$\Phi(t) = \tan^{-1}\left(\frac{Q(t)}{I(t)}\right) \tag{28}$$

The AD8347EVAL demodulator down-converts the RF signal to *I* and *Q* baseband components after mixing with the LO signal. *I* and *Q* voltages are measured at the in-phase output positive (IOPP), in-phase output negative (IOPN), quadrature-phase output positive (QOPP) and quadrature output negative (QOPN) as shown in Figure 38 and calculated with Eq. (29):

$$\begin{aligned} I &= I^{+} - I^{-} \\ Q &= Q^{+} - Q^{-} \end{aligned} \tag{29}$$

Using LabVIEW, the measurement results of the differential baseband components of the analog input signal in the demodulator (IOPP, IOPN, QOPP, QOPN) are directly output as amplitude and phase. This program was later modified to make it compatible with 8 elements.

VGIN varies between 0.2 and 1.2 V, and it determines the amplitude level *A* of the RF signal for every phase angle. Selecting VGIN was the subject of extensive study. A good phase response to the RF signal fed to the demodulator is supposed to give a circle with equally distributed RF input signal samples for every phase degree. The phase and amplitude of the signal for every shifted RF phase degree is determined by plotting the baseband components of the signal in the Eqs. (27) through (29). The measured *I* and *Q* values give a circle in the *I*-*Q* phasor plane. The ideal circle is supposed to be like the one in Figure 38. But, varying *I* and *Q* values for each demodulator gives the circles whose centers are not located in the origin of the phasor plane. The distances of the circle on the axes *I* and *Q* were obtained by measuring IOPP, IOPN, QOPP, and QOPN, and using them in a MATLAB program written to plot and compute the circle of the demodulator. The data for each demodulator, as a result of measurements, are listed in Table 3. The graphs showing *I* vs. *Q* values and transmitted phase difference between received and transmitted phases for each board are shown in Appendix F. The optimum value of VGIN for most operating conditions was determined to be 0.38 V. This value gives the largest diameter circles, which are less sensitive to noise. The circle offsets will be taken out in the processing.

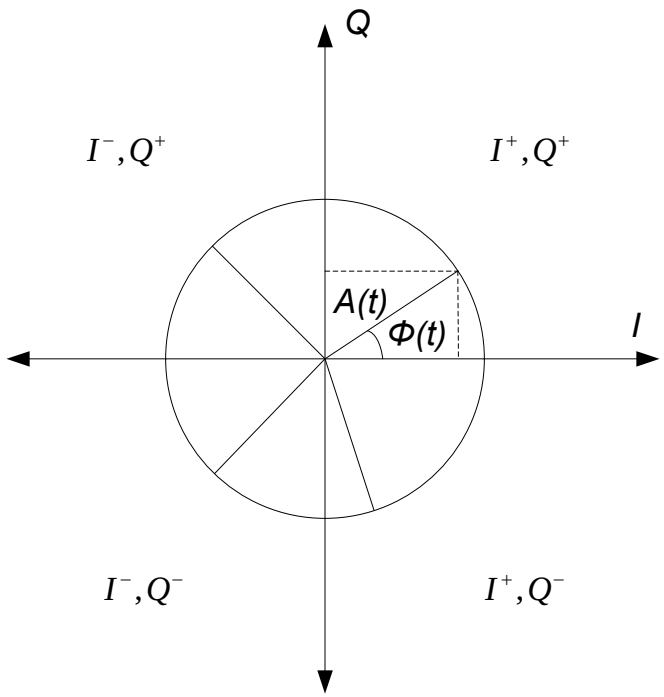

Figure 38 Phasor In-phase and Quadarature-Phase plane.

Board No	**Diameter of the Circle (mV)**		**Center Coordinates (mV)**	
0	ΔI	~ 94	I	-0.0465
	ΔQ	~ 94	Q	0.0212
1	ΔI	~ 125	I	-0.0993
	ΔQ	~ 125	Q	0.0385
2	ΔI	~ 96	I	-0.0061
	ΔQ	~ 96	Q	0.0259
4	ΔI	~ 92	I	0.0011
	ΔQ	~ 98	Q	0.0177
5	ΔI	~ 106	I	-0.0285
	ΔQ	~ 98	Q	0.0344
6	ΔI	~ 98	I	-0.0864
	ΔQ	~ 96	Q	0.0604
7	ΔI	~ 103	I	-0.0113
	ΔQ	~ 95	Q	0.0027
9	ΔI	~ 99	I	-0.0102
	ΔQ	~ 103	Q	-0.0033

Table 3 The parameters measured for each demodulator.

The other components that need to be characterized are the cable and the 2-way power splitter that feeds the LO signal to the demodulators through the two 4-way splitters. The 2-way splitter used in the system is Anaren 40266 power divider operating within the frequency range 2 through 4 GHz. Using the VNA, the deviation from the linear phase was measured for the cables with the 2-way splitter. The cable giving the least phase deviation, 400 millidegrees, was chosen among the other cables.

The 4-way splitters used in the system are Merrrimac PDM-42-2.75G power dividers. To measure the phase deviation, the RF signal from VNA is transmitted to two 4-way splitters through the selected 2-way splitter as shown in Figure 39. Except for the port to be measured, all the others were terminated to prevent reflections. Using the first port of one of the 4-way splitters as a reference, the deviation from linear phase was measured for every other junction of the two 4-way splitters. The results and are listed in Table 4. All were within the ± 10 degree limits that manufacturer specifies.

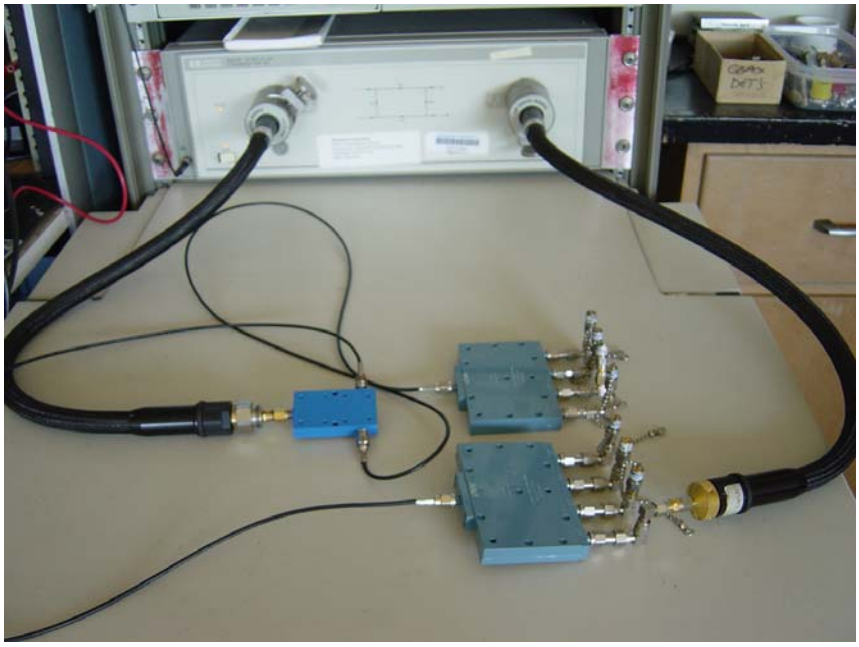

Figure 39 The setup for deviation from linear phase measurement for 4-way splitters.

4-Way Splitter 1		4-Way Splitter 2	
Junction No	Phase Difference (°)	Junction No	Phase Difference (°)
1	-0.215	1	-7.4419
2	1.3884	2	-5.5991
3	0.500	3	-4.9316
4	-1.4186	4	-4.6143

Table 4 The phase differences for each port on both 4-way splitters.

C. ARRAY ASSEMBLY

After characterizing the components, the system was assembled and tested. A wooden base to mount the system components was cut approximately 0.38 m by 0.60 m. The aperture ground plane was cut 0.215 m by 0.58 m, then holes of 0.09 m were drilled for each dipole at a spacing of 0.065 m. A half a wavelength extension (0.0625 m) was left between the elements and the edges of the ground plane. The dimensions of the array ground plane on which the elements are placed are 0.215 m by 0.58 m as seen in Figure 14. The ground plane was covered with copper to make it a good conductor to increase gain and shield the components. The ground plane was attached to the wooden base with screws and two wooden supports.

The demodulators were stacked in 2 sub-assemblies of 4 each. The $+V_S$ and GND terminals of the voltage supply were connected with soldered thin wires, so a 5 V supply voltage could be fed to all the demodulators in parallel. The 4 demodulators in each sub-assembly are held together with screws and supported with plexiglass on each side.

The reconfigurable chassis NI cRIO-9104 with the real-time embedded controller cRIO-9004 was located in the middle of the wooden base with its center located at the center of the two sub-assemblies of demodulators. Eight NI cRIO-9215 analog input modules were plugged in the RS-232 connections in the chassis slots as shown in Figure 35. Terminal 9 (common (COM)) of the analog input module was connected to terminal

7 which is ground of *QOPN* to reduce the noise. The outputs, *IOPP*, *IOPN*, *QOPP*, and *QOPN* were wired to the corresponding channels on the input modules and were tested to confirm they all ran properly.

Two HP 6550 A linear power supplies, one for each demodulator sub-assembly, were connected to 12-way terminals to dispatch the 5, and +12 V to the components of the system. The ports on the 12-way terminals are painted in black for ground, red for 5 V, blue for +12 V, and green for -12 V. VGIN for each modulator must be reduced to 0.38 V and this is done via a VGIN voltage regulator designed and made by Bob Broadston. The VGIN voltage, which was adjusted with a multimeter, is provided to the demodulators through two bundles of 4 cables. The 5 V is provided to the V_S of the demodulator and 12 V to the LO with VGIN by the power supplies.

The Z-Communications LO provides the RF frequency at 2.4 GHz to the demodulators. Before connecting the LO to the 2-way splitter and the power supply, the LO frequency was adjusted to 2.4 GHz. Accounting for the 30 dB attenuator connected to the power meter, the power measurement of the LO output was found to be 0.94 dBm. Given that the 2-way and 4-way splitters give a loss of 9 dB, the LO power to the demodulators is estimated to be -8.06 dBm. This LO power is within the limits defined in [22].

The LNA and dipoles were placed last. The LNAs are connected to the dipoles with barrels in order to minimize the feedline losses. The LNAs are connected to the RFIP input of the demodulators with the cables. The cables that RF energy is transmitted through need to be the same length to prevent any phase differences. The cables that are used in the system set-up meet this requirement.

The other component of this research set-up is anechoic chamber which is the test range for the system. Anechoic chambers are widely used for testing electromagnetic and acoustic properties of all kinds of equipment. In most cases, an open environment is not convenient for these tests due to the different noise sources. A room lined with absorbing material is referred to as an anechoic chamber. Anechoic chamber simulates the free space environment by reducing the reflections with the help of its absorbers on its walls. It provides an environment to determine the antenna patterns and parameters such as gain, HPBW, and side lobe level. [26]

The anechoic chamber located at the NPS has a VNA similar to that was used to characterize the system components. The dimensions of this chamber can be seen in Figure 40. The VNA is connected to a 2.4 GHz horn antenna and the antenna is placed on a pedestal facing the transmit horn antenna. The horn antenna simulates the antenna of a UAV transmitting a continuous wave (CW) signal. Rotating the pedestal, the movement of UAV with respect to tracking array system is simulated. The array will scan to track the CW signal from the horn antenna. The computed angle can be compared to the actual rotation angle to obtain the tracking error.

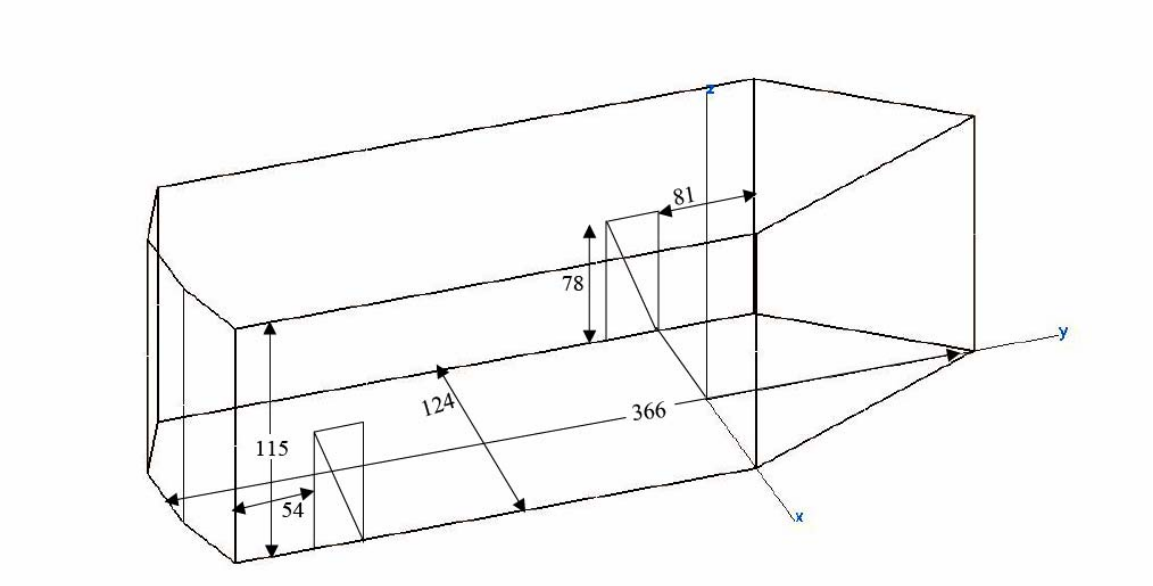

Figure 40 Specification of the anechoic chamber at the Naval Postgraduate School. Monterey, CA (Spanagel Hall Room 604) [27]

D. LABVIEW CONTROLLER SOFTWARE

LabVIEW is a software package by National Instruments that serves as an interface to hardware. This software has been available since 1986. The latest version is LabVIEW 8.20. LabVIEW has brought a big advantage to engineers by adding an option to use MATLAB within the LabVIEW environment. LabVIEW Virtual Instrumentation (VI) programs have applications in design (signal and image processing), embedded system programming (PC, FPGA, Microcontroller), simulation and prototyping), control (automatic controls and dynamic systems, mechatronics and robotics) and measurement (circuits and electronics, instrumentation).

Virtual Instrumentation (VI) is the user interface and computational engine of LabVIEW. This enables the users to create user-defined solutions that meet their specific needs, which is a very good alternative to the fixed functionality of traditional instruments. Moreover, VI removes the need for different instrument controllers.

E. LABVIEW PROGRAM

The LabVIEW program used in the research was based on a basic VI from the NI website and modified by Professor David Jenn to measure the outputs from one demodulator, display the data and calculate the amplitude and phase. The program of three VIs on two platforms communicating with each other: host-VI, FPGA-VI, and Sub-VI. Averaging was added to the host program to provide a stable output to 4 digits. The program was tested for one module then extended to eight modules. Finally the MATLAB program for the array system tracking and pattern calculation was added.

The compiled program is downloaded to the FPGA on the chassis. It receives all the output voltages from the analog input modules (NI cRIO-9215) and processes them to obtain analog input calibration data and error data as shown in Figure 41. The loop rate of the FPGA program is entered in microseconds. It adjusts the loop rate of the host program as well, since there is handshaking between the host and remote (FPGA).

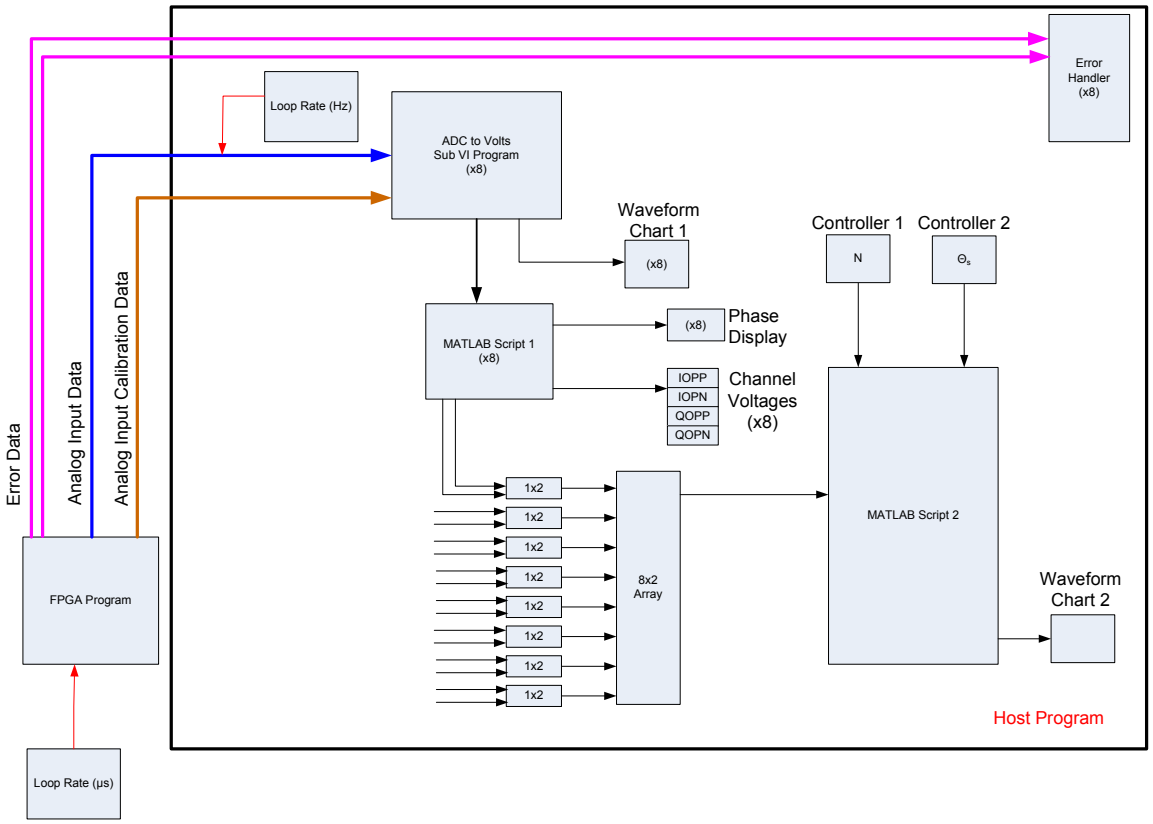

Figure 41 LabVIEW Software Data Flow Diagram.

The analog input data is fed to the host program continuously. The FPGA and host programs transfer data by the means of handshaking. The FPGA program triggers the interrupt request node and enables it to send the data to the host program. The analog input data and analog input calibration data are fed into a sub-VI running in the host program. The Sub-VI converts the 16 bit data to voltages. The voltage outputs are fed into "Waveform Chart 1" and "MATLAB Script 1" in Figure 41. "Waveform Chart 1"shows all the outputs of the demodulator (IOPP, IOPN, QOPP, QOPN) graphically. "MATLAB Script 1" calculates the differential *I* and *Q* voltages and provides an input to "Phase Display" and "Channel Voltages" seen in Figure 39. *I* and *Q* voltage values are built as an array for each module and then assembled to an 8-by-2 array that provides the input data to "MATLAB Script 2". MATLAB Script 2 has two more inputs provided by "Controller 1" for number of elements and "Controller 2" for the scan angle. All these data are used to calculate the pattern of the array and make the system track the signal transmitted by UAV. The resulting data is displayed to the user in "Waveform Chart 2".

If any error occurs within the system, the signal is sent from FPGA to the host program. The error handler warns the user about the problem. This procedure is repeated for all eight modules.

F. INTEGRATION OF THE COMPONENTS

The integration of the components in a system can be the most difficult and challenging part of design. When the components are combined into a system, the compatibility of these components is a major problem. The characteristics of one component might change due to the other components. For example, mismatches between components can lead to standing waves and phase errors. Also, RF components radiate, which can couple to other components.

To verify the correct installation and operating conditions for the system, the total insertion phase of the channels was measured. The system was fed with a LO and RF signal from the VNA and the required bias voltages set from the HP 6255A Dual DC linear power supplies for more accurate measurements. The *I* and *Q* demodulator voltages were measured again with a 30 degree increment for each demodulator. These measurements, shown in Table 5, gave different off-center values and diameters from those in Table 3. This difference showed that the characteristics of the demodulators connected to the LNAs were affected by each other and the LNAs. This is likely due to DC introduced by the amplifiers, although this issue needs further investigation.

Board No	Diameter of the Circle (mV)		Center Coordinates (mV)	
0	ΔI	~76	I	-0.0595
	ΔQ	~69	Q	0.0428
1	ΔI	~111	I	-0.1025
	ΔQ	~104	Q	0.0481
2	ΔI	~85	I	-0.0132
	ΔQ	~100	Q	0.0311
4	ΔI	~76	I	0.0058
	ΔQ	~86	Q	0.0372
5	ΔI	~88	I	-0.0163
	ΔQ	~84	Q	0.0142
6	ΔI	~79	I	-0.1091
	ΔQ	~74	Q	0.0442
7	ΔI	~95	I	-0.0258
	ΔQ	~101	Q	0.0033
9	ΔI	~94	I	-0.0248
	ΔQ	~92	Q	0.0315

Table 5 The parameters remeasured for each demodulator when integrated in the system.

The phase data for the demodulators connected to the LNAs was plotted with the MATLAB code shown in Appendix G. The received phase was calculated in the same way as in Eq. (27) through Eq. (29), and then the received phases of each demodulator were compared to the transmitted phases from the VNA as seen in Figure 42.

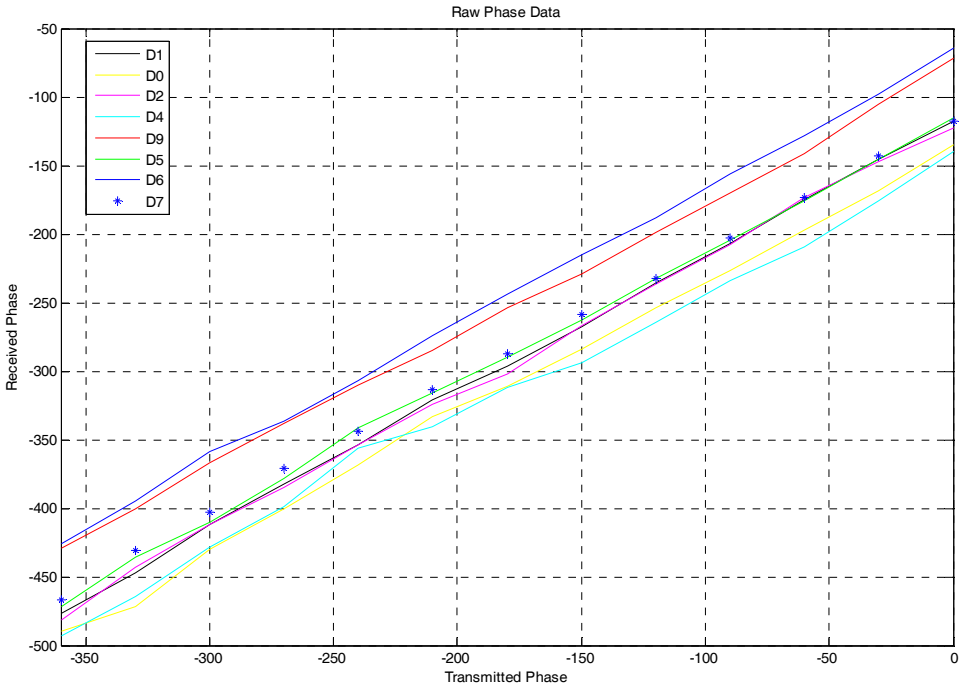

Figure 42 Transmitted phase vs. received phase for each demodulator with an LNA.

Using the least squares method, a straight line fit to data was found for each demodulator. In this way, the offset phase for each demodulator was found (Table 6). The fitted curves can be seen in Figure 43, with the offsets subtracted.

Figure 44 shows the measured data with the offsets subtracted. These curves represent the actual values that will be used in the beam processing.

D1 (Reference)	**D 0**	**D 2**	**D 4**	**D 9**	**D 5**	**D 6**	**D 7**
0	-17.88	-1.44	-20.97	41.25	4.46	49.58	7.15

Table 6 The phase differences in degrees with respect to the reference demodulator, D1.

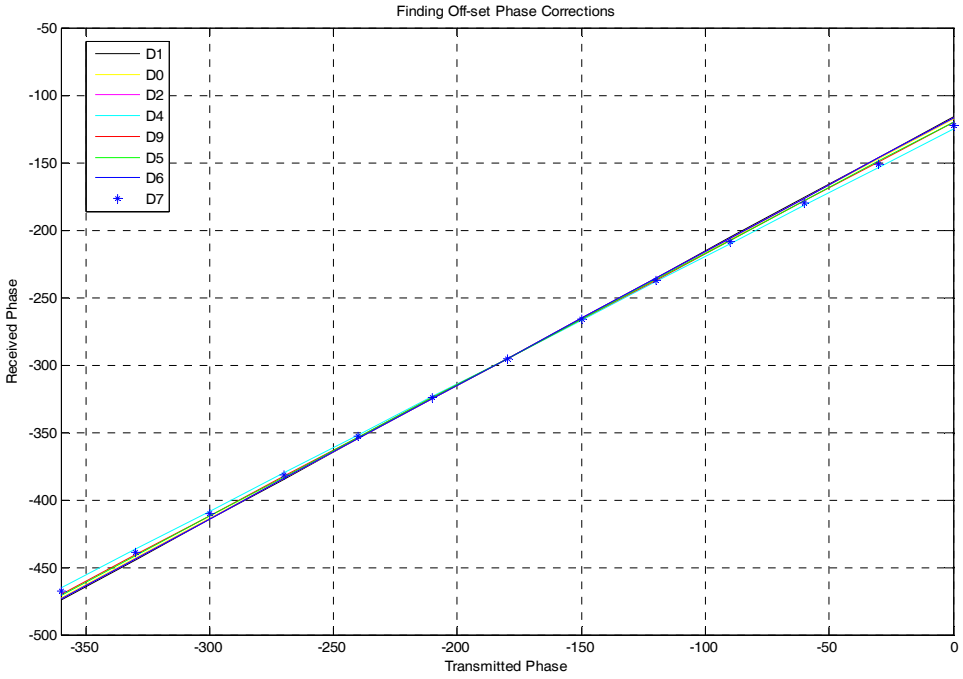

Figure 43 The approximate linear curve fit received phase vs. transmitted phase.

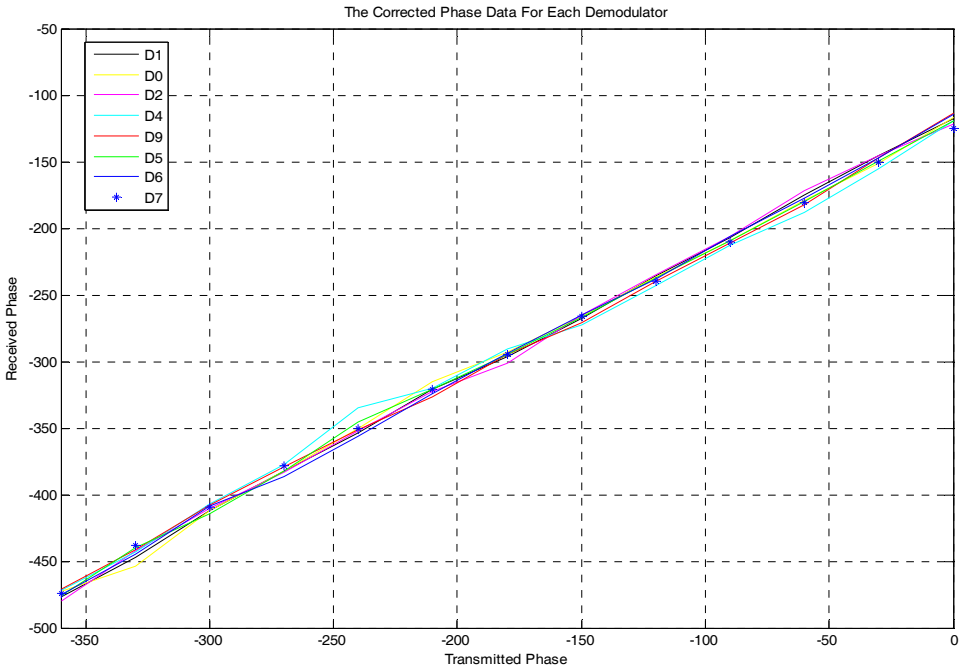

Figure 44 The measured received phase vs. transmitted phase after the phase offsets are subtracted.

The system components were characterized and the phase and voltage offsets were applied to the host VI. The system needed to be tested before taking the next step of testing the system in the anechoic chamber. To simulate a wave incident in the anechoic chamber, the dipoles were detached from the system and the RF signal at 2.4 GHz was fed directly to the LNAs from the VNA through an 8-way splitter. This simulates a plane wave incident from broadside. The sum and difference pattern distribution values corresponding to each 5 degree increment scan angle are plotted in Figure 45. The simulation of the actual values in MATLAB gives Figure 46 when the observation angle is zero. When the array patterns in Figure 45 are compared to those in Figure 46, it can be seen that they look similar. If a one degree scan angle increment was used instead of 5 degrees, more similar sum and difference pattern distributions could be obtained.

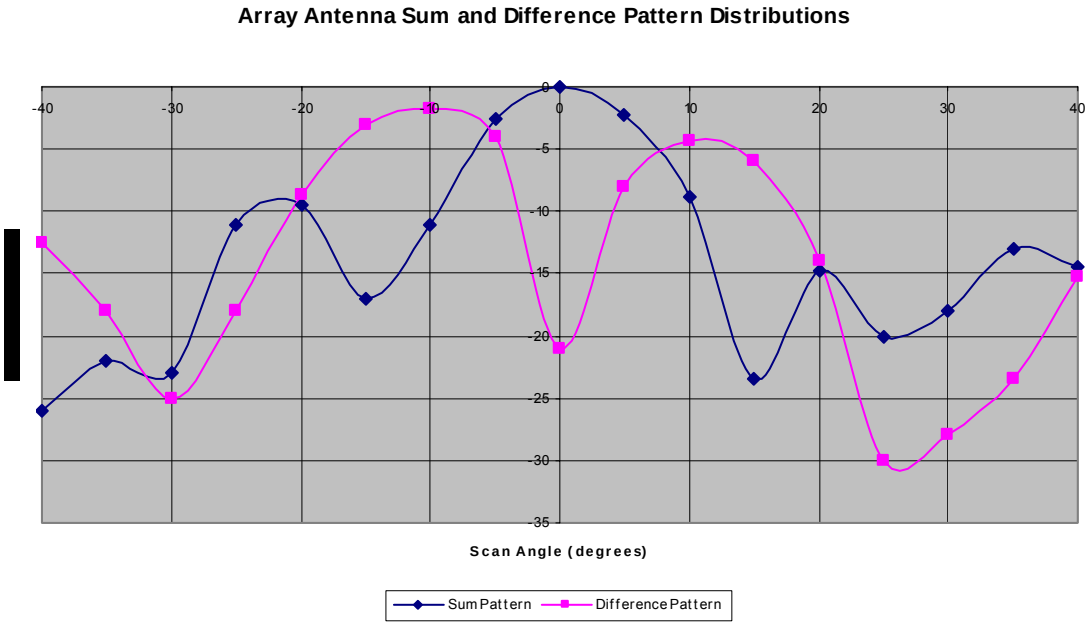

Figure 45 Measured array antenna sum and difference pattern distributions for broadside excitation when the beam is scanned.

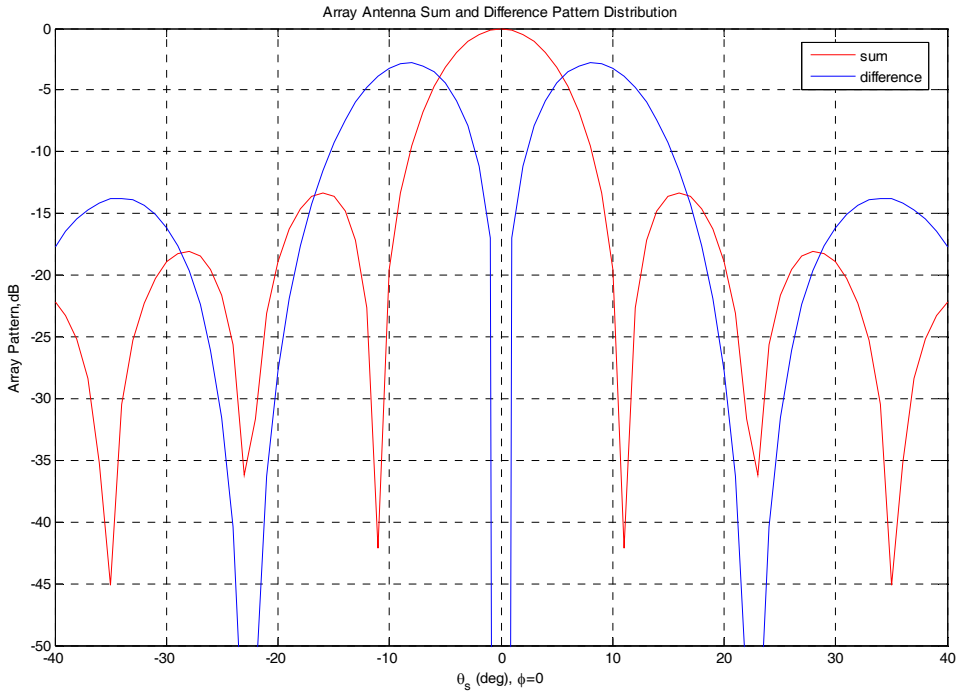

Figure 46 Calculated array antenna sum and difference pattern distributions for broadside excitation when the beam is scanned.

G. FINAL ANALYSIS OF THE ARRAY

After good sum and difference pattern distributions were obtained, the next step was to make the system track the signal. To achieve this goal, the host VI needed to be modified to find the angular difference between the difference beam null and the signal. Using this information the scan angle is updated. Feeding the updated scan angle to the MATLAB script calculating the sum and difference patterns, the difference beam null and sum beam peak can be swept to the direction of the signal.

The monopulse slope constant in Eq. (4) was recalculated for the results extracted from CST Microwave Studio simulation which was mentioned in Chapter III Section C and found to be -0.0775 instead of -0.12003 per degree. This new monopulse slope constant is put in MATLAB script as seen in Figure 47. The *I* and *Q* voltages from each cRIO-9215 input module are fed to the MATLAB script as an 8-by-2 array. The value 0 is assigned to the initializer terminal of the feedback node to start the system at the position where the array is broadside to the UAV transmitter. Eventually, this initial scan

value can be replaced by an acquisition algorithm. To obtain the new scan angle, the angular difference between the difference beam null and the signal, θ in Eq. (4) and *deltheta* in host VI, is subtracted from the scan angle. After the new scan angle is converted to degrees from radians, it is fed back to the MATLAB script where it is converted to radians again.

The tracking was tested by inserting an angle variable (*theta_in* in Figure 47) to the MATLAB script to simulate the plane wave arriving the array dipoles at different angles. Since this is an angle-tracking system, the amplitude is not used in the program.

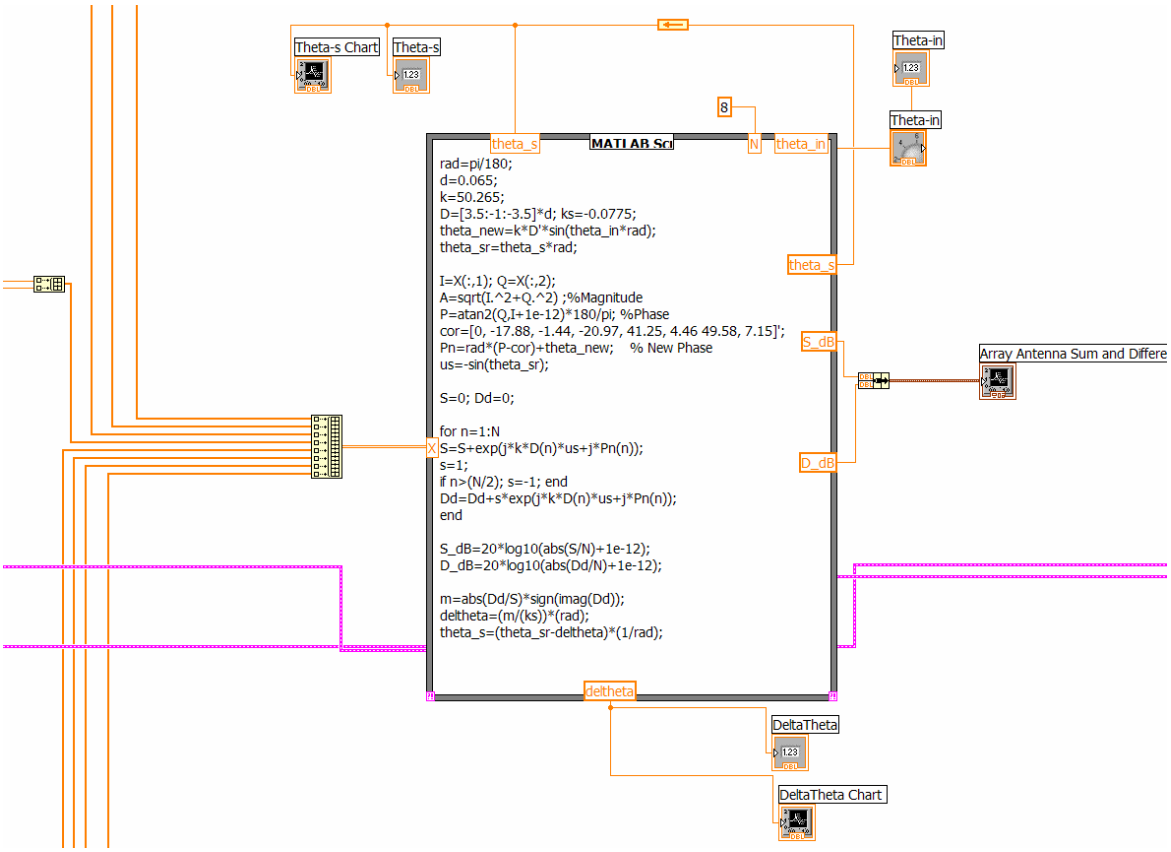

Figure 47 The block diagram of host VI.

The array antenna sum and difference pattern distributions display is seen in Figure 48. The sum pattern is approximately 0 dB and difference pattern is approximately -25 dB with an oscillation of ± 5 dB. When the sum and difference pattern distributions

are compared to those in Figure 45, their values are seen to be close to one another. In addition to the sum and difference distribution patterns, the scan angle and the angular difference between the difference beam null and the signal is shown in both a numeric indicator and a waveform chart as seen in Figure 48. The angle of the simulated plane waves are controlled by a knob controller on the front panel and displayed in a numeric indicator with a text of *Theta_in*. The system was tested for angles range changing from -40 to 40 degrees and it was observed that the scan angle was within ± 2 degrees of the angle of the signal.

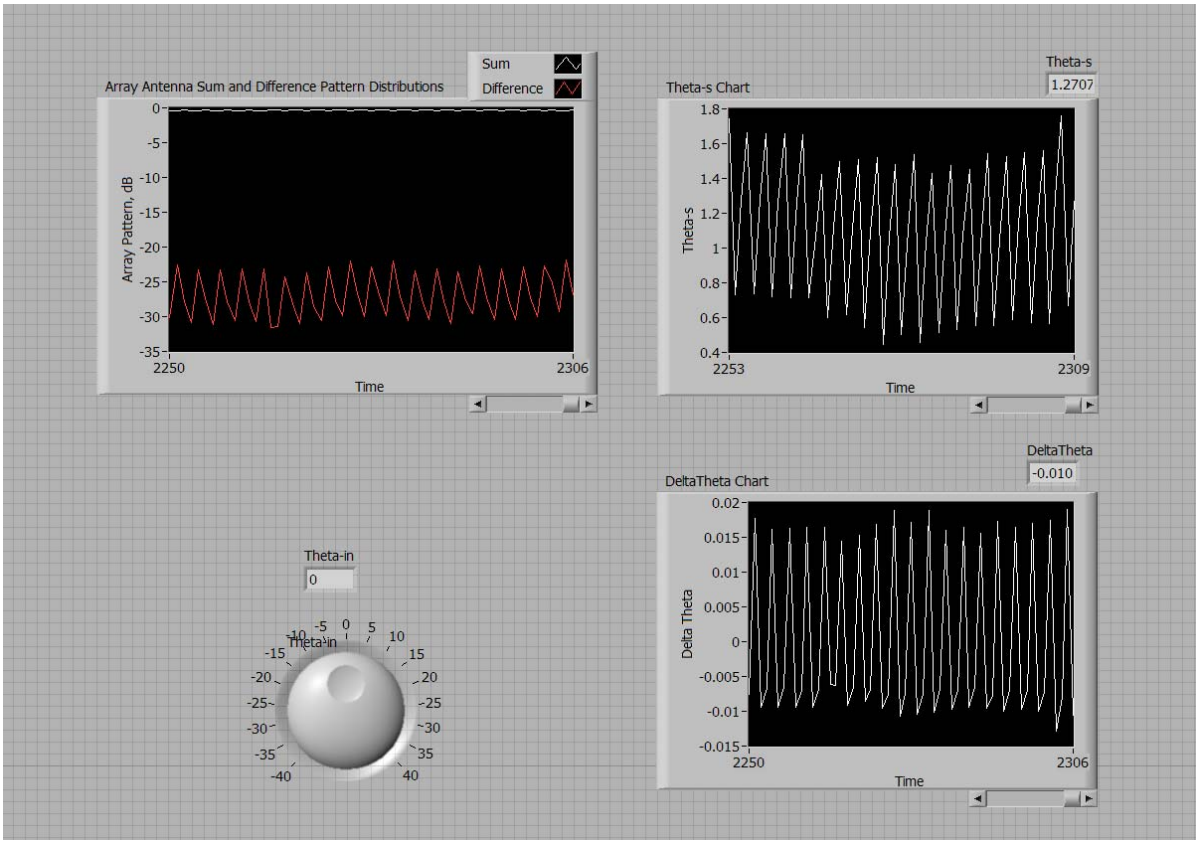

Figure 48 The front panel of host VI showing array sum and difference amplitudes (left), beam scan angle (upper right) and pointing correction (lower right).

This chapter covered the tracking array hardware and simulations of the system. In Section A, the system components were described. Section B summarized how the system components were characterized. Array assembly is mentioned in Section C. Information about the LabVIEW software was given in Section D. In Section E, the Lab

VIEW programs designed for this project were explained. How the system components were built up in a system was discussed in Section F. Lastly in Section G, the results of the tracking simulation of the array antenna system was shown.

THIS PAGE INTENTIONALLY LEFT BLANK.

V. CONCLUSION AND RECOMMENDATIONS

A. SUMMARY AND CONCLUSION

As a part of an ongoing project, this research aimed to track a signal transmitted continuously by a UAV via an array of antennas. Tracking this signal will be the first step towards maintaining a data link between a UAV and ground station for any kind data transfer such as video, image, or audio. The remaining steps to be taken to achieve this object are summarized in Section B as recommendations for future work.

This research has covered the design and development of the tracking array beginning with background about tracking systems and techniques and the causes of tracking errors.

The array uses a monopulse difference beam to track the UAV signal. The array was designed based on typical UAV operational requirements. This led to the selection of array parameters such as number of elements and spacing.

The array hardware was selected and its performance characterized in the lab. After assembly of the components, benchtop testing verified the beam patterns. The beams were successfully scanned and the tracking algorithm was incorporated and tracking simulated. A photograph of the current configuration is shown in Figure 49.

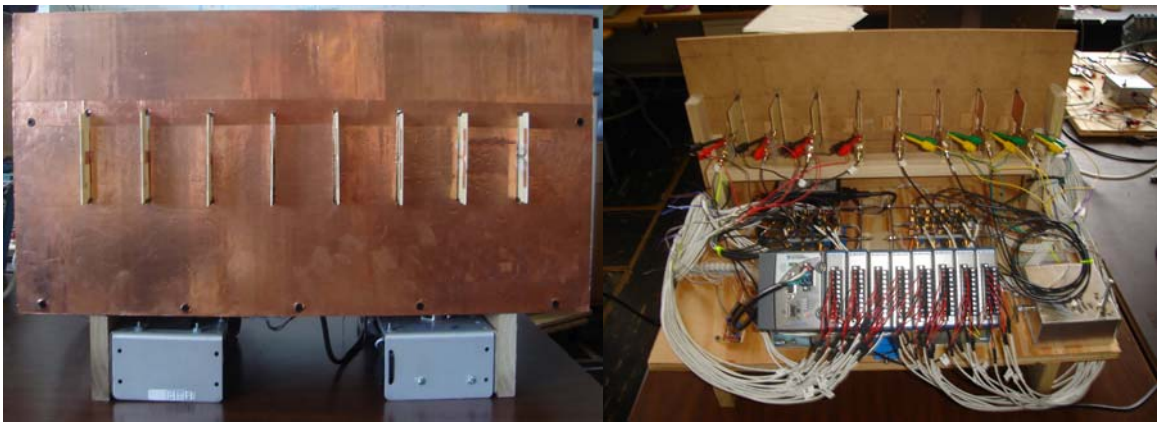

(a) **(b)**

Figure 49 a) The front view of the current system configuration. b) The back view of the current system configuration.

The array parameters were initially determined via MATLAB programs. Then, the system was simulated with CST Microwave Studio to include the affects of the ground plane and mutual coupling on the system performance. This gave more realistic values.

By compensating for the differences between components in the signal processing, the array performance was improved. LabVIEW programs designed for this research made the tracking of the signal possible.

As discussed in Chapter IV Section G, the simulation results in lab conditions gave very accurate results. However, these results should be verified in the anechoic chamber to achieve the final objective of this research.

B. RECOMMENDATIONS FOR FUTURE WORK

1. Circularly Polarized Antennas

The dipoles that are set in the array are linearly polarized. In light of those findings mentioned in Chapter III Part B, it can be said that both of the antennas should preferably be circularly polarized for the best performance when the UAV is maneuvering.

2. Simplifying LabVIEW Program

The response rate of the array depends the complexity the LabVIEW program for tracking. The program needs to be simplified to make the array respond quicker. The amplitude and phase is calculated twice; once for the actual *I* and *Q* voltages and once for the average *I* and *Q* voltages. Also, the actual *I* and *Q* voltages are displayed as a waveform chart to make sure that the right *I* and *Q* voltages are obtained. The LabVIEW host VI takes an average of 100 samples, and this rate can be decreased to improve speed if it does not affect the tracking performance of the system.

3. Acquisition System

The array system designed for this research project does not have the capability of acquiring the target. Hence, the target is acquired manually. Sweeping the sum and difference beams simultaneously, the signal transmitted continuously from the target can be acquired and tracked.

4. Verifying the Pattern Distributions

The array should be tested in an anechoic chamber and the results should be compared to the sum and difference pattern distributions obtained with CST Microwave Studio.

5. Data Transfer

Although the specific type of UAV for the system has not been defined yet, its desired purpose is troop support, carrying out reconnaissance and surveillance missions. Thus, after the tracking of the signal transmitted by UAV is achieved, the collected data transfer to the system should be accomplished. The system is a non-coherent system, because does not have the same phase references for the receiver and transmitter. The coherent detection requires a carrier recovery circuit that can extract the data from the received signal by the means of Binary Phase-Shift Keying (BPSK) which uses two phases, also known as 2-PSK or Quadrature Phase-Shift Keying (QPSK) which uses four phases, also known as 4-PSK.

6. Operational Testing

After the array has been tested, it should be taken to the field and its operability with a real UAV should be checked. This last step will reveal the vulnerabilities of the system and lead to further improvements.

THIS PAGE INTENTIONALLY LEFT BLANK.

APPENDIX

A. MATLAB CODES TO DEFINE THE DESIGN PARAMETERS

```
% element spacing vs. scan angle .

clear; clc;
rad=pi/180;
freq=2.40*10^9;
lambda=3*10^8/freq;
theta_s=0:60; theta_s_rad=theta_s*rad;

d=lambda./(1.+abs(sin(theta_s_rad)));
d_l=((1.+abs(sin(theta_s_rad)))).^(-1);

figure(1)
plot(d,theta_s);
grid on;
title(['Scan Angle vs. Element Spacing  ( freq = 2.40 GHz)']);
xlabel('element spacing,d (m)');
ylabel('\theta_s (deg)');


% Element Spacing vs. Gain for Parallel Short Dipoles

clear; clc;

rad=pi/180;

freq_i=input('Enter the frequency (2.4, 2.45 or 2.5) = ');
freq=freq_i*10^9; lambda=3*10^8/freq;  k=(2*pi)/lambda;

a_0=2/3; % For parallel short dipoles.
alpha=0; % Uniformly excited elements (No interelement phase shift).

for N=2:2:12

   t=1;

   for d=0:0.0001:0.25

% The upper boundary for this array is 2*lambda which is equal to 0.125*2 for freq= 2.4
GHz.
```

```
        temp=0;

        for m=1:(N-1)

            a_1=1-(1/((m*k*d)^2)); a_2=1/(m*k*d);

            temp=temp+((N-
m)/(m*k*d))*((a_1*sin(m*k*d))+(a_2*cos(m*k*d)))*(cos(m*alpha));

        end

        D=1/((a_0/N)+((2/(N*N))*temp));

        Display(t,1)=d; Display(t,2)=D;

        t=t+1;

    end

    figure(1)
    plot(Display(:,1),Display(:,2)); hold on; grid on;
    title(['Element Spacing vs. Gain for Parallel Short Dipoles (freq= ', num2str(freq_i),'
GHz)']);
    xlabel('element spacing, d (m)'); ylabel('Gain');
    text(0.23,22,'N=12');
    text(0.23,18,'N=10');
    text(0.23,14.8,'N=8');
    text(0.23,11.3,'N=6');
    text(0.23,7.2,'N=4');
    text(0.23,3.7,'N=2');

    figure(2)
    line([0 0.25],[0 2*N],'color',[1 0 0]); grid on;
    title(['Element Spacing vs. Gain for Parallel Short Dipoles(freq= ', num2str(freq_i),'
GHz)']);
    xlabel('element spacing, d (m)'); ylabel('Gain');
    text(0.23,22,'N=12');
    text(0.23,18,'N=10');
    text(0.23,14.3,'N=8');
    text(0.23,10.2,'N=6');
    text(0.23,7.0,'N=4');
    text(0.23,3.2,'N=2');

end
```

```
%  Element Spacing vs. Gain for Parallel Short Dipoles

clear; clc;

rad=pi/180;

freq_i=input('Enter the frequency (2.4, 2.45 or 2.5) = ');
freq=freq_i*10^9; lambda=3*10^8/freq; k=(2*pi)/lambda;

a_0=2/3; % For parallel short dipoles.
alpha=0; % Uniformly excited elements (No interelement phase shift)
d=input('Enter element spacing in meters= '); % Element spacing in meters.

t=1;

for N=2:2:12

    temp=0;

 for m=1:(N-1)

   a_1=1-(1/((m*k*d)^2)); a_2=1/(m*k*d);

   temp=temp+((N-m)/(m*k*d))*((a_1*sin(m*k*d))+(a_2*cos(m*k*d)))*(cos(m*alpha));

end

    D=1/((a_0/N)+((2/(N*N))*temp));

    Display(t,1)=N; Display(t,2)=D;

    t=t+1;

end

plot(Display(:,1),Display(:,2));hold on;
grid on;
title(['Number of Elements vs. Gain for Parallel Short Dipoles ( freq = ',num2str(freq_i),'
GHz & d= ', num2str(d),' m )']);
xlabel('# of Elements (N)'); ylabel('Gain');
```

```
%  Scan Angle vs. HPBW

clear; clc;

rad=pi/180;

freq_i=input('Enter the frequency (2.4, 2.45 or 2.5) = ');
freq=freq_i*10^9; lambda=3*10^8/freq; k=(2*pi)/lambda;

d=input('Enter element spacing in meters= ');

for N=2:2:12

   i=0;

   for theta_s=0:60

      i=i+1;
      HP1=0.886*lambda./(N.*d);
      theta_s_rad=theta_s*rad;
      HPBW(i)=(HP1/(cos (theta_s_rad)))*(180/pi);
      T(i)=theta_s;

   end

   plot(T, HPBW); hold on; grid on;
   title(['Scan Angle vs. HPBW ( freq =',num2str(freq_i), 'GHz', ' & ', 'd= ',num2str(d), '
m )']);
   xlabel('Scan Angle (\theta_s)');ylabel('HPBW (deg)');
   text(30, 60, 'N= 2');
   text(30, 31,'N= 4');
   text(30, 21, 'N= 6');
   text(30, 16,'N= 8');
   text(30, 12, 'N= 10');
   text(30, 8,'N= 12');

end
```

B.1. MATLAB CODE FOR TRACKING ERROR AND MONOPULSE SLOPE CONSTANT CALCULATION

```
%  This programme shows the difference between the tracking angle and actual
%  angular position of the target versus time. This program originates
%  from the slope error constant formula which is  K*delta_theta = Sigma / Delta

clc;clear;

rad=pi/180;
freq=2.40*10^09; lambda=3*10^08/freq;

theta_A=90; d=0.065; HPBW= 16; N=8;

k=(2*pi)/lambda;

v=30; Rmax=1000; Ro=Rmax*cos (40*rad);

x=Ro*tan(40*rad); % Scan angle is 40

tlast=(2*x)/v; tlast=ceil(tlast); % rounding up to the nearest integer towards infinity

t=0;

angle_1=(HPBW*(-.25)); angle_2=((HPBW)*(.25)); deltaHPBW=HPBW/20;

N_angles=floor((angle_2-angle_1)/deltaHPBW)+1;

for p=1:N_angles

   As(p)=((p-1)*deltaHPBW)+angle_1;

   y=sin(As(p)*rad); u=exp(j*k*d*y);  S_s=0; D_s=0;

   for z=1:N

      S_s=S_s+(u^(z-1));

      ss=1;

      if z>(N/2);ss=-1;end

      D_s=D_s+(ss*(u^(z-1)));

   end
```

```
    D_S_m(p)=abs(D_s/S_s)*sign(imag(D_s));
end
Ko1=polyfit(As,D_S_m,1); Ko=Ko1(1); display(['Slope constant is ', num2str(Ko)]);
a=1; N_timesteps=0; theta_s=-40;
x=Ro*tan(theta_s*rad)
for t=0:a:tlast
    N_timesteps=N_timesteps+1;
    y_s=sin(theta_s*rad)
    xo=Ro*tan(-40*rad); x=xo+(v*t);
    theta_t_rad=atan((v*t+xo)/Ro);
    theta_t=theta_t_rad*(180/pi);
    Tt(N_timesteps)=theta_t;
    y_t=sin(theta_t_rad);
    u_t=exp(j*k*d*y_t)*exp(-j*k*d*y_s);
    m=0; S_t=0; D_t=0;
    Ts(N_timesteps)=theta_s
    T(N_timesteps)=t;
    for n=1:N
        S_t=S_t+(u_t^(n-1));
        st=1;
        if n>(N/2); st=-1; end
        D_t=D_t+(st*(u_t^(n-1)));
    end
```

```
    D_S_t=abs(D_t/S_t)*sign(imag(D_t));

    deltatheta=D_S_t/(Ko*cos(theta_s*rad))

    theta_s=theta_s+deltatheta

end

figure(2)
plot(T,Tt-Ts,'r')
grid on;
xlabel('time (sec)');
ylabel('\Delta\theta');
title(['Angular Difference vs. Time for downrange of ', num2str(Rmax), ' m']);
```

B.2. MATLAB CODE WITH DIGITAL BEAMFORMING FOR TRACKING ERROR AND MONOPULSE SLOPE CONSTANT CALCULATION

```
% This program includes the digital beam forming to calculate the difference between
% the tracking angle and actual angular position of the target versus time. This program
% originates from the slope error constant formula which is K*theta = Sigma / Delta

clc;clear;

rad=pi/180;
freq=2.40*10^09;
lambda=3*10^08/freq;

theta_A=90; d=0.065; HPBW=16; N=8;

k=(2*pi)/lambda;

v=30; Rmax=1000; Ro=Rmax*cos (40*rad);

x=Ro*tan(40*rad); % Scan angle is 40

tlast=(2*x)/v; tlast=ceil(tlast); % rounding up to the nearest integer towards infinity

t=0;

angle_1=(HPBW*(-.25)); angle_2=((HPBW)*(.25)); deltaHPBW=HPBW/20;

N_angles=floor((angle_2-angle_1)/deltaHPBW)+1;

for p=1:N_angles

   As(p)=((p-1)*deltaHPBW)+angle_1;

   y=sin(As(p)*rad); u=exp(j*k*d*y);

   S_s=0; D_s=0;

   for z=1:N

      S_s=S_s+(u^(z-1));

      ss=1;

      if z>(N/2);ss=-1;end

      D_s=D_s+(ss*(u^(z-1)));
```

```
    end
    D_S_m(p)=abs(D_s/S_s)*sign(imag(D_s));
end
Ko1=polyfit(As,D_S_m,1); Ko=Ko1(1); display(['Slope constant is ', num2str(Ko)]);
a=1; N_timesteps=0; theta_s=-40;
x=Ro*tan(theta_s*rad);
for t=0:a:tlast
    N_timesteps=N_timesteps+1;
    xo=Ro*tan(-40*rad); x=xo+(v*t);
    theta_t_rad=atan((v*t+xo)/Ro);
    theta_t=theta_t_rad*(180/pi);
    Tt(N_timesteps)=theta_t;
    y_t=sin(theta_t_rad);
    IQ=cos(k*d*y_t)+(j*sin(k*d*y_t));
    m=0; S_t=0; D_t=0;
    Ts(N_timesteps)=theta_s;
    y_s=sin(theta_s*rad);
    DBF=cos(k*d*y_s)-j*sin(k*d*y_s); % DBF stands for digital beamforming
    u_t=IQ*DBF;
    T(N_timesteps)=t;
    for n=1:N
        S_t=S_t+(u_t^(n-1));
        st=1;
```

```
        if n>(N/2); st=-1; end

        D_t=D_t+(st*(u_t^(n-1)));

    end

    D_S_t=abs(D_t/S_t)*sign(imag(D_t));

    deltatheta=D_S_t/(Ko*cos(theta_s*rad));

    theta_s=theta_s+deltatheta;

end

plot(T,Tt-Ts,'r')
grid on;
xlabel('time (sec)');
ylabel('\Delta\theta');
title(['Angular Difference vs. Time for downrange of ', num2str(Rmax), ' m ( UAV Speed
is ', num2str(v), 'm/sec )']);
```

C. MATLAB CODE FOR ARRAY ANTENNA SUM AND DIFFERENCE PATTERN DISTRIBUTION

```
% This program calculates the sum and difference patterns of an array whose
% element factor is isotropic.

clc;clear;

rad=pi/180;
freq=2.40*10^09;
lambda=3*10^08/freq;

% Group pattern is assumed to be broadside. Theta_A will be perpendicular
% to the array face. Since it is broadside, the interelement phasing
% (alpha) is zero.

theta_A=90;
d=0.065;

HPBW= input ('Enter the desired Half Power Beamwidth in degrees : ');

k=(2*pi)/lambda;

HPBW_rad=HPBW*rad;
N_pre= (0.886*lambda)/(HPBW_rad*d*sin(theta_A));
N=round(N_pre); if mod(N,2)==1; N=N+1; end

L=N*d; %The length of the array
D=10*log10 (2*L/lambda); %Directivity for broadside pattern in dB.
display(['Directivity is ', num2str(D)]);
theta_s=input('enter scanning angle in degrees : ');
theta_s_rad=theta_s*rad;

phi=0.00;

m=0;

for angle=-90:1:90

   m=m+1;
   A(m)=angle;
   angle_rad=angle*rad;
   tt=sin(angle_rad)-sin(theta_s_rad);
   u=exp(j*k*d*tt);

   EF=cos(angle_rad);
```

```
   S=0;
   D=0;

for n=1:N

   S=S+(u^(n-1));

   s=1;
   if n>(N/2); s=-1; end

   D=D+(s*(u^(n-1)));

end

S_dB(m)=20*log10(abs((S*EF)/N)+1e-10);

D_dB(m)=20*log10(abs((D*EF)/N)+1e-10);

end

figure
plot(A,S_dB,'r',A,D_dB,'b');
grid off;
xlabel(['\theta(deg), \phi=',num2str(phi)]);
ylabel('Array Pattern,dB');
title('Array Antenna Sum and Difference Pattern Distribution');
legend('sum','difference');
axis([-90 90 -50 0]);
```

D. MATLAB CODE FOR RANGE CALCULATION FOR DIFFERENT BIT RATES

```
% The Application of Friis Equation to find the range to the target. Eq. (18) and Eq. (19)

% Gain is approximately 12 dB. (16.18)

clear; clc;

rad=pi/180;

freq_i=input('Enter the frequency (2.4, 2.45 or 2.5) = ');
freq=freq_i*10^9; lambda=3*10^8/freq; k=(2*pi)/lambda;

% fmax=2.5e09;fmin=2.4e09;

Pt= 1; % Pt= 1 Watt
Gt= 1; % Transmitter Gain
Gr= 10^(12/10); % Gt= 12 dB

k=1.38e-23;
Ts=94.07; % Room temperature is 290K.
B=100E06;

N=k*Ts*B;

BR=input ('Enter one of the Bit Rates(1=1 Mbps, 2=2Mbps, 3=5.5 Mbps, 4=11 Mbps )='); % See Table-2

display([' ']); display(['***** The Results *****']);
display(['Noise is ',num2str(N), ' W']);

switch BR

   case 1

      Pr_1= 10^((-94-30)/10);
      SNR_1=Pr_1/N;
      SNR_1_dB=10*log10(SNR_1);
      R_1=sqrt((Pt*Gt*Gr*(lambda^2))/(((4*pi)^2)*Pr_1));
      display(['Range is ',num2str(R_1), ' m and SNR is ',num2str(SNR_1_dB),'dB for Pr = -94 dBm ']);

   case 2

      Pr_2= 10^((-91-30)/10);
```

```
        SNR_2=Pr_2/N;
        SNR_2_dB=10*log10(SNR_2);
        R_2=sqrt((Pt*Gt*Gr*(lambda^2))/(((4*pi)^2)*Pr_2));
        display(['Range is ',num2str(R_2), ' m and SNR is ',num2str(SNR_2_dB),' dB for Pr
= -91 dBm ']);

    case 3

        Pr_3= 10^((-89-30)/10);
        SNR_3=Pr_3/N;
        SNR_3_dB=10*log10(SNR_3);
        R_3=sqrt((Pt*Gt*Gr*(lambda^2))/(((4*pi)^2)*Pr_3));
        display(['Range is ',num2str(R_3), ' m and SNR is ',num2str(SNR_3_dB),' dB for Pr
= -89 dBm ']);

    case 4

        Pr_4= 10^((-85-30)/10);
        SNR_4=Pr_4/N;
        SNR_4_dB=10*log10(SNR_4);
        R_4=sqrt((Pt*Gt*Gr*(lambda^2))/(((4*pi)^2)*Pr_4));
        display(['Range is ',num2str(R_4), ' m and SNR is ',num2str(SNR_4_dB),' dB for Pr
= -85 dBm ']);

    otherwise

        display ('DO NOT ENTER ANOTHER VALUE OTHER THAN 1,2,3,4')

end
```

E. MICROWAVE STUDIO SIMULATED PATTERNS OF THE GROUND PLANE

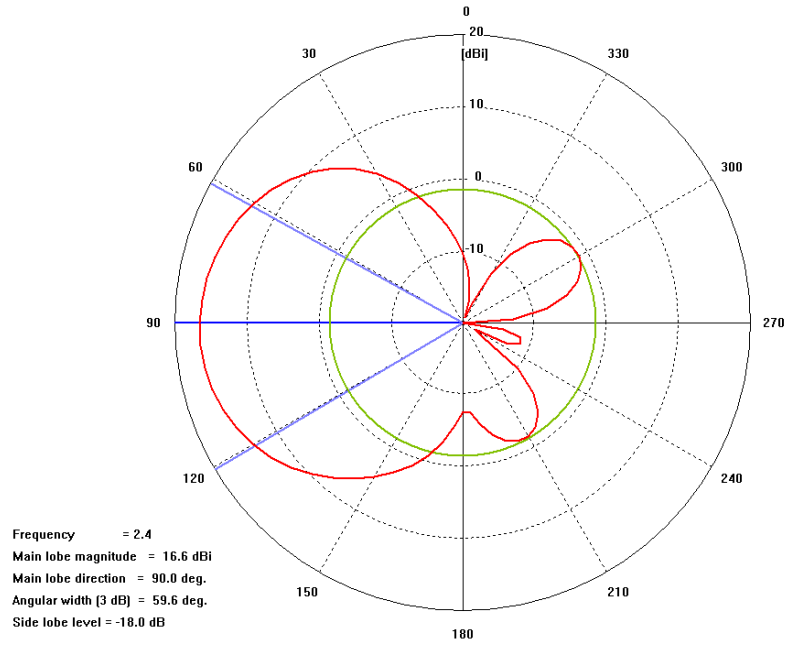

Figure E-1. The E-Plane of the array.

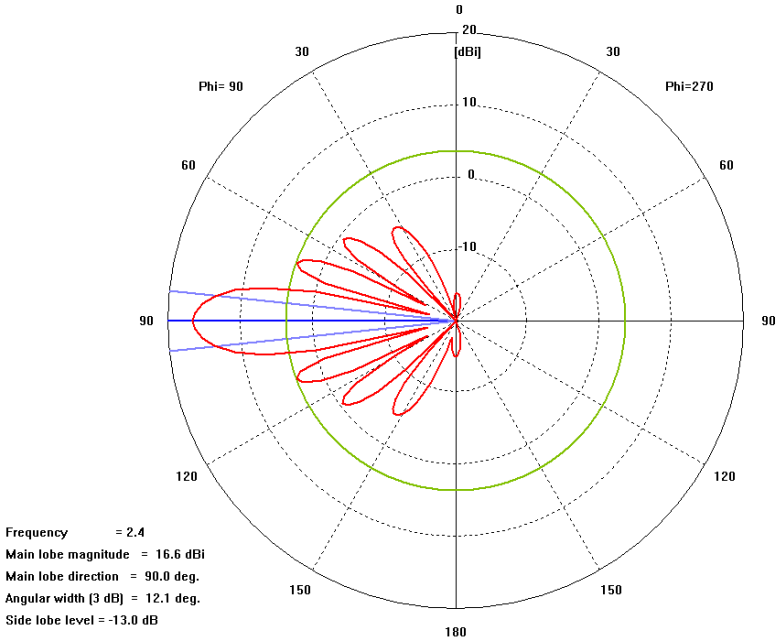

Figure E-2. The sum pattern of the array, no scan.

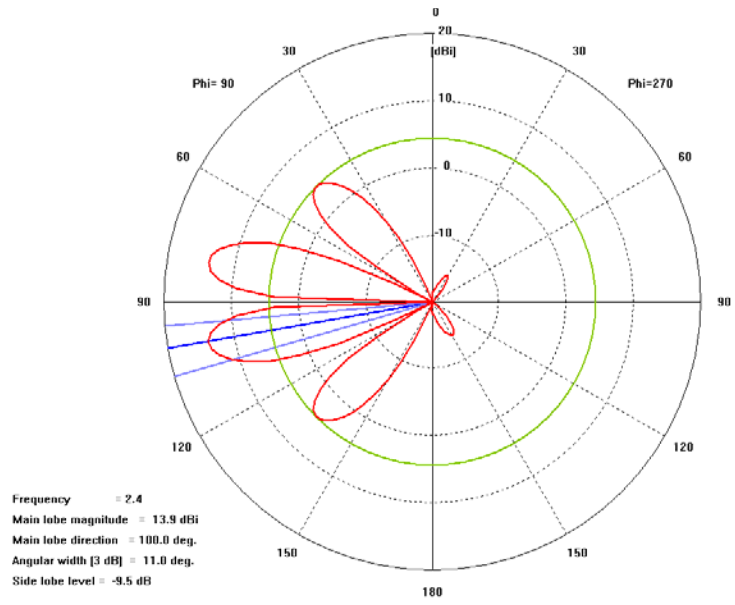

Figure E-3. The difference pattern of the array, no scan.

F. MATLAB CODE FOR CHARACTERIZING THE DEMODULATORS AND THE FIGURES OF THE MATLAB CODE

```
% This program asks for the off-center I and Q components of the baseband
% and the voltage applied from the user and gives two figures;
% transmitted I&Q vs. received I&Q
% transmitted phase vs. the difference between received  phase and
% transmitted phase.
clc;clear;

rad=pi/180; n=0;

Bno=input('Enter the board no : ');
deltaI=input('Enter the off-center I value : ');
deltaQ=input('Enter the off-center Q value : ');
V=input('Enter the voltage applied : ');

for phi0=0:360
   n=n+1;
   A(n)=phi0;
   Io(n)=V*cos(phi0*rad); Qo(n)=V*sin(phi0*rad);
   Ip(n)=Io(n)+deltaI; Qp(n)=Qo(n)+deltaQ;
   phi(n)=(atan2(Qp(n),Ip(n)));
end

phidiff=A-phi

figure(1)
plot(Io,Qo,'*',Ip,Qp,'+');grid on; axis equal;
xlabel('I (V)');ylabel('Q (V)');legend('Transmitted I&Q','Received I&Q');
title(['Transmitted I&Q vs. Received I&Q for Board No ',num2str(Bno)]);

figure(2)
plot(A',(unwrap(phi')*(180/pi))-A','-');grid on;
xlabel('\phi_0 (degrees)');ylabel('\phi - \phi_0 (degrees)');
title(['Transmitted Phase vs. Difference between the  Received and TransmittedPhases for
Board No ',num2str(Bno)]);
```

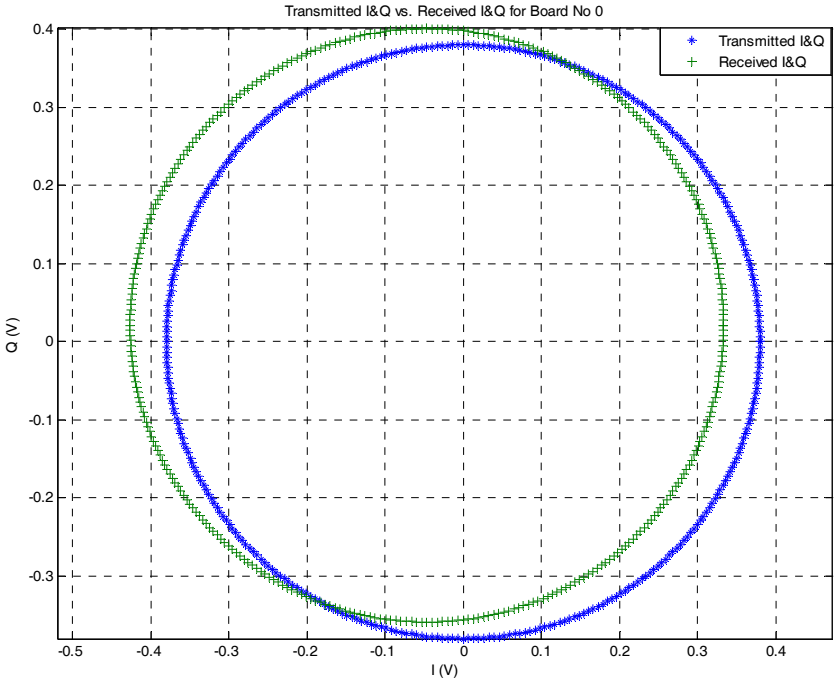

Figure F-1. Transmitted I and Q vs. received I and Q values for Board 0.

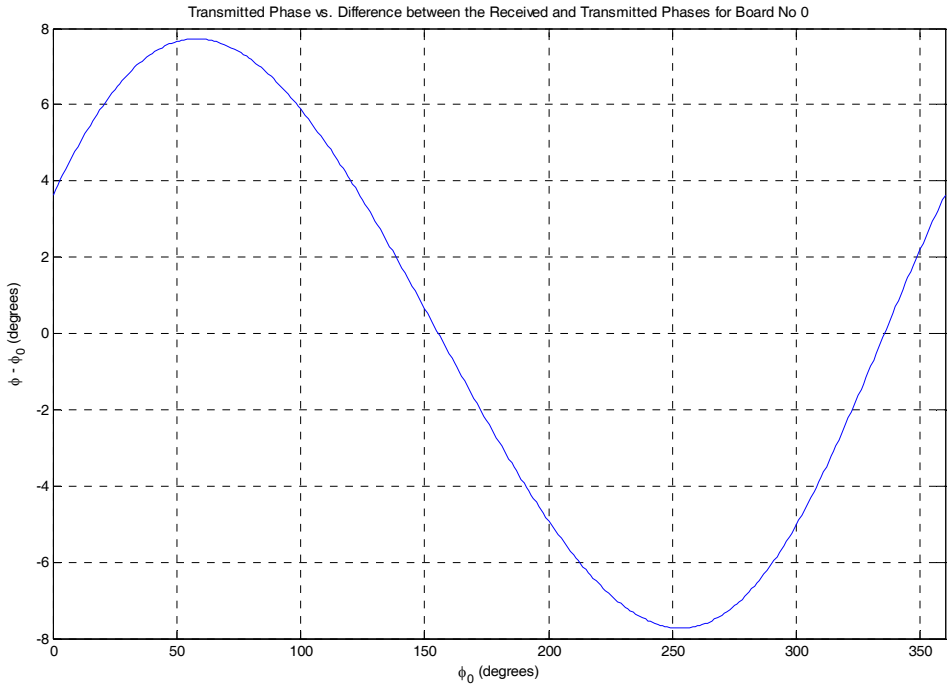

Figure F-2. Transmitted phase vs. the difference between the received and transmitted phases for Board 0.

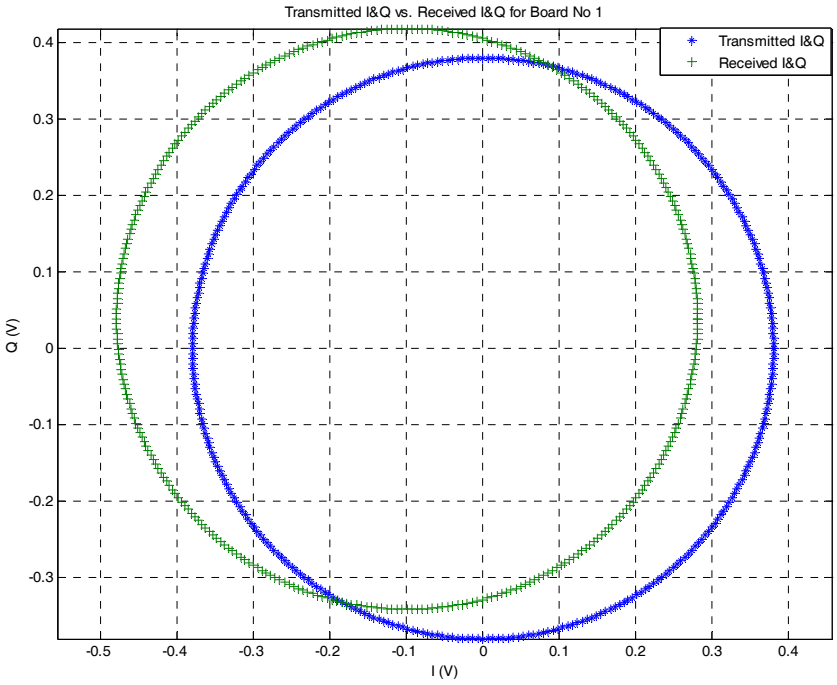

Figure F-3. Transmitted I and Q vs. received I and Q values for Board 1.

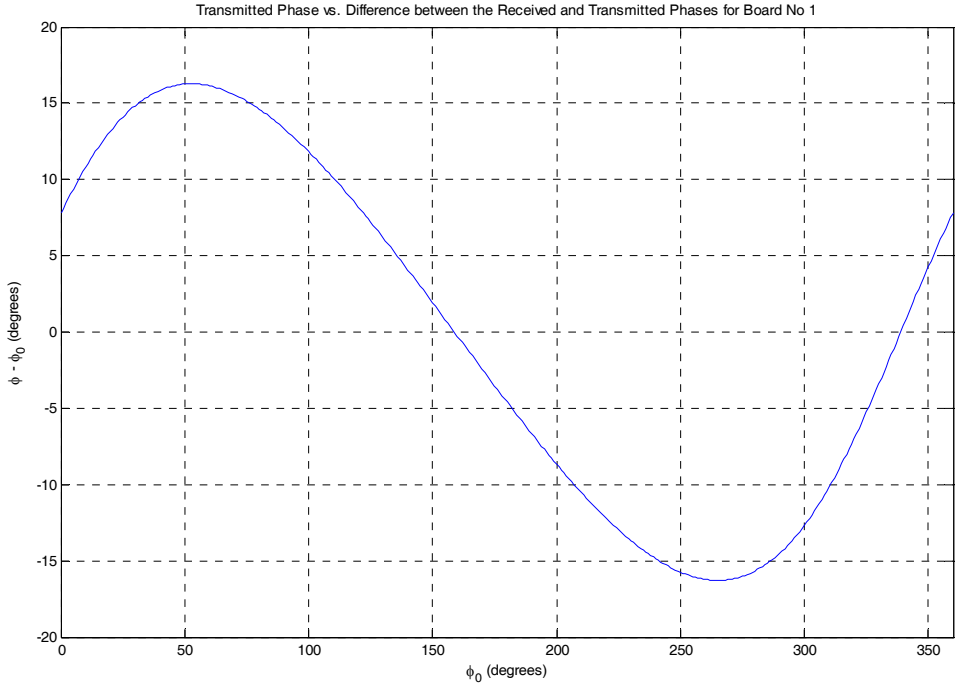

Figure F-4. Transmitted phase vs. the difference between the received and transmitted phases for Board 1.

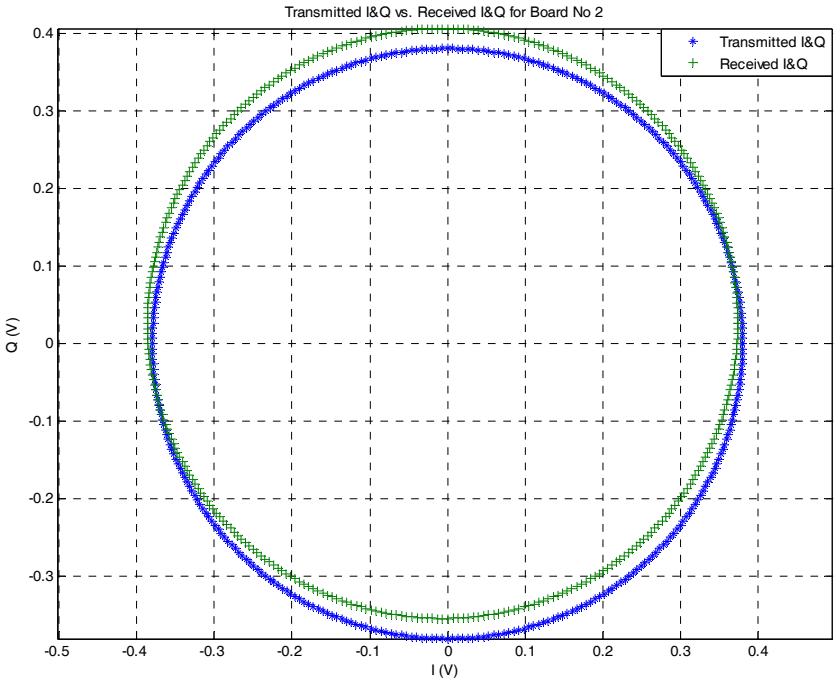

Figure F-5. Transmitted I and Q vs. received I and Q values for Board 2.

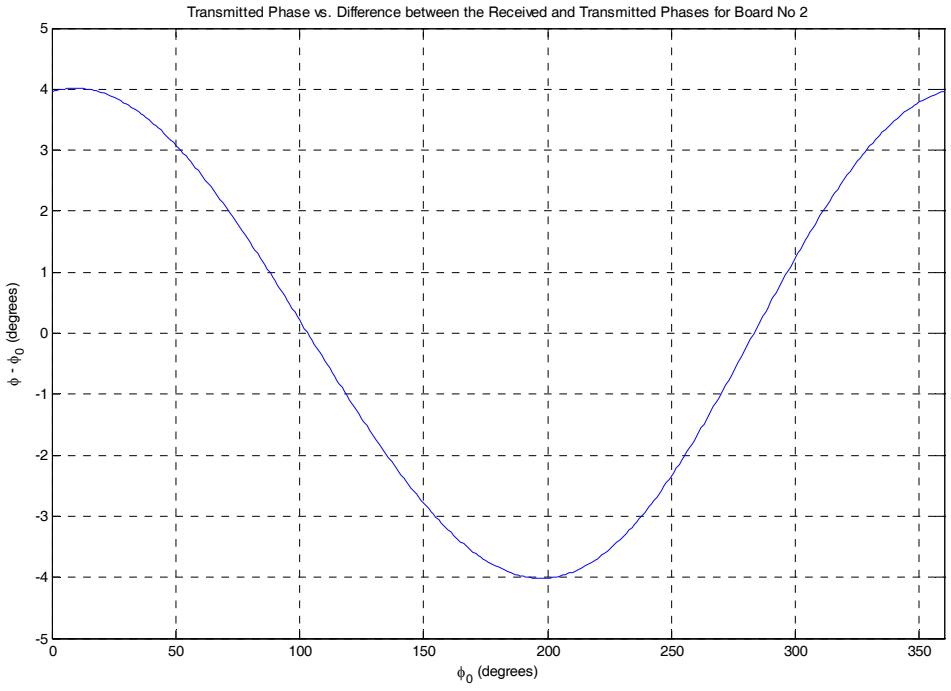

Figure F-6. Transmitted phase vs. the difference between the received and transmitted phases for Board 2.

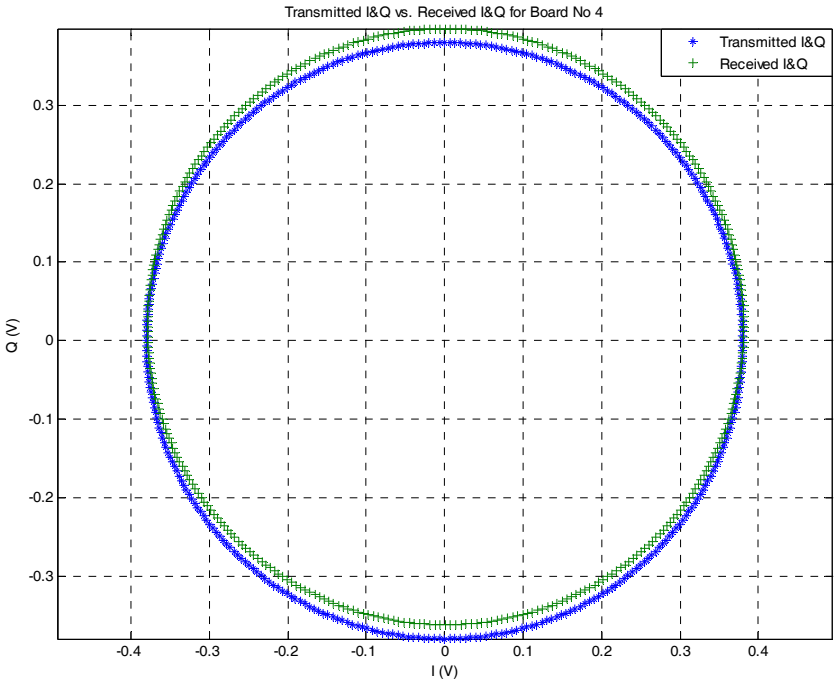

Figure F-7. Transmitted I and Q vs. received I and Q values for Board 4.

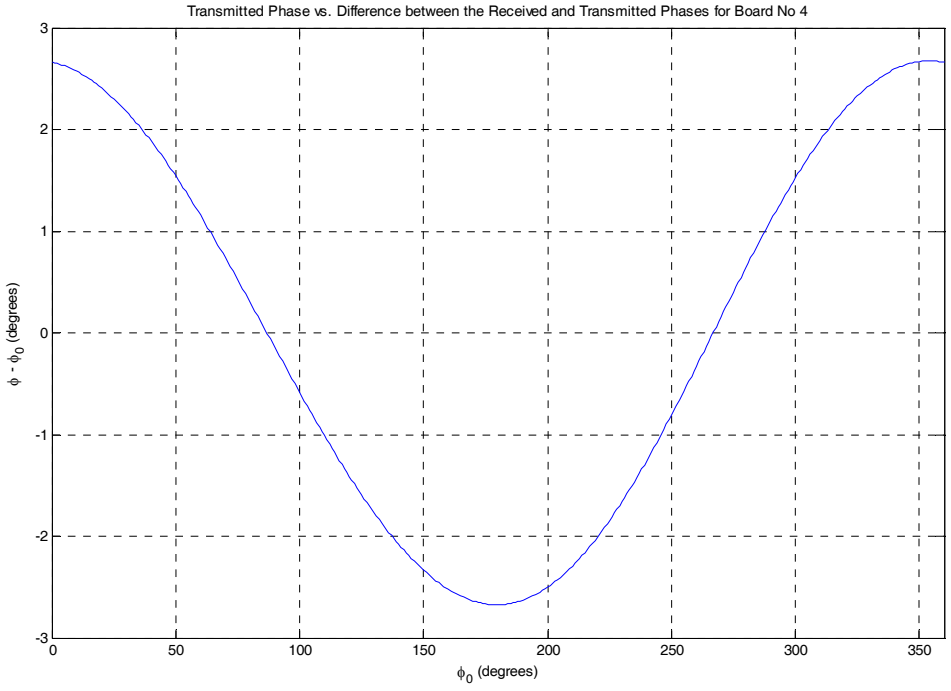

Figure F-8. Transmitted phase vs. the difference between the received and transmitted phases for Board 4.

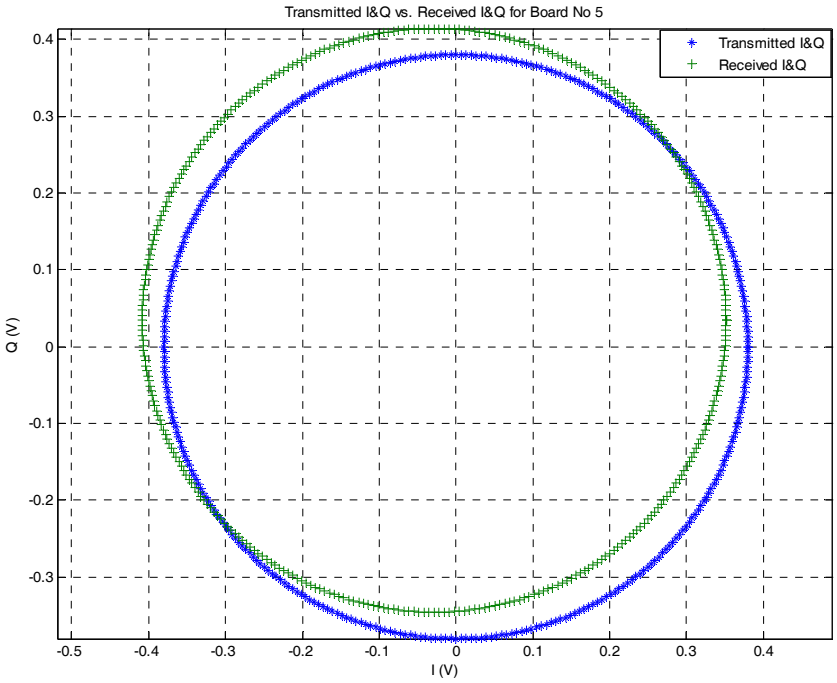

Figure F-9. Transmitted I and Q vs. received I and Q values for Board 5.

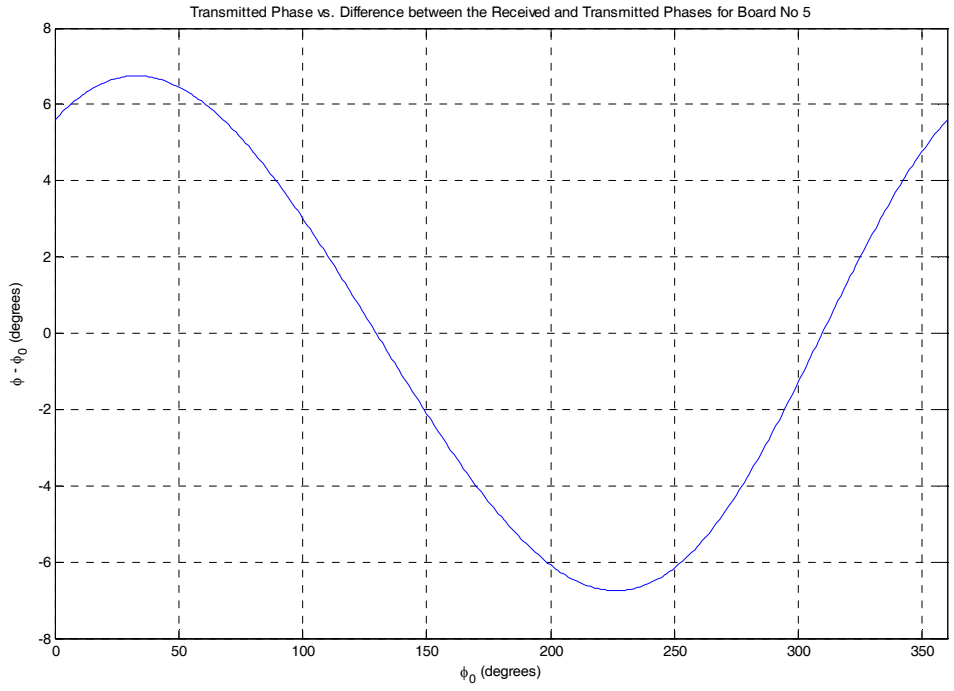

Figure F-10. Transmitted phase vs. the difference between the received and transmitted phases for Board 5.

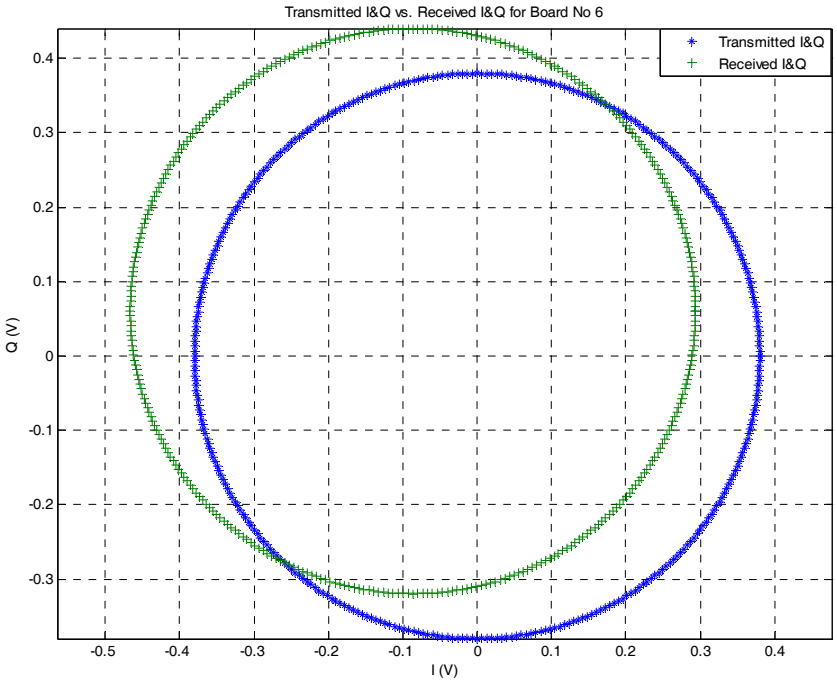

Figure F-11. Transmitted I and Q vs. received I and Q values for Board 6.

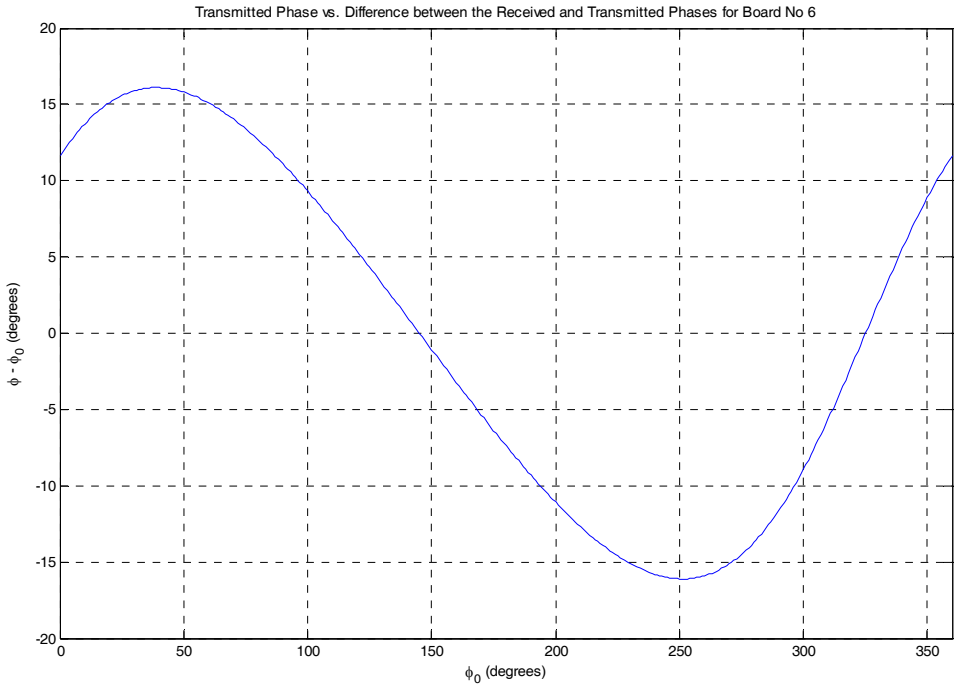

Figure F-12. Transmitted phase vs. the difference between the received and transmitted phases for Board 6.

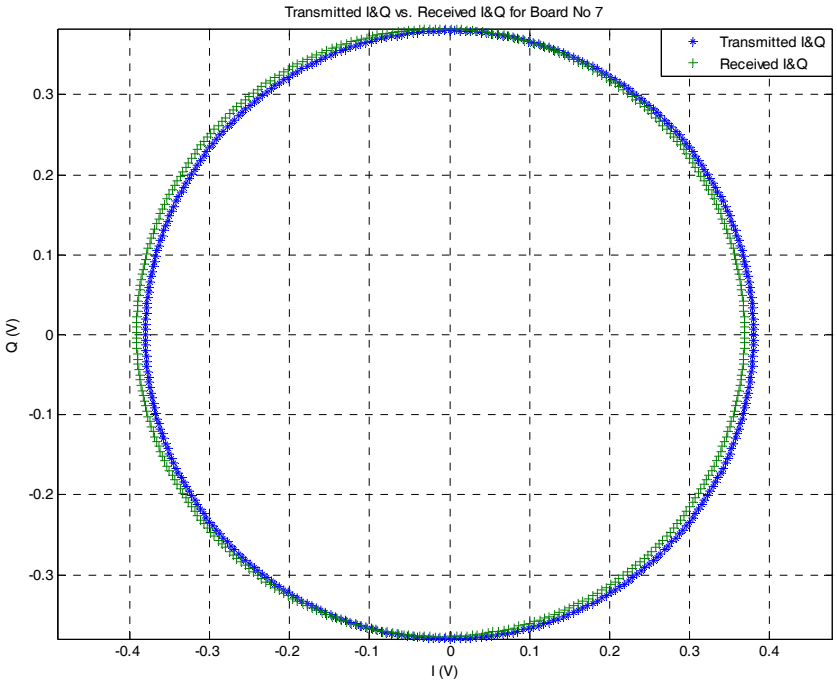

Figure F-13. Transmitted I and Q vs. received I and Q values for Board 7.

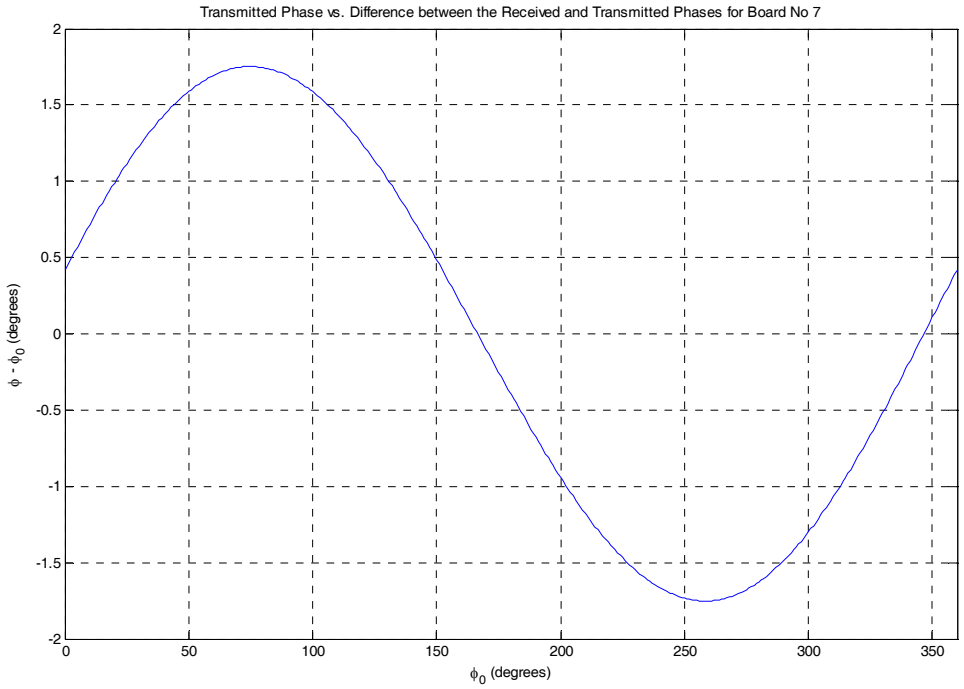

Figure F-14. Transmitted phase vs. the difference between the received and transmitted phases for Board 7.

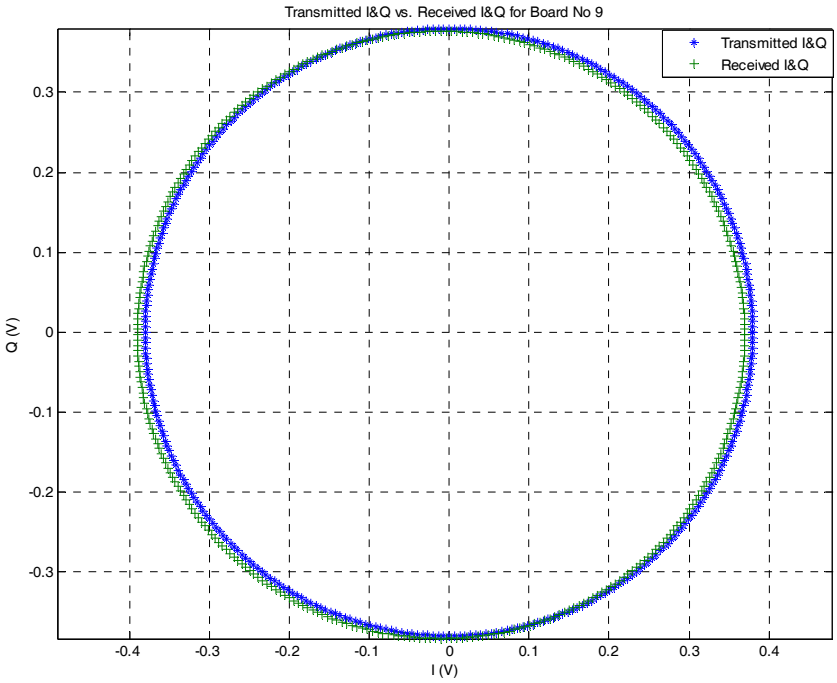

Figure F-15. Transmitted I and Q vs. received I and Q values for Board 9.

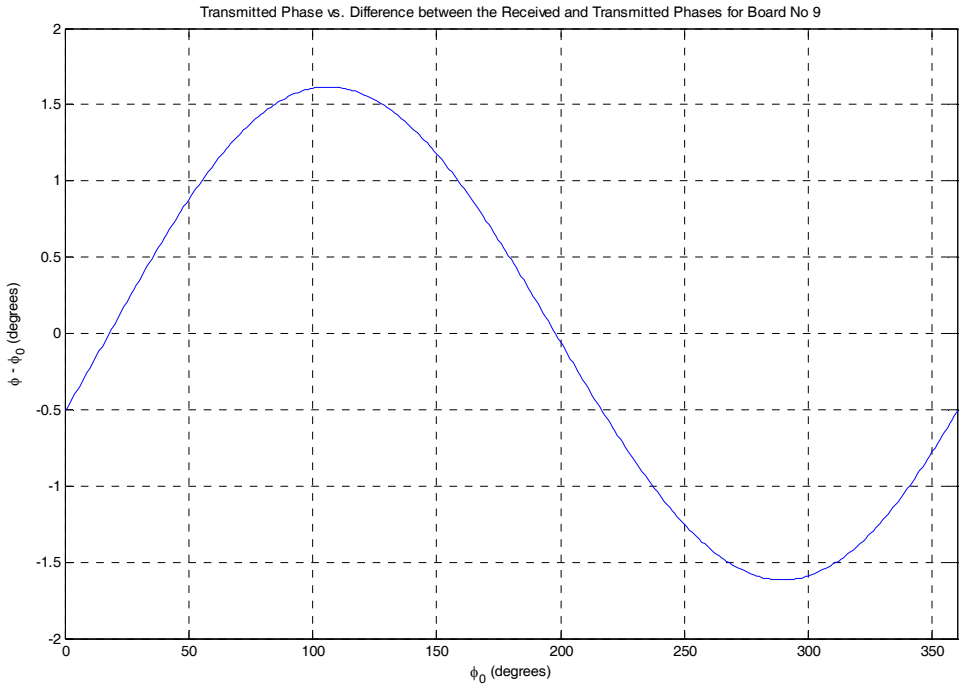

Figure F-16. Transmitted phase vs. the difference between the received and transmitted phases for Board 9.

G. MATLAB CODE FOR FINDING THE INTER-ELEMENT PHASE DIFFERENCES

```
% Overall Phase Mesuremenents

clc;clear;

p_V= rad2deg(unwrap((pi/180)*xlsread('Characterization_Board_1_Pos_1','B2:B14')));

P_1= rad2deg(unwrap((pi/180)*xlsread('Characterization_Board_1_Pos_1','M2:M14')));
P_0= rad2deg(unwrap((pi/180)*xlsread('Characterization_Board_0_Pos_2','M2:M14')));
P_2= rad2deg(unwrap((pi/180)*xlsread('Characterization_Board_2_Pos_3','M2:M14')));
P_4= rad2deg(unwrap((pi/180)*xlsread('Characterization_Board_4_Pos_4','M2:M14')));
P_9= rad2deg(unwrap((pi/180)*xlsread('Characterization_Board_9_Pos_5','M2:M14')));
P_5= rad2deg(unwrap((pi/180)*xlsread('Characterization_Board_5_Pos_6','M2:M14')));
P_6= rad2deg(unwrap((pi/180)*xlsread('Characterization_Board_6_Pos_7','M2:M14')));
P_7= rad2deg(unwrap((pi/180)*xlsread('Characterization_Board_7_Pos_8','M2:M14')));

Q_1=polyfit(p_V,P_1,1); y_1=polyval(Q_1, p_V);
o_1=polyval(Q_1,-180); pc_1=0;
Q_0=polyfit(p_V,P_0,1); y_0=polyval(Q_0, p_V);
o_0=polyval(Q_0,-180); pc_0=o_0-o_1;
Q_2=polyfit(p_V,P_2,1); y_2=polyval(Q_2, p_V);
o_2=polyval(Q_2,-180); pc_2=o_2-o_1;
Q_4=polyfit(p_V,P_4,1); y_4=polyval(Q_4, p_V);
o_4=polyval(Q_4,-180); pc_4=o_4-o_1;
Q_9=polyfit(p_V,P_9,1); y_9=polyval(Q_9, p_V);
o_9=polyval(Q_9,-180); pc_9=o_9-o_1;
Q_5=polyfit(p_V,P_5,1); y_5=polyval(Q_5, p_V);
o_5=polyval(Q_5,-180); pc_5=o_5-o_1;
Q_6=polyfit(p_V,P_6,1); y_6=polyval(Q_6, p_V);
o_6=polyval(Q_6,-180); pc_6=o_6-o_1;
Q_7=polyfit(p_V,P_7,1); y_7=polyval(Q_7, p_V);
o_7=polyval(Q_7,-180); pc_7=o_7-o_1;

figure(1)
plot(p_V,P_1,'k',p_V,P_0,'y',p_V,P_2,'m',p_V,P_4,'c',...
p_V,P_9,'r',p_V,P_5,'g',p_V,P_6,'b',p_V,P_7,'*');
grid on; title('Raw Phase Data');
xlabel('Transmitted Phase'); ylabel('Received Phase');
legend('D1', 'D0', 'D2', 'D4', 'D9', 'D5', 'D6', 'D7');
axis([-360 0 -500 -50]);
```

```
figure(2)
plot(p_V,y_1-pc_1,'k',p_V,y_0-pc_0,'y',p_V,y_2-pc_2,'m',p_V,y_4-pc_4,'c',...
p_V,y_9-pc_9,'r',p_V,y_5-pc_5,'g',p_V,y_6-pc_6,'b',p_V,y_7-pc_7,'*');
grid on; title('Finding Off-set Phase Corrections');
xlabel('Transmitted Phase'); ylabel('Received Phase');
legend('D1', 'D0', 'D2', 'D4', 'D9', 'D5', 'D6', 'D7');
axis([-360 0 -500 -50]);

figure(3)
plot(p_V,P_1-pc_1,'k',p_V,P_0-pc_0,'y',p_V,P_2-pc_2,'m',p_V,P_4-pc_4,'c',...
p_V,P_9-pc_9,'r',p_V,P_5-pc_5,'g',p_V,P_6-pc_6,'b',p_V,P_7-pc_7,'*');
grid on;
grid on; title('The Corrected Phase Data For Each Demodulator');
xlabel('Transmitted Phase'); ylabel('Received Phase');
legend('D1', 'D0', 'D2', 'D4', 'D9', 'D5', 'D6', 'D7');
axis([-360 0 -500 -50]);
```

THIS PAGE INTENTIONALLY LEFT BLANK

LIST OF REFERENCES

[1] Dr. Probir K. Bondyopadhyay, "*The First Application of Array Antenna*" 2000 The Proceedings of IEEE International Conference on Phased Array Systems & Technology, Dr. Michael Thorburn, ed., pp. 29-33, IEEE Operations Center, New Jersey, Pub. No. 00TH8510, 2005.

[2] John A. Bartee, "Genetic algorithms as a tool for phased array radar design," Master's Thesis, Naval Postgraduate School, Monterey, California, June 2002.

[3] L.C.Esswein, "Generic algorithm design and testing of a random element 3-D 2.4 GHz phased array transmit antenna constructed of commercial RF microchips," Master's Thesis, Naval Postgraduate School, Monterey, California, June 2003.

[4] Cher Sing, Eng, "Digital antenna architectures using commercial off the shelf hardware," Master's Thesis, Naval Postgraduate School, Monterey, California, December 2004.

[5] Chin Siang, Ong, "Digital phased array architectures for radar and communications based on off-the-shelf wireless technologies," Master's Thesis, Naval Postgraduate School, Monterey, California, December 2004.

[6] Yoke Chuang, Yong, "Receive channel architecture and transmission system for digital array radar," Master's Thesis, Naval Postgraduate School, Monterey, California, December 2005.

[7] Kevin Jones, private conversation, Naval Postgraduate School, 23 April 2006.

[8] www.cmc.sandia.gov/.../images/image010.gif, August 2006.

[9] Merrill I. Skolnik, *Introduction to Radar Systems*, 3rd Edition, pp. 210-238, McGraw-Hill, New York, NY, 2001.

[10] http://www.fas.org/man/dod-101/navy/docs/vis99/v99-ch3d.html, May 2006 .

[11] Merrill Skolnik, *Radar Handbook*, 2nd Edition, pp. 18.1-18.60, McGraw-Hill, New York, NY, 1990.

[12] David C. Jenn, Notes from EC4610 (Radar Systems), Naval Postgraduate School, California, 2005 (unpublished).

[13] David K. Barton, *Radar System Analysis*, pp.83-89, 327-331, Artech House, Dedham, MA, 1979.

[14] Filippo Neri, *Introduction to Electronic Defense Systems*, 2nd Edition, pp. 156-170, Artech House, Norwood, MA, 2001.

[15] Warren L. Stutzman and Gary A. Thiele, *Antenna Theory and Design*, 2nd Edition, pp. 80 , 88-136, Wiley, Indianapolis, IN, 1998.

[16] Prof. David C. Jenn and Paul Sumagaysay, Notes from CS4920 (Homeland Security), Naval Postgraduate School, California, 2.002 (unpublished)

[17] David C. Jenn, *Radar and Laser Cross Section Engineering*, 2nd Edition, pp. 208-211, AIAA, Reston, VA, 2005.

[18] CST Studio Suite 2006, *CST Microwave Studio Getting Started.*

[19] David C. Jenn, "Tracking Arrays", Naval Postgraduate School, California, 2006 (unpublished notes).

[20] http://rfbayinc.com/LNA/LNA-2700.pdf, August 2006.

[21] http://members.tripod.com/michaelgellis/mixerscom.html, August 2006.

[22] http://www.analog.com/UploadedFiles/Data_Sheets/230407246AD8347_a.pdf, August 2006.

[23] Measurement and Automation Catalog 2006, National Instruments.

[24] http://sine.ni.com/nips/cds/view/p/lang/en/nid/202555, August 2006.

[25] Gert Burgstaller, "Wirelessly networked digital digital phased array: design and analysis of a 2.4 GHz demonstrator," EE Thesis, Naval Postgraduate School, Monterey, California, September 2006.

[26] http://www.tm.agilent.com/data/static/downloads/eng/Notes/interactive/an-95-1/an-95-1.pdf#search=%22HP%208510C%20VNA%20S%20parameter%20set%22, August 2006.

[27] Erenoglu, Burcak, “Naval Postgraduate School Anechoic Chamber Evaluation,” Master’s Thesis, Naval Postgraduate School, Monterey, California, September 2004.

THIS PAGE INTENTIONALLY LEFT BLANK

INITIAL DISTRIBUTION LIST

1. Defense Technical Information Center
   Ft. Belvoir, Virginia

2. Dudley Knox Library
   Naval Postgraduate School
   Monterey, California

3. Prof. David C. Jenn
   Department of Electrical and Computer Engineering
   Monterey, California

4. Robert D. Broadston
   Department of Electrical and Computer Engineering
   Monterey, California

5. Prof. Dan C. Boger
   Department of Information Sciences
   Monterey, California

6. Prof. Jeffrey B. Knorr
   Department of Electrical and Computer Engineering
   Monterey, California

7. Izmir Deniz Gozetleme Komutanligi
   Turkish Navy
   Izmir, TURKEY

8. Aratirma Merkezi Komutanligi
   Turkish Navy
   Istanbul, TURKEY